# PERFORMANCE STUDIES FOR THE PACIFIC OCEAN NEUTRINO EXPERIMENT (P-ONE)

By

Jean Pierre Twagirayezu

#### A DISSERTATION

Submitted to Michigan State University in Partial Fulfillment of the Requirements for the Degree of

Physics — Doctor of Philosophy

Physics and Astronomy

2025

#### ABSTRACT

# PERFORMANCE STUDIES FOR THE PACIFIC OCEAN NEUTRINO EXPERIMENT (P-ONE)

By

1

3

#### Jean Pierre Twagirayezu

During the past decade, the IceCube Neutrino Observatory has been at the forefront of neutrino astronomy, detecting a diffuse flux of extraterrestrial neutrinos and successfully identifying some sources of these high-energy neutrinos. However, most astrophysical neutrinos detected by IceCube have not been associated with known astronomical sources. The Pacific Ocean Neutrino Experiment (P-ONE), a km<sup>3</sup> scale neutrino telescope, is be-10 ing developed to be deployed in the northern hemisphere's Cascadia Basin, off the coast of Vancouver Island. By deploying P-ONE in the northern hemisphere and in water, where 12 light scattering is reduced compared to in-ice experiments, P-ONE will complement existing 13 or under-construction neutrino telescopes, such as IceCube, KM3NeT, and Baikal-GVD, to cover the full sky and provide additional observational windows for neutrino astronomy. 15 This thesis aims to forecast the sensitivity of the P-ONE to point sources using Monte 16 Carlo Simulations. We present a first detailed Monte Carlo event simulation for the P-17 ONE. This involves generating events in the detector volume, propagating Cherenkov light produced by secondary particles in the detector medium, leveraging software tools previously developed by the IceCube collaboration, and simulating the response of the optical module to the Cherenkov photons. We present a track event reconstruction algorithm, based on a maximum-likelihood 22

method, developed for the P-ONE using Monte Carlo simulation. Recorded light pulses

are evaluated using pre-computed arrival time distributions of Cherenkov photons at optical

- 25 modules as functions of track parameters. We found that for muon tracks with more than
- $_{26}~>700\,\mathrm{m}$  in track length, P-ONE can potentially reach an angular resolution of  $\sim0.1^\circ$  at
- $^{27}$  1 TeV, which improves to  $\sim 0.05^{\circ}$  at 1 PeV. These values are a factor of  $\sim 4$  better than
- those currently achieved by IceCube.
- 29 Finally, using the expected angular resolution, we estimate the discovery potential, the
- flux required to detect a point source of astrophysical neutrinos with P-ONE. We evaluated
- the expected performance of P-ONE for some known point source discovered by IceCube.
- We extend our calculations to a generic steady-point source located at different declinations.
- With expected track angular resolution at or below a tenth of a degree, P-ONE will be able
- to discover a steady point source, depending on the energy and flux, by observing as few as
- seven events from that source with a few years of operation.

Copyright by JEAN PIERRE TWAGIRAYEZU 2025

36

#### ACKNOWLEDGMENTS

37

First, I express my deepest gratitude to my advisor, Professor Tyce DeYoung, for the vital role you have played throughout my PhD journey. I am truly fortunate to have had the opportunity to learn under your guidance. The weekly meetings provided direction and clarity, particularly during times when I faced roadblocks and uncertainties. I am deeply appreciative of your patience during periods of slow progress and for your willingness to address every question, regardless of how naive it might have seemed. I am equally thankful to Professor Nathan for always supporting me. I would like to express my sincere appreciation to both of you for making this journey possible. Thank you all for providing me with the opportunity to participate in conferences and collaboration meetings, both within the United States and internationally.

I am very grateful to other committee members, Professor Pawel Danielewicz, Professor Wade Fisher, Professor Paul Gueye, and Professor Mehr Un Nisa, for your guidance, and constructive discussions, which made each of our annual committee meetings a highly valuable learning experience.

I extend my sincere thanks to Professor Pawel Danielewicz and Professor Kirsten Tollefson for the work you have done to help me get into the Michigan State University Graduate School. Thanks to Kim Crosslan and Brenda Wenzlick for your support in navigating the Department of Physics and Astronomy.

Thanks to all the professors who taught graduate classes I took at Michigan State University: Professor Carlo Piermarocchi, Professor Mohammad Maghrebi, Professor Vladimir Zelevinsky, Professor Wade Fisher, Professor Luke Roberts, Professor Andreas von Manteuffel, Professor Claudio Kopper, and Professor Dirk Colbry. I also thank Professor Ke Xianglin

- and Professor Saul Beceiro Novo for your guidance during my first two years as a Teaching
  Assistant.
- In the course of my PhD research, I was extremely fortunate to receive support from local experts at Michigan State University, as well as from people from other institutions through the IceCube and P-ONE collaborations. Foremost, I would like to thank my local collaborators and thesis committee members, Professor Tyce DeYoung, Professor Nathan Whitehorn, and Professor Mehr Un Nisa, as well as my mentor, Dr. Hans Niederhausen, for your consistent guidance and offering hands-on supports throughout the course of my PhD research.
- Professor Nathan Whitehorn and Dr. Hans Niederhausen thank you for the handson support during the development of the track reconstruction and point source analysis
  pipelines when I am stuck and struggling. Dr. Hans Niederhausen your expertise has been
  instrumental in helping me boost productivity. Without your consistent mentorship and
  hands-on support, the completion of this thesis would not have been possible. Thank you
  for being my guiding light.
- Dr. Chris Weaver, thank you for computing and technical supports. I am grateful to
  Dr. Thomas McElroy a and Professor Claudio Kopper for your assistance with the P-ONE
  software tools for generating Monte Carlo Simulations. Thank you, Dr. Hans Niederhausen,
  Professor Mehr Un Nisa, Dr. Tomas Kontrimas, and Dr. Martin Wolf, for your assistance
  with Skyllh. The skills I gained from using the Skyllh analysis framework and later the
  effort to extend it for the P-ONE have been instrumental in developing a point source analysis
  pipeline.
- Dr. Sarah Nowicki and Dr. Sebastian Enrique Sanchez Herrera, thank you for your hands-on computing support when I started working with the IceCube collaboration. The

- experience I got working on cascade reconstruction using the IceTray software framework
  was a valuable asset for a smooth transition when I started working on my PhD thesis for
  the P-ONE collaboration. Thank you, Dr. Steve Sclafani, Dr. Rob Halliday, and Dr. Shiqi
  Yu, for all the individual support you provided to me.
- Thank you Dr. Felix Ndayisabye and Dr. Pierre Nzabahimana sharing your experience with me. I am grateful to Professor Paul Gueye, Mornetka Gueye, and Rachel Younger for always checking on me. Thanks to the current and former graduate students within the IceCube and P-ONE research groups, as well as the members of NSBP at Michigan State University, with whom I spent many years in group meetings and occasionally other social activities, for being such wonderful people.
- I would also like to thank the members of the local church and community for their social support throughout my journey. Pastor Eric Mulanda, Professor Mark Worden, Pastor Alphonse Kwizera, Mathias Ndizihiwe, Jacques Mugisha, Dr. Judith Namanya, Jacqueline Kasine, and many others thank you. Thanks to my wife, Elizabeth Nyiransaba for your companionship. Thank my mom for the tireless efforts and the sacrifices you have made for me to reach where I am today. I owe you so much. You are, and will always be, my hero.
- This work is supported by the National Science Foundation under grant NSF PHY2237581 and Michigan State University.

# TABLE OF CONTENTS

Chap	ter 1 Neutrino Astronomy
1.1	Cosmic Rays
	1.1.1 Energy Spectrum
	1.1.2 Cosmic Ray Origins
	1.1.3 Astrophysical neutrinos
1.2	2 High-energy Neutrino detection
	1.2.1 Neutrino Interaction
	1.2.2 Cherenkov Radiation
	1.2.3 Event Signatures
1.3	
	1.3.1 Baikal-GVD
	1.3.2 KM3NeT
	1.3.3 IceCube
Chap	•
2.1	Introduction
2.2	2 Ocean Networks Canada
2.3	B P-ONE Pathfinder Missions
	2.3.1 STRAW
	2.3.2 STRAW-b
2.4	4 P-ONE Instrumentation
	2.4.1 P-ONE Optical Module
	2.4.2 Calibration Systems
2.5	
CI.	
Chap	
3.1	
3.2	
	3.2.1 Neutrinos Simulation
	3.2.2 Cosmic Ray Muons Simulation
~ -	1 1 0
3.3	4 Photon Propagation
3.4	

161	BEFEI	RENC	TES 10	na
160	Chapte	er 6	Conclusions	06
159	5.4	Outlo	ok	03
158	٠.	5.3.3		01
157		5.3.2		00
156		5.3.1	O	98
155	5.3			98
154		5.2.3	1	96
153		5.2.2	1 0	94
152		5.2.1	1 0	91
151	5.2	Analy	rsis Method	90
150	5.1	MC S	Simulation Dataset	85
149	Chapte	er 5	3	85
	2.3	5 4010		
148	4.5			80
147		4.4.2		76
146	2.1	4.4.1		76
145	4.4	Recon	1	
144		1.0. <b>2</b>		73
143		4.3.2		70
142	1.0	4.3.1	1	69
141	4.3		1	65
140		4.2.2		60
139		4.2.1		58
138	4.2	Photo	on Arrival Time Parametrization	57

# LIST OF TABLES

162	Table 5.1:	Expected bkg and NGC 1068 signal events / 1 year livetime	99
163	Table 5.2:	Expected bkg and NGC 1068 signal events $/$ 10 years livetime	100

# LIST OF FIGURES

164 165	Figure 1.1:	Cosmic ray energy spectrum measured by air-shower experiments. Figure is taken from [1]	3
166	Figure 1.2:	Neutrinos in the Standard Model of particles. The figure is taken from [2].	6
167 168 169 170	Figure 1.3:	Neutrino energy spectra from different neutrino sources. The atmospheric neutrino flux (green) dominates the astrophysical neutrino flux from diffuse neutrino emission from AGN (pink) up to 100 TeV. This plot is taken from [3]	7
171 172 173	Figure 1.4:	Feynman diagram for neutrino-nucleon deep inelastic scattering for Charged-Current (left) and Neutral-Current (right) interaction channels. Diagram taken from Ref. [4]	9
174 175 176	Figure 1.5:	The geometry of the Cherenkov radiation. Figure from Ref. [5]. The blue arrow shows the direction of Cherenkov radiation. The red arrow shows the particle traveling at speed $v_p$ such that $\frac{c}{n} < v_p < c$ . Where $v_p = \beta c$	
177		c	10
178	Figure 1.6:	Neutrino interactions signatures	12
179	Figure 1.7:	Particle mean free path lengths. Figure taken from [6]	12
180	Figure 1.8:	Muon energy loss. Figure taken from [6]	14
181 182	Figure 1.9:	A schematic view of the Baikal-GVD telescope with its modular structure of clusters. Figure taken from [7]	17
183 184 185	Figure 1.10:	Comparison between KM3NeT's ARCA and ORCA detectors. Instrumented on about 1 km <sup>3</sup> , ARCA has 115 detection units in each block. Figure taken from the KM3NeT website [8]	18
186	Figure 1.11:	IceCube Neutrino Observatory layout. The Picture is taken from [9]	20
187 188 189 190	Figure 2.1:	Neutrino Telescopes field of view. P-ONE's location in the northern Pacific Ocean will provide a sky view complementary to existing and planned neutrino telescopes in Antarctica, the Mediterranean, Lake Baikal, and the western Pacific [10]. Image courtesy. Lisa Schumacher	23

191 192 193 194	Figure 2.2:	The Ocean Network Canada NEPTUNE Observatory. The STRAW and STRAW-b instruments for site investigation were deployed at the Cascadia Basin node. P-ONE is planned to be deployed at the Cascadia Basin as well. Image courtesy of ONC	24
195 196	Figure 2.3:	Detailed technical sketch of the two STRAW mooring lines showing all modules' exact (measured) geometry	26
197	Figure 2.4:	POCAM2 deployment Inspection in June 2018. Pictures courtesy of ONC.	27
198	Figure 2.5:	sDOM4 deployment Inspection in June 2018. Pictures courtesy of ONC.	27
199 200	Figure 2.6:	Attenuation length measurement results from two years of STRAW data are shown in black. The figure is taken from Ref. [11]	29
201	Figure 2.7:	STRAW-b deployment. Picture courtesy of ONC	30
202 203 204 205	Figure 2.8:	A sketch diagram of the STRAW-b mooring line(left), indicating the locations of all modules. Examples on the right show the housing glass sphere Standard Module (top right) and the PMT-Spectrometer (middle right and bottom right). Figure taken from [12]	33
206	Figure 2.9:	STRAW-b PMT-Spectrometer module. Image taken from Ref. [12]	34
207	Figure 2.10:	Picture of P-OM prototype. Picture taken from Ref. [13]	36
208	Figure 2.11:	Picture of P-OM prototype. Picture taken from Ref. [13]	37
209 210 211 212 213	Figure 2.12:	Top left: The P-CAL hemisphere layout view from CAD software. Top right: P-CAL interior optics, self-monitoring, and camera system. Bottom: Illustration of P-ONE optical module (P-OM) with integrated acoustic receiver highlighted in red. The top figures are taken from Ref. [14]. The bottom figure is taken from Ref. [15]	39
214 215 216 217 218 219	Figure 2.13:	The figure shows the anticipated P-ONE acoustic positioning system. The three transponders(red) and acoustic transceiver (yellow) are all external to the P-ONE optical modules. The piezo-acoustic receivers will be housed in P-OMs(black) and P-CALs(green) as shown in Fig. 2.12. Two acoustic receivers are planned to be installed in every P-ONE module. The figure is taken from Ref. [15]	40
220 221 222 223	Figure 2.14:	The plot on the left illustrates the P-ONE geometry configuration concept. P-ONE will be deployed in modules of seven clusters of mooring lines. The right plot shows a cluster consisting of ten mooring lines. The figure is taken from Ref. [16]	41

224 225 226 227 228 229 230	Figure 2.15:	Top view of the simulated full 70-string P-ONE reference geometry. This test geometry has the following dimensions: The distance between cluster centers is 400 m. Each cluster consists of 10 mooring lines, each about 1 km long. The distance between the strings is about 80 m. Each string will contain 20 optical modules, and each optical module consists of 16 photomultiplier tubes [17]. The string-to-string spacing is based on a preliminary study [18]	42
231	Figure 3.1:	Simulation Chain	44
232 233 234 235 236 237	Figure 3.2:	Display of an example of the simulated event at 500 TeV that crosses different clusters shown in the event viewer using Icetray software. The gray dots indicate the positions of individual DOM on the mooring line using simulated detector geometry in Fig. 2.15. The circle shows the simulated physics signal. Photoelectrons that arrived early are colored red, and those that arrived late are colored green	45
238 239	Figure 3.3:	An example of a simulated high-energy muon with uncleaned pulses. Credit Nathan Whitehorn	51
240 241	Figure 3.4:	An example of a simulated high-energy muon with cleaned pulses. Credit Nathan Whitehorn	52
242 243	Figure 4.1:	Parameters defining Cherenkov light of a muon near an Optical Module. Figure taken from Ref. [19])	56
244 245 246 247 248 249	Figure 4.2:	A histogram of the residual time pdf from the Monte Carlo simulation around effective distances of 10 m using a 20 cm slice. The figure also compares the MC time residual with the pdf parameterization using the mixture model pdf (black) and its individual pdf component contributions based on Eq. (4.7). The top plot displays a linear scale on the y-axis, while the bottom plot uses a log scale	61
250 251 252 253 254	Figure 4.3:	A histogram of the residual time pdf from the Monte Carlo simulation around effective distances of 30 m using a 20 cm slice. The figure also compares the MC time residual with the pdf parameterization using the mixture model pdf (black) and its individual pdf component contributions based on Eq. (4.7). The top plot displays a linear scale on the y-axis, while the bottom plot uses a log scale	62

256 257 258 259 260 261	Figure 4.4:	Histograms of the residual time pdf from the Monte Carlo simulation around effective distances of 100 m using a 20 cm slice. The figure also compares the MC time residual with the pdf parameterization using the mixture model pdf (black) and its individual pdf component contributions based on Eq. (4.7). The top plot displays a linear scale on the y-axis, while the bottom plot uses a log scale	63
262 263 264 265 266 267 268 269 270	Figure 4.5:	Comparison of CPandel vs mixture model PDF (mmpdf) parametrization of the MC simulation time residual histograms for DOM distance around 10 m (top plots), 30 m (middle plots), and 100 m (bottom plots) using 20 cm slices. The right plots display a linear scale on the y-axis, while the bottom plots use a log scale on the y-axis. The results for the CPandel PDF [20] implemented in IceCube IceTray software framework as discussed in Ref. [21]. Here we used the following free parameters: tau scale of $\tau=20$ ns, an absorption length $\lambda_a=25$ m, and a scattering length $\lambda=120$ m. The plots are for timing uncertainty of the PMT of $\sigma=1.5$ ns.	64
271 272 273 274 275	Figure 4.6:	Histograms of the residual time pdf from the Monte Carlo simulation around effective distances of 2 m using a 20 cm slice. The figure also compares the MC time residual with the B-splines PDF (black) and the mixture model PDF (red). The top plot displays a linear scale on the y-axis, while the bottom plot uses a log scale	66
276 277 278 279 280	Figure 4.7:	Histograms of the residual time pdf from the Monte Carlo simulation around effective distances of 30 m using a 20 cm slice. The figure also compares the MC time residual with the B-splines PDF (black) and Mixture Model PDF (red). The top plot displays a linear scale on the y-axis, while the bottom plot uses a log scale	67
281 282 283 284 285	Figure 4.8:	Histograms of the residual time pdf from the Monte Carlo simulation around effective distances of 100 m using a 20 cm slice. The figure also compares the MC time residual with the B-splines PDF (black) and the mixture model PDF (red). The top plot displays a linear scale on the y-axis, while the bottom plot uses a log scale	68
286 287 288	Figure 4.9:	A likelihood fitter needs a seed service, a parametrization service, a log-likelihood service, and a minimizer service. Diagram adapted per Gulliver from IceTray documentation	69

289 290	Figure 4.10:	The left diagrams are visualizations of a simulated 505 TeV event as it passes through the detector volume in the event viewer. The color-coding	
291		indicates the arrival time of the photoelectrons, with red marking early	
292		arrivals and green marking late arrivals. The right-hand plots show the	
293		profile likelihood scans for the event shown in the left diagrams. The	
294		color bar is a test statistic, $-2(\log \mathcal{L} - \min(\log \mathcal{L}))$ , indicating how much	
295		each log-likelihood deviates from the minimum. The green cross shows	
296		the direction found by a simple fitter seeded with the Monte Carlo truth	
297		for all parameters. The orange cross shows the direction of the minimum	
298		likelihood found during the grid scan. The top plots utilize a likelihood	
299		based on our mixture model PDF (see Eq. 4.7). The bottom-right plot	
300		uses the B-spline PDF parameterization instead of the mixture model	
301		shown in Fig. 4.2.2. Figure courtesy of H. Niederhausen	71
302	Figure 4.11:	The left diagrams are visualizations of a simulated 11 TeV event as it	
303		passes through the detector volume in the event viewer. The color-coding	
304		indicates the arrival time of the photoelectrons, with red marking early	
305		arrivals and green marking late arrivals. The right-hand plots show the	
306		profile likelihood scans for the event shown in the left diagrams. The	
307		color bar is a test statistic, $-2(\log \mathcal{L} - \min(\log \mathcal{L}))$ , indicating how much	
308		each log-likelihood deviates from the minimum. The green cross shows	
309		the direction found by a simple fitter seeded with the Monte Carlo truth	
310		for all parameters. The orange cross shows the direction of the minimum	
311		likelihood found during the grid scan. The top plots utilize a likelihood	
312		based on our mixture model PDF (see Eq. 4.7). The bottom-right plot	
313		uses the B-spline PDF parameterization instead of the mixture model	
314		shown in Fig. 4.2.2. Figure courtesy of H. Niederhausen	72
315	Figure 4.12:	Distribution of the opening angles between reconstructed and true direc-	
316		tion using a simple fitter and LineFit as seed. For all events in these	
317		histograms, the minimizer indicated that it converged, and we selected	
318		events that have a valid track length (LDirA: see Sec. 4.4.1). In the left	
319		plot, around 93% of events are stuck in local minima. In the right plot,	
320		only 25% of the simulated events with track length greater than or equal	
321		to 700 m have an opening angle less than 0.1 degree	73
322	Figure 4.13:	Flow diagram for our baseline reconstruction method	74
323	Figure 4.14:	An example of B-splines PDFs convolution. The plot shows a histogram	
324		of residual times of photons recorded at a distance of 30 m from the	
325		emission point on the muon track (blue) and the B-spline (black), as well	
326		as convolutions of the B-spline with different Gaussian widths used as a	
327		benchmark for reconstruction	75

328 329 330	Figure 4.15:	A screenshot of the event viewer of a simulated track event of 33 TeV that is estimated to have a visible length of approximately 900 m in the detector volume	76
331 332 333 334 335 336 337	Figure 4.16:	Profile scans for simulated event in Fig. 4.15 using 20 ns convolution (upper left), 10 ns convolution (top-right), 5 ns convolution (bottom left). The plot in the bottom right uses no convolution. Additionally, a 35 ns convolution has been performed but is not shown in the plot. For this event, LineFit has an opening angle of 3.24 degrees. A simple fitter starting from LineFit results in an opening angle 2.69 degrees. However, starting from the LineFit seed and performing iterative fits yields an opening angle of 0.053 degrees.	77
339 340	Figure 4.17:	A screen shot of the event viewer of a simulated track event of 76 TeV that is estimated to have a visible length of $160~\rm m$ in the detector volume. 	78
341 342 343 344 345 346 347 348	Figure 4.18:	Profile scans for simulated event in Fig. 4.17 using 20 ns convolution (upper left), 10 ns convolution (top-right), 5 ns convolution (bottom left). The plot in the bottom right does not use convolution. Additionally, a 35 ns convolution has been performed but is not shown in the plot. For this event, LineFit has an opening angle of 9.02 degrees. A simple fitter starting from LineFit results in an opening angle 2.67 degrees. However, starting from the LineFit seed and performing iterative fits yields an opening angle of 8.34 degrees.	79
349 350 351 352 353 354 355	Figure 4.19:	The figure shows the median of the opening angle as a function of muon energy for different selections based on the estimated visible track length. The solid lines represent the resolution for the likelihood fit seeded with truth values without using an intermediate step convolution method. The dashed lines are the results using the Gaussian-convolution iterative strategy discussed in Sec. 4.3.2.1. The median was calculated for muon simulations following an energy spectrum of $E^{-1}$	80
356 357 358 359 360 361	Figure 4.20:	The opening angle distribution for muon tracks with a visible length larger than 700 m (top figure) and 100 m (bottom figure). The histograms with a solid line represent the event resolution for the likelihood fit seeded with truth values without using an intermediate step convolution method. The histogram with a dashed line is the result using the Gaussian-convolution iterative strategy	82
362 363 364 365 366	Figure 4.21:	Reconstruction performance plot using a hypothetical seed. Using the von Mises-Fisher distribution from scipy [22], we generated hypothetical seeds that are 1 degree away from the event's true directions in median opening angle. The plot shows the distribution of expected angular resolution, starting with these hypothetical seeds that have a 1-degree opening angle.	83

367 368 369 370 371 372 373 374 375	Figure 4.22:	Reconstruction performance plot using a hypothetical seed. Using the von Mises-Fisher distribution from scipy [22], we generated hypothetical seeds that are 1 degree away from the event's true directions in median opening angle. The plots show the expected angular resolution as a function of muon energy. The solid lines represent the results of a likelihood fit using a truth seed as the initial guess, without a convolution strategy. The dotted lines indicate the expected performance from the Gaussian-convolution iterations in Sec. 4.2.2 seeded with a hypothetical seed, which is a 1-degree median opening from true event directions	84
376 377 378 379 380 381 382 383	Figure 5.1:	Top plot shows the distribution of expected event rate from a flux of conventional and prompt atmospheric neutrinos, a diffuse flux of astrophysical neutrinos, and the flux of neutrino events from NGC 1068 [23] source as a function of muon neutrino energy bin for a livetime of 10 years of P-ONE detector operation. The bottom plot shows the distribution of expected neutrino events as a function of the zenith angle for the fluxes of conventional and prompt atmospheric neutrinos, as well as a diffuse flux of astrophysical neutrinos	87
384 385 386 387	Figure 5.2:	The plots show the distribution of the event angular distance between true direction and sampled direction using von Mises-Fisher distribution assuming a median angular resolution of 0.08 degree. The solid line uses the Rayleigh distribution	89
388 389 390 391 392 393 394 395	Figure 5.3:	Effective area of the simulated P-ONE test geometry (see Fig. 2.15) as a function of neutrino energy for different zenith angle bands at trigger level. The effects of Earth absorption on neutrinos with core-crossing trajectories are visible at high energies for events that enter the detector from below. The trigger applied here looks for events with pulses on at least 3 PMTs within a 10 ns window. The current simulated test geometry has an effective area at trigger level comparable to that of the IceCube detector, as expected based on their comparable geometric volumes [24].	91
396 397 398	Figure 5.4:	The figure shows the altitude as a function of MJD time for the source NGC 1068, as seen by a detector at the P-ONE location over a single day. In subsequent days, the source transits to the same position in the local horizontal goodinates.	93
399		horizontal coordinates	,

400 401 402 403 404 405 406 407 408	Figure 5.5:	bottom plot shows a section of the altitude band used when calculating the number of expected events in an angular search bin at one specific central time bin of a day. The dotted red line shows the boundaries of the altitude band. The black circle shows the size of the angular bin. Other circles show the angular error on MC events resulting from vMF sampling with an angular error of 0.08 degrees. Events with smaller circles than the black one are used to calculate the expected signal, while those with larger circles are not counted in during the analysis	95
409 410 411 412 413	Figure 5.6:	The significance of observing NGC 1068 [23] for different observation times. The blue line shows the performance expectation of the P-ONE based on our angular resolution assumption of 0.08 degrees. In contrast, the orange line shows the performance for a detector with an expected median angular resolution of 0.60 degrees	100
414 415 416 417 418 419	Figure 5.7:	The plot on the top (bottom) shows the minimum number of signal events (flux) needed to reach a discovery potential with a significance of 5 sigma over 10 years exposure for a $\gamma=2$ source at different declinations. The blue lines in both plots indicate predictions for a detector located at the P-ONE location for a median angular resolution of the track reconstruction of 0.6 degrees	102
420 421 422 423 424	Figure 5.8:	(flux) needed to reach a discovery potential with a significance of 5 sigma over 10 years exposure for a $\gamma=2$ source at different declinations. The blue lines in both plots indicate predictions for a detector located at the P-ONE location for a median angular resolution of the track reconstruction	104
425		of 0.6 degrees	104

# Chapter 1

# Neutrino Astronomy

In 1912, Victor Hess discovered cosmic rays when conducting a series of balloon experiments
to measure ionizing radiation at increasing altitudes. Despite the progress that has been
made to measure their energy spectrum and composition, the origin of cosmic rays, these
very high energies, remains a mystery.

Accelerated cosmic rays interact with ambient photons or matter. These interactions produce neutrinos, gamma rays, and cosmic rays (see Sec.1.1.3). Cosmic rays have been measured by multiple air-shower experiments up to Energy about 10<sup>20</sup> eV (see Sec.1.1). As these are charged particles, the interstellar magnetic field deflects them, and by inferring their sources from their energy spectrum, the composition measurement is limited.

On the other hand, gamma-rays produced from the decay of neutral pions resulting from
cosmic ray interactions can travel to Earth and provide evidence of cosmic ray sources, such
as supernova remnants [25]. However, gamma-rays are attenuated by intervening matter and
radiation in the galaxy and can often be obscured by synchrotron radiation from electrons
also present in the source.

Astrophysical high-energy neutrinos produced from the hadronic interactions (Eq. (1.3) and Eq. (1.2)) of cosmic rays are not deflected by the galactic magnetic field and point directly from their sources; and therefore are ideal messenger particles for identifying the sources of cosmic rays. But they are challenging to detect, and only a large neutrino telescope

increases their chance of being detected.

In this chapter, we introduce the field of neutrino astronomy. In Sec. 1.1, we briefly discuss the astrophysical neutrinos and their connection to cosmic rays. Sec. 1.2 discusses the methods that neutrino telescopes use to detect neutrinos indirectly, followed by Sec. 1.3 that highlights current operational neutrino telescopes.

### 1.1 Cosmic Rays

#### 452 1.1.1 Energy Spectrum

Cosmic rays have been measured by various experiments in terms of energy spectrum and composition. The plot in Fig. 1.1 shows the cosmic ray energy spectrum measurement over several orders of magnitude in energy. They mainly consist of protons (hydrogen nuclei) above 90%, but also include alpha particles (helium nuclei), heavier atomic nuclei, electrons, and positrons. These particles travel through space at nearly the speed of light and possess energies that span a wide range, some even exceeding  $10^{20}$  eV, far beyond what any human-made particle accelerator can achieve. The number of particles decreases rapidly as the energy increases. At the energy above a few GeV the differential energy spectrum follows approximately a power-law distribution given by Eq. (1.1), where is  $\gamma$  the spectral index.

$$\frac{dN}{dE} \propto E^{-\gamma} \tag{1.1}$$

The spectrum presents several key features: it follows a power law above a few GeV with an index of approximately  $\gamma=2.7$  up to roughly  $10^{15}\,\mathrm{eV}$ . Near  $10^{15}\,\mathrm{eV}$ , a knee appears and the spectrum softens from index  $\gamma=2.7$  to about  $\gamma=3.1$  [26]. These cosmic rays

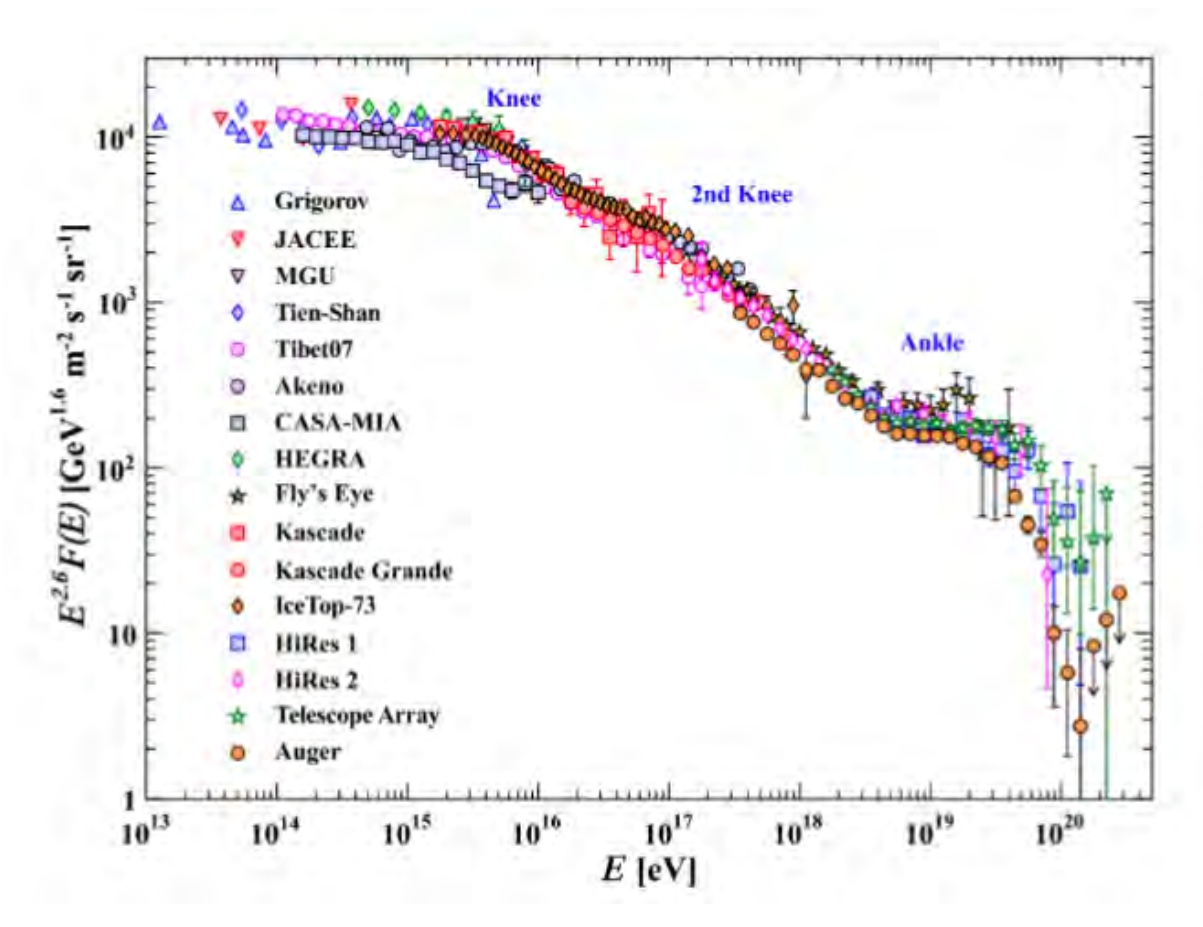


Figure 1.1: Cosmic ray energy spectrum measured by air-shower experiments. Figure is taken from [1].

are commonly attributed to galactic accelerators reaching their maximum energy and to 465 higher-energy protons escaping the galactic magnetic field [27]. Between the knee and the second knee, the spectrum continues to soften up to about  $8 \times 10^{16} \, \text{eV}$ . At the second knee 467 (  $8 \times 10^{16} \, \text{eV}$ ), the spectrum steepens further to an index near  $\gamma = 3.3 \, [27,28]$ . This attribution 468 is that likely heavier nuclei reach their maximum energies before they can escape the galaxy's 469 magnetic field. Around  $4 \times 10^{18}$  eV, the ankle marks a hardening of the spectrum. This is 470 often interpreted as the transition to extragalactic dominance, where the galaxy's magnetic 471 field can no longer confine cosmic rays. An alternative explanation invokes energy losses 472 from interactions between cosmic-ray protons and CMB photons. At the highest energies

- above  $5 \times 10^{19}$  eV, there is a rapid steepening of the spectrum known as the Greisen-Zatsepin-
- Kuzmin (GZK) cut off [29]. This is where cosmic rays interact with photons from the CMB
- and lose their energy, which explains the sharp spectral cutoff.

#### 477 1.1.2 Cosmic Ray Origins

- The potential galactic sources of cosmic rays include supernova remnants, pulsars, and many
- others. Several candidate sources beyond our galaxy include active galactic nuclei, gamma-
- 480 ray bursts, starburst galaxies, and galaxy clusters.

#### 481 Supernova Remnants (SNRs)

- Shock waves from exploding stars accelerate particles through first-order Fermi acceleration.
- $_{483}$  SNRs are considered the dominant source of galactic cosmic rays below  $10^{15}$  eV.

#### 484 Active Galactic Nuclei (AGNs)

- AGNs are bright regions at the centers of galaxies where a supermassive black hole pulls in
- gas. As matter spirals inward, some is ejected in relativistic jets perpendicular to the disk.
- This produces high-energy gamma rays and potentially high-energy neutrinos. Depending
- on their jet orientation and appearance to Earth viewers, AGNs are classified as Seyferts,
- radio galaxies, quasars, or blazars. When a jet points at Earth, the AGN is seen as a blazar.
- 490 In 2017, IceCube detected and identified neutrinos associated with blazar TXS 0506 + 056
- as one of the sources of cosmic rays [30, 31]. In 2022 IceCube has also identified a nearby
- Active Galaxy, NGC 1068, as the steady source of high-energy neutrinos [23].

#### 493 Gamma-Ray Bursts (GRBs)

Gamma-ray bursts are brief, extremely bright gamma-ray flashes lasting up to several hundred seconds. They are randomly distributed in the sky and thus extragalactic. Leading
models associate them with either massive stellar core collapse (long-soft GRBs) or compact binary mergers, such as neutron star-neutron star or neutron star-black hole systems
(short-hard GRBs). They launch ultra-relativistic fireball jets that produce gamma rays
and are expected to emit high-energy neutrinos.

#### $_{500}$ 1.1.3 Astrophysical neutrinos

In the Standard Model of particle physics, neutrinos are electrically neutral, nearly massless elementary particles that interact only via the weak force and gravity. They exist in three flavors, electron ( $\nu_e$ ), muon ( $\nu_{\mu}$ ), and tau ( $\nu_{\tau}$ ), each associated with a corresponding charged lepton (see Fig. 1.2). The Fig. 1.3 shows the energy spectrum of natural and man-made neutrinos.

Astrophysical high-energy neutrinos are conventionally produced when protons are accelerated to very high energies in cosmic sources and then interact to create short-lived particles
that decay into neutrinos. In a pp interaction, cosmic rays interact with gas near their source
and generate pions, kaons, neutrons, and other short-lived heavy hadrons as per Eq. (1.2).

$$p^{+} + p^{+} \longrightarrow \pi^{\pm}, \pi^{0}, K^{\pm}, n, \dots$$
 (1.2)

In a  $p\gamma$  interaction, cosmic rays may also interact with ambient radiation around the source, producing unstable hadrons as shown in Eq. (1.3).

#### **Standard Model of Elementary Particles**

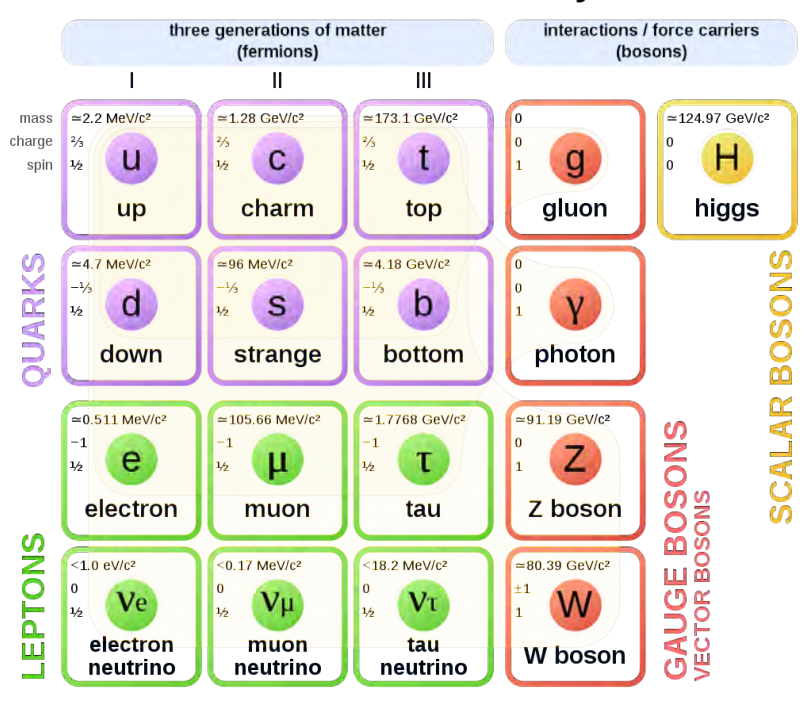


Figure 1.2: Neutrinos in the Standard Model of particles. The figure is taken from [2].

$$p^{+} + \gamma \longrightarrow \Delta^{+} \longrightarrow n + \pi^{+}$$

$$p^{+} + \gamma \longrightarrow \Delta^{+} \longrightarrow p + \pi^{0}$$
(1.3)

Neutral pions from both pp and  $p\gamma$  interactions decay into gamma-ray photons Eq. (1.4).

These photons can be detected by imaging Cherenkov telescopes, such as Fermi-LAT [25].

$$\pi^0 \longrightarrow \gamma + \gamma$$
 (1.4)

Charged pions decay into muons and muon neutrinos according to Eqs. (1.5). Those
muons subsequently decay to produce electron neutrinos plus additional muon neutrinos.

This chain yields approximately twice as many muon neutrinos as electron neutrinos and
produces no tau neutrinos at the source, resulting in an initial flavor ratio of 1 : 2 : 0.

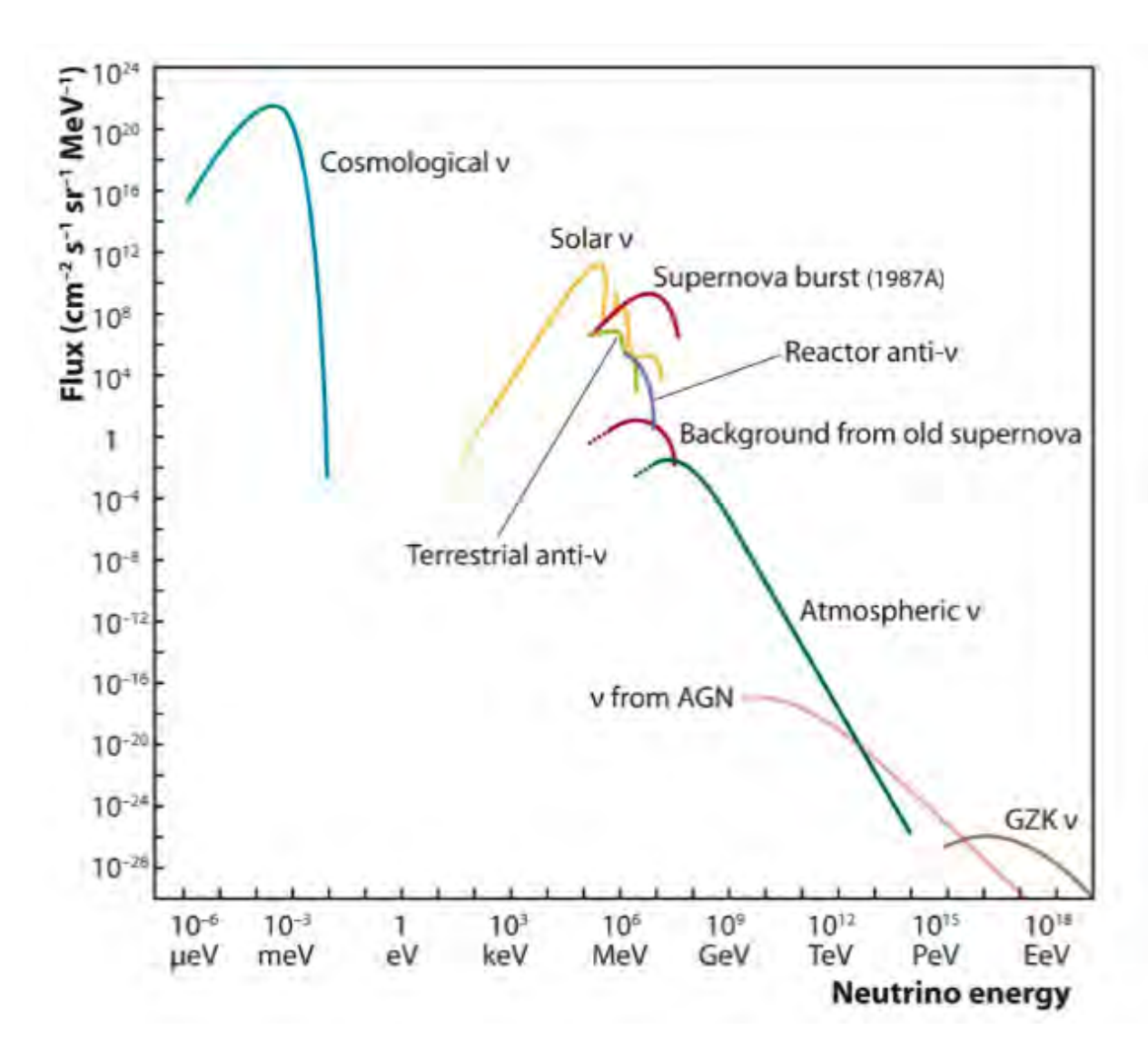


Figure 1.3: Neutrino energy spectra from different neutrino sources. The atmospheric neutrino flux (green) dominates the astrophysical neutrino flux from diffuse neutrino emission from AGN (pink) up to 100 TeV. This plot is taken from [3].

Over cosmic distances, neutrino flavor oscillations continuously swap flavors, and this ratio

is changed to an observed ratio of 1:1:1 when they reach the Earth.

520

$$\pi^{+} \longrightarrow \mu^{+} + \nu_{\mu} \longrightarrow e^{+} + \nu_{e} + \bar{\nu}_{\mu} + \nu_{\mu}$$

$$\pi^{-} \longrightarrow \mu^{-} + \bar{\nu}_{\mu} \longrightarrow e^{-} + \bar{\nu}_{e} + \nu_{\mu} + \bar{\nu}_{\mu}$$

$$(1.5)$$

One of the main challenges in detecting astrophysical neutrinos is the significantly greater

abundance of atmospheric neutrinos (see Fig. 1.3). The atmospheric neutrinos are produced when cosmic rays collide with the atmosphere, generating mesons that subsequently decay into neutrinos. Their spectrum consists of two components: conventional neutrinos fall steeply at high energies and are created from the decay of pions and kaons. Prompt neutrinos are from heavier mesons that yield a harder spectrum.

## 1.2 High-energy Neutrino detection

Neutrino events are detected indirectly by measuring Cherenkov radiation emitted from relativistic secondary charged particles produced in neutrino rare interactions with matter. These photons are collected by an array of photomultiplier tubes (PMTs). By analyzing the number of detected photons and their arrival times, the properties of neutrinos, such as direction, energy, and type, can be determined.

#### 532 1.2.1 Neutrino Interaction

At the energy relevant to neutrino telescopes, neutrinos interact via neutrino-nucleon deepinelastic scattering (DIS). This interaction involves a high-energy neutrino with a typical
energy greater than 20 GeV, which interacts with an individual quark inside the target
nucleon (proton or neutron), resulting in momentum transfer and leading to the nucleus
breaking into its constituent quarks and gluons. For a neutrino interacting with a nucleon in
the DIS process, the theoretical formulation of the differential cross-section has been reviewed
in Ref. [32] and discussed in Refs. [33–35].

Since neutrinos interact very weakly, the neutrino cross-section is generally very low.

Below 10 TeV, theory predicts that the cross-section grows roughly linearly with neutrino

energy [35, 36], so higher-energy neutrinos are more likely to interact. On the other hand, the flux of astrophysical neutrinos decreases sharply with energy and can reach a rate of one event per year, as shown in Fig. 1.3. Hence, a very large neutrino telescope (see Sec. 1.3) of the order of a cubic kilometer scale is needed to do neutrino astronomy [37, 38].

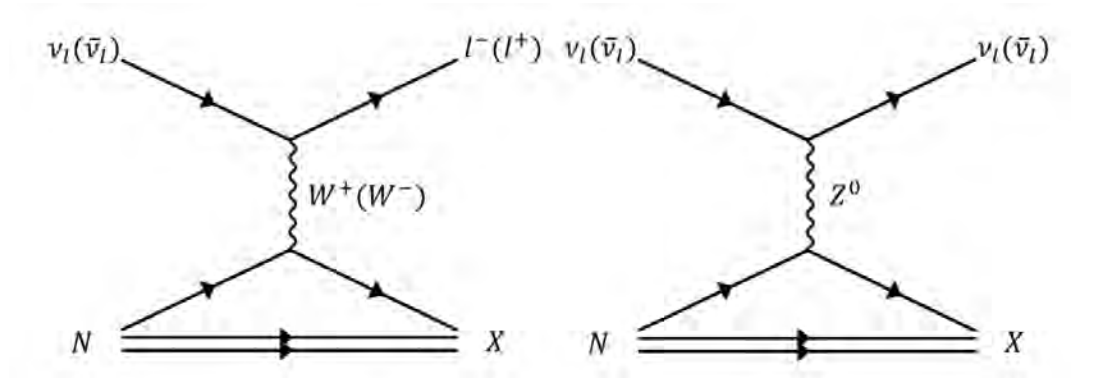


Figure 1.4: Feynman diagram for neutrino-nucleon deep inelastic scattering for Charged-Current (left) and Neutral-Current (right) interaction channels. Diagram taken from Ref. [4].

$$\nu_l + N \longrightarrow l^- + X \quad (CC)$$

$$\nu_l + N \longrightarrow \nu_l + X \quad (NC)$$
(1.6)

For this weak DIS interaction, there are typically two types of interactions: neutralcurrent (NC) interactions and charged-current (CC) interactions, as illustrated in Fig. 1.4
and Eq. (1.6). For CC interaction, a neutrino exchanges a  $W^{\pm}$  boson, resulting in the
production of an outgoing charged lepton  $l(e, \mu, \tau)$  and hadronic cascade (X) in the final
state as shown in Fig. 1.4 and Eq. (1.6). For an NC interaction, there is an exchange of a
boson, resulting in the production of a hadronic cascade (X) in the final state and an
outgoing invisible neutrino of the same flavor as the incoming neutrino.

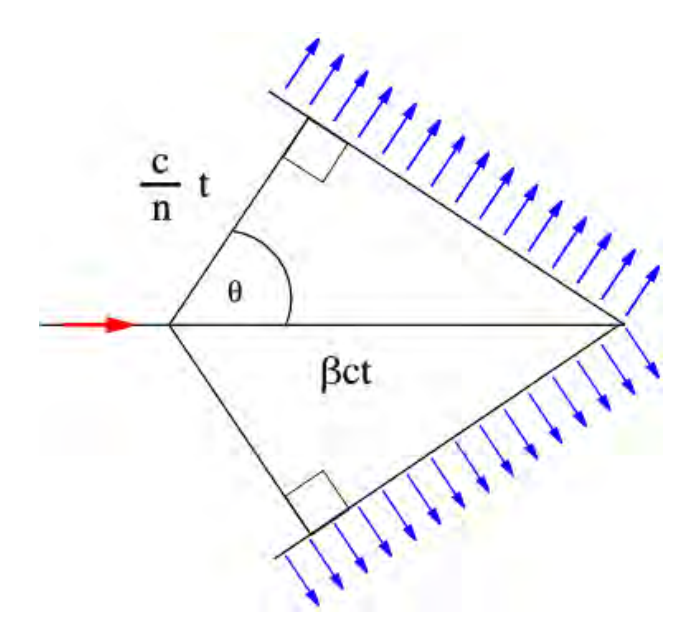


Figure 1.5: The geometry of the Cherenkov radiation. Figure from Ref. [5]. The blue arrow shows the direction of Cherenkov radiation. The red arrow shows the particle traveling at speed  $v_p$  such that  $\frac{c}{n} < v_p < c$ . Where  $v_p = \beta c$  and  $\frac{c}{n}$  is the speed of light in the medium.

#### 553 1.2.2 Cherenkov Radiation

Cherenkov radiation occurs when a charged particle travels through a medium at a speed greater than the phase velocity of light in that medium. Pavel Aleksyevich Cherenkov first observed the effect in 1937 [39]. From this condition necessary to produce Cherenkov radiation  $\beta > c/n$ , for a charged particle of rest mass m, the threshold kinetic energy a particle must have for Cherenkov emission to occur can be derived from the total energy  $E = \gamma mc^2 = \frac{mc^2}{\sqrt{1-\beta^2}}$  and is given by Eq. (1.7).

$$K_{\min} = mc^2 \left( \frac{1}{\sqrt{1 - \frac{1}{n(\lambda)^2}}} - 1 \right)$$
 (1.7)

The Cherenkov radiation is emitted at a fixed angle  $\theta_c$  with respect to the particle's direction. This angle, given by Eq (1.8), depends on the medium refractive index. The Cherenkov angle is approximately  $\theta_c = 41^\circ$  (42°) for relativistic particle with  $\beta \approx 1$  and

refractive index for water (ice) n = 1.35 (1.32).

$$cos(\theta_c) = \frac{1}{\beta n(\lambda)} \tag{1.8}$$

where  $\beta = v/c$  is the ratio of the speed of the particle to the speed of light in vacuum.

The number of Cherenkov photons emitted per unit path length and per unit wavelength of the charged particle is given by the *Frank-Tamm formula*, provided by Eq. (1.9) from Ref. [40]. The emission profile is peaked toward the blue near-UV part of the spectrum, and the angular emission profile is peaked at the Cherenkov radiation.

$$\frac{d^2N}{dxd\lambda} = \frac{2\pi\alpha z^2}{\lambda^2} \left( 1 - \frac{1}{\beta^2 n(\lambda)^2} \right) \tag{1.9}$$

where  $\alpha$  is the fine-structure constant, z is the charge of the particles in units of elementary charge, and the index of refraction,  $n(\lambda)$ , is a function of wavelength.

### $_{571}$ 1.2.3 Event Signatures

In this section, we introduce the event signatures observed in a neutrino observatory. Highenergy neutrinos interact via neutral current (NC) and charged current (CC) processes with nuclei, producing a hadronic cascade in all cases. CC interactions also yield a charged lepton of flavor e,  $\mu$ ,  $\tau$ . The resulting charged particles emit Cherenkov light, which is recorded by PMTs. The pattern (in terms of time, charge, and position) of detected photons depends on the type and flavor of the interaction.

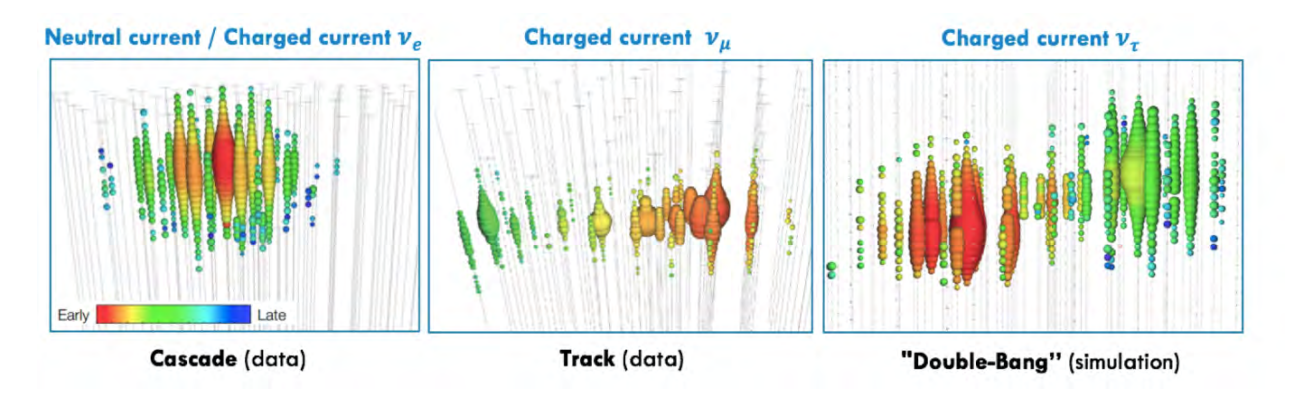


Figure 1.6: Neutrino interactions signatures

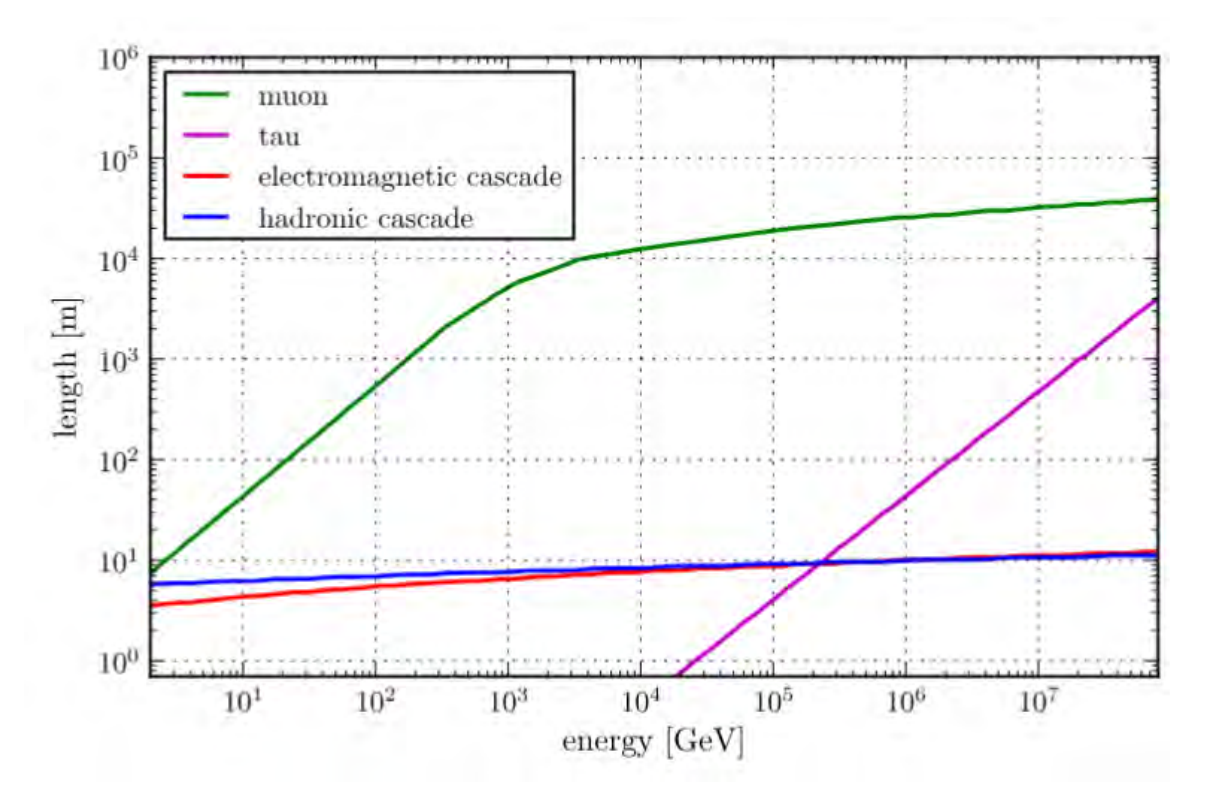


Figure 1.7: Particle mean free path lengths. Figure taken from [6].

#### Cascade signature

Cascade signatures come from CC electron neutrino interactions. Electrons produced in neutrino-nucleon DIS charged-current interactions lose energy via ionization,  $e^+$   $e^-$  pair production, bremsstrahlung, and photo-nuclear interactions. Electrons have a significantly smaller mass compared to muons and tau particles. They lose energy at a much faster

rate. At high energies, their energy losses are dominated by bremsstrahlung. This creates energetic photons, which then convert into  $e^+e^-$  pairs. The new electrons radiate more 584 bremsstrahlung photons and repeat the cycle. This chain forms an electromagnetic cascade. 585 Both CC and NC deep-inelastic neutrino interactions produce a hadronic cascade of 586 secondary particles, primarily pions. Charged pions decay mainly into muons and neutrinos, 587 thereby propagating the hadronic shower. Neutral pions decay into photons, which initiate accompanying electromagnetic cascades. Hadronic cascades are only 10 m long, so NC events 580 appear as point-like in the detector volume, resulting in nearly isotropic cascades. The CC 590  $\nu_e$  produces similar electromagnetic cascades (see Fig. 1.7). 591

#### 592 Track signature

The charged-current deep-inelastic scattering interaction of a muon neutrino produces the outgoing muon. Due to its longer lifetime (2.2  $\mu$ s) and larger mass compared to the electron, a muon can travel a greater distance before losing all its energy. As shown in Fig.1.7, muons travel only meters at a few GeV but extend to several kilometers by  $\approx 1$  TeV. At these energies, a detected muon can originate from outside the detector volume. The long track that muons leave in the detected volume, as shown in Fig.1.6, leads to improved direction reconstruction but poor energy resolution reconstruction compared to cascades.

Muons propagate through matter losing energy via ionization (continuously) and stochastic radiative processes. The main radiative processes are  $e^+$   $e^-$  pair production, bremsstrahlung, and photo-nuclear interactions [41]. The plot in Fig. 1.8 shows muons' energy losses in water. At energies below 1 TeV, losses are dominated by ionization. At energies above 1 TeV, radiative losses dominate over ionization. At high energies, these radioactive energy losses scale linearly with energy and can produce other electromagnetic cascades along the muon's

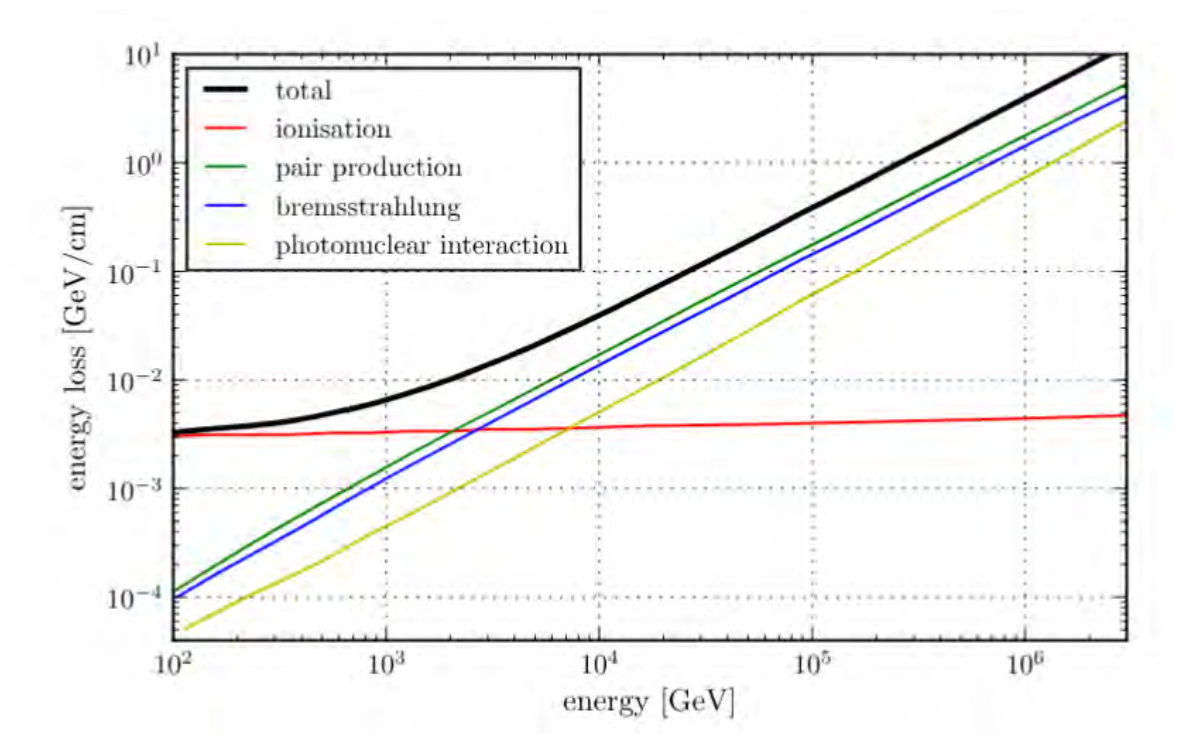


Figure 1.8: Muon energy loss. Figure taken from [6].

path. The average muon energy loss per distance  $\frac{dE}{dx}$  is approximated by the Eq. (1.10)

$$-\frac{dE_{\mu}}{dx} = a + bE_{\mu} \tag{1.10}$$

where the constant term a represents ionization and the term proportional to  $E_{\mu}$  represents the sum of radiative processes. The values of  $a=0.00268~{\rm GeV\,cm^2/g}$  and  $b=0.47\times 10^{-5}~{\rm cm^2/g}$  for muon in ice [41]. Solving the differential equation gives the average range of a muon,  $R=\frac{1}{b}\ln\left(1+\frac{b}{a}E_{\mu}\right)$ , which gives  $\approx 2~{\rm km}$  for a muon with  $E_0=1~{\rm TeV}$  in Ice.

#### 611 Double-bang signature

The CC deep-inelastic scattering interaction of a tau neutrino produces the outgoing tau.

Taus have a short lifetime (lifetime  $\approx 0.29~ps$ ) and decay almost immediately once they are

produced. Their large mass (1.77 GeV) also suppresses radiative energy losses during their

short lifetime, and such losses matter mainly above about 100 PeV. The tau decays into mesons such as  $\pi$  and K mesons. The decay modes for tau are given by Eqs. (1.11) with their branching ratios [27].

$$\tau^{-} \longrightarrow \nu_{\tau} + \text{Hadrons}, \qquad BR = 64.79\%$$

$$\tau^{-} \longrightarrow \nu_{\tau} + \bar{\nu}_{e} + e^{-} \qquad BR = 17.82\%$$

$$\tau^{-} \longrightarrow \nu_{\tau} + \bar{\nu}_{\mu} + \mu^{+} \qquad BR = 17.39\%$$

$$(1.11)$$

As can be seen from Eqs. (1.11), tau decay modes primarily produce hadronic (64.79%) 618 and electromagnetic (17.82%) cascades. At high energy, the tau can travel a large distance 619 as shown in Fig. 1.7. The CC interaction of tau neutrinos produces hadronic cascades and 620 electromagnetic cascades at different interaction vertices. Tau can only travel about 50 621 meters per PeV before decaying [42, 43] (also see Fig. 1.7). Therefore, only at sufficiently 622 high energies can a neutrino telescope distinguish the two cascades from a charged-current 623 tau-neutrino event in a signature called double-bang as shown from simulation in Fig. 1.6 and as discussed in Refs. [34,44]. At lower energies, CC  $\nu_{\tau}$  signatures look like other event 625 types: if the tau decays to a muon, it mimics a CC  $\nu_{\mu}$  track; otherwise, it appears as a 626 cascade indistinguishable from CC  $\nu_e$  or from any-flavor NC interactions. 627

## 528 1.3 Existing Neutrino Telescopes

This section provides a brief overview of the history of neutrino astronomy development, adapted from the discussion in Ref. [45]. The Deep Underwater Muon and Neutrino Detector (DUMAND) project, from 1976 to 1995, aimed to construct the first deep-ocean high-energy neutrino detector. DUMAND was the first effort marking the transition from initial ideas since 1960 to a large-scale experimental development of a high-energy neutrino telescope [45, 46]. The original envisioned cubic-kilometer array with over 20,000 PMTs proved to be beyond the technical and financial reach of the time. DUMAND scaled its plan from a grand standard array to the smaller DUMAND-II Octagon: 216 PMTs on eight outer strings plus one central, about 100 m wide, 230 m tall, to be installed 4.8 km deep, 30 km off Hawaii. These steps established the engineering, deployment, and calibration concepts later adopted by subsequent underwater and under-ice telescopes [45].

#### 640 1.3.1 Baikal-GVD

Based on the experience gained from the DUMAND project, a collaborator from DUMAND proposed the idea of constructing a cubic kilometer neutrino telescope in the deep waters of 642 Lake Baikal in 1980. Construction of the Baikal Neutrino Telescope (NT200) began in 1993. 643 Baikal NT200, an array of 192 Optical modules on eight strings 72 m long, was completed in 1998 [45]. The GVD-Baikal [7,47] is a neutrino telescope being constructed in Lake Baikal 645 (Russia). In 2015, a Gigaton Volume Detector (GVD) demonstrator cluster was successfully deployed. The first phase of construction began in 2016, with the deployment of the first 647 eight clusters. In 2021, GVD-I was completed with 8 clusters, each containing 288 optical modules, on an instrumented volume of 0.4 km<sup>3</sup>. As of January 2025 Baikal-GVD has 4104 649 optical modules installed on 114 vertical strings [7]. Each optical module has a downward-650 facing 10-inch PMT and sensors for pressure, humidity, and tilt. OMs are located at depths ranging from 750 m to 1275 m and are mounted on cables anchored to the lakebed, held 652 upright by buoys, forming vertical strings with 36 OMs spaced every 15 m. In winter, the 653 lake is fully ice-covered, with a thickness of around 40–50 cm. This supports the transport of heavy equipment and allows for smooth string deployment through drilled holes [7,47].

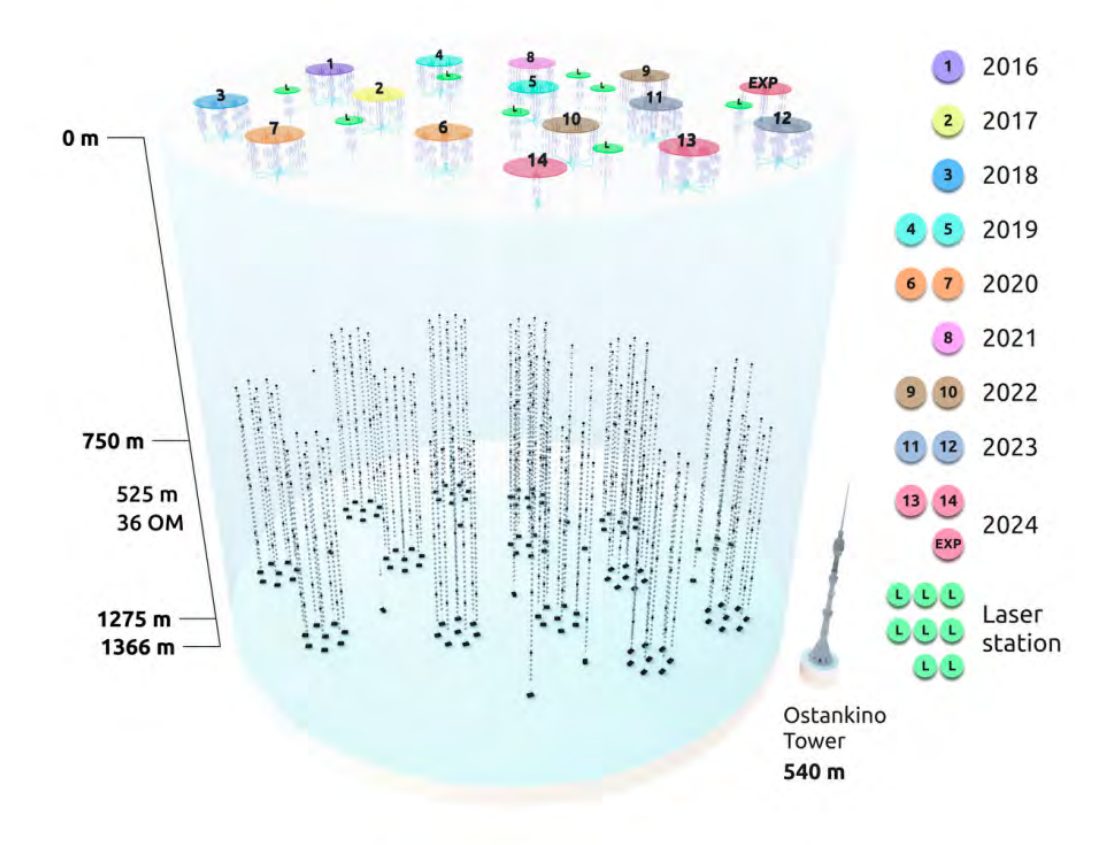


Figure 1.9: A schematic view of the Baikal-GVD telescope with its modular structure of clusters. Figure taken from [7].

#### $_{66}$ 1.3.2 $\mathrm{KM3NeT}$

The construction of the neutrino telescope in the Mediterranean sea also began in 1993 with
the NESTOR collaboration, which deployed a prototype in 2004. The ANTARES (Astronomy with a Neutrino Telescope and Abyss environment Research) is a neutrino detector deployed at 2475 km under the Mediterranean sea, approximately 40 km off the coast of Toulon
in France. ANTARES detector construction started in 2002 and was completed in 2008, and
aimed primarily to detect the neutrino flux of cosmic origin. ANTARES drew from the experience and know-how from the earlier DUMAND [46] effort and the operational Lake Baikal
detector, and it also shares certain design elements with the AMANDA/ICECUBE [48] ex-

periment at the South Pole [49]. ANTARES consisted of 12 strings of 450 m length each spaced about 70 m. Since then, the NESTOR, NEMO, and ANTARES projects joined efforts to start KM3NeT [45].

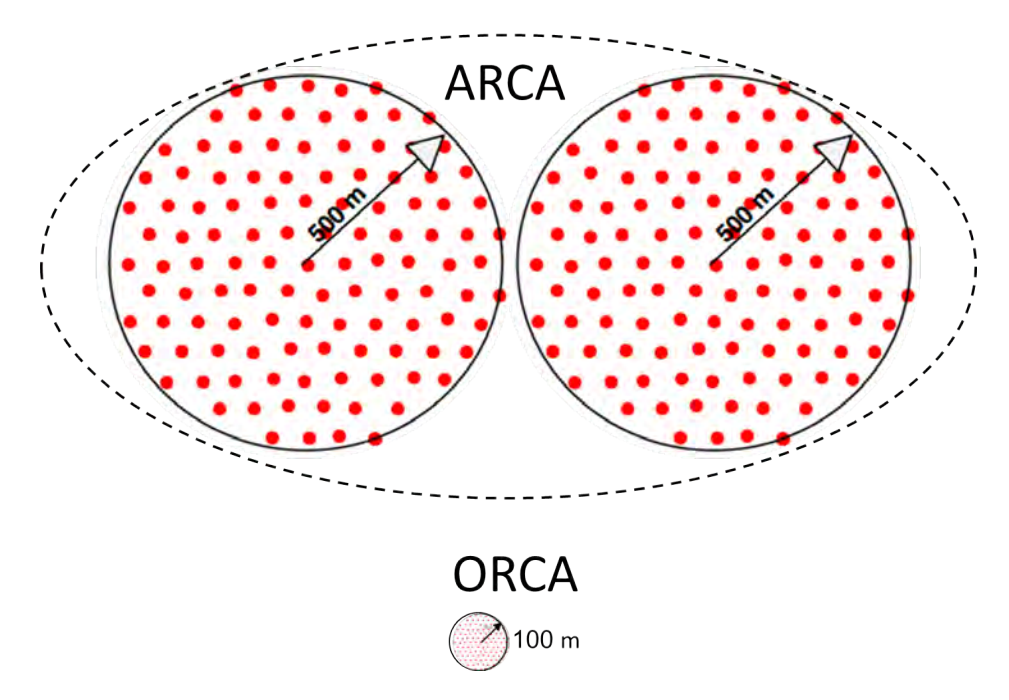


Figure 1.10: Comparison between KM3NeT's ARCA and ORCA detectors. Instrumented on about 1 km<sup>3</sup>, ARCA has 115 detection units in each block. Figure taken from the KM3NeT website [8].

The KM3NeT neutrino telescope is currently under construction [50]. It comprises two detectors: ARCA (Astroparticle Research with Cosmics in the Abyss), being deployed at a depth of 3500 m near Capo Passero (Italy), targets astrophysical neutrinos at high energies. ORCA (Oscillation Research with Cosmics in the Abyss), being deployed at a depth of 2500 m near Toulon (France), focuses on lower-energy atmospheric neutrinos for oscillation studies. Both detectors utilize the same multi-PMT optical module technology, but they differ in sensor spacing and in the total volume of water they are instrumented, with ARCA being sparse and kilometer-scale, and ORCA being compact and denser [51]. The Fig. 1.10 shows a scale comparison of ORCA and ARCA of KM3NeT.

KM3NeT uses multi-PMT Digital Optical Modules (DOMs) arranged on vertical Detection Units (DUs) and cabled to shore. Each DOM consists of 31 3-inch PMTs housed in a 678 17-inch diameter glass sphere. The lower DOM hemisphere has 19 PMTs facing downward, and the upper DOM hemisphere has 112 PMTs facing upwards [50, 52]. Each vertical line, 680 called a Detection Unit (DU), holds 18 DOMs suspended along it on two support ropes. The 681 DU is fixed to the seafloor and stabilized by underwater buoyancy, so it stays nearly upright. ARCA array is optimized for high-energy neutrino astronomy. The full ARCA comprises 683 two building blocks, totaling 230 DUs, providing a cubic-kilometer-scale instrumented volume for detecting neutrinos from astrophysical sources with energies ranging from 100 GeV 685 to 100 PeV. ARCA vertical height of each detection unit is about 700 m. The vertical 686 distance between optical modules on a detection unit is approximately 40 m and 100 m horizontal spacing. 688

ORCA is a compact, densely instrumented building block designed for atmospheric neutrinos in the tens of GeV range, with a focus on oscillation physics. It uses identical hardware to ARCA but with much closer spacing. ORCA is instrumented over approximately
0.004 km<sup>3</sup> and features 115 detection units. The optical modules are spaced vertically by
9 m on a detection unit and approximately 20 m between detection units. ORCA's purpose is to measure oscillation parameters and determine the neutrino mass ordering; first
lines were installed in 2017, with four lines operating by mid-2019, enabling time/geometry
calibrations and the selection of up-going neutrinos despite the small configuration.

#### 697 1.3.3 IceCube

The idea of building a neutrino telescope in deep ice at the South Pole emerged in 1988 with the idea to construct a 1 km<sup>3</sup> detector that guarantees the first detection and study of

the neutrino emission of cosmic origin [37,40,53]. However, the first AMANDA array was deployed in the summer of 1993/1994 [54]. The first two neutrino events were identified in the data record with a 4-string configuration [55], which by January 2000 had been upgraded to a full 19-string array consisting of a total of 677 optical modules [48]. AMANDA set strong upper limits on cosmic neutrinos for diffuse, point-source, and transient sources, such as gamma-ray bursts [56–59].

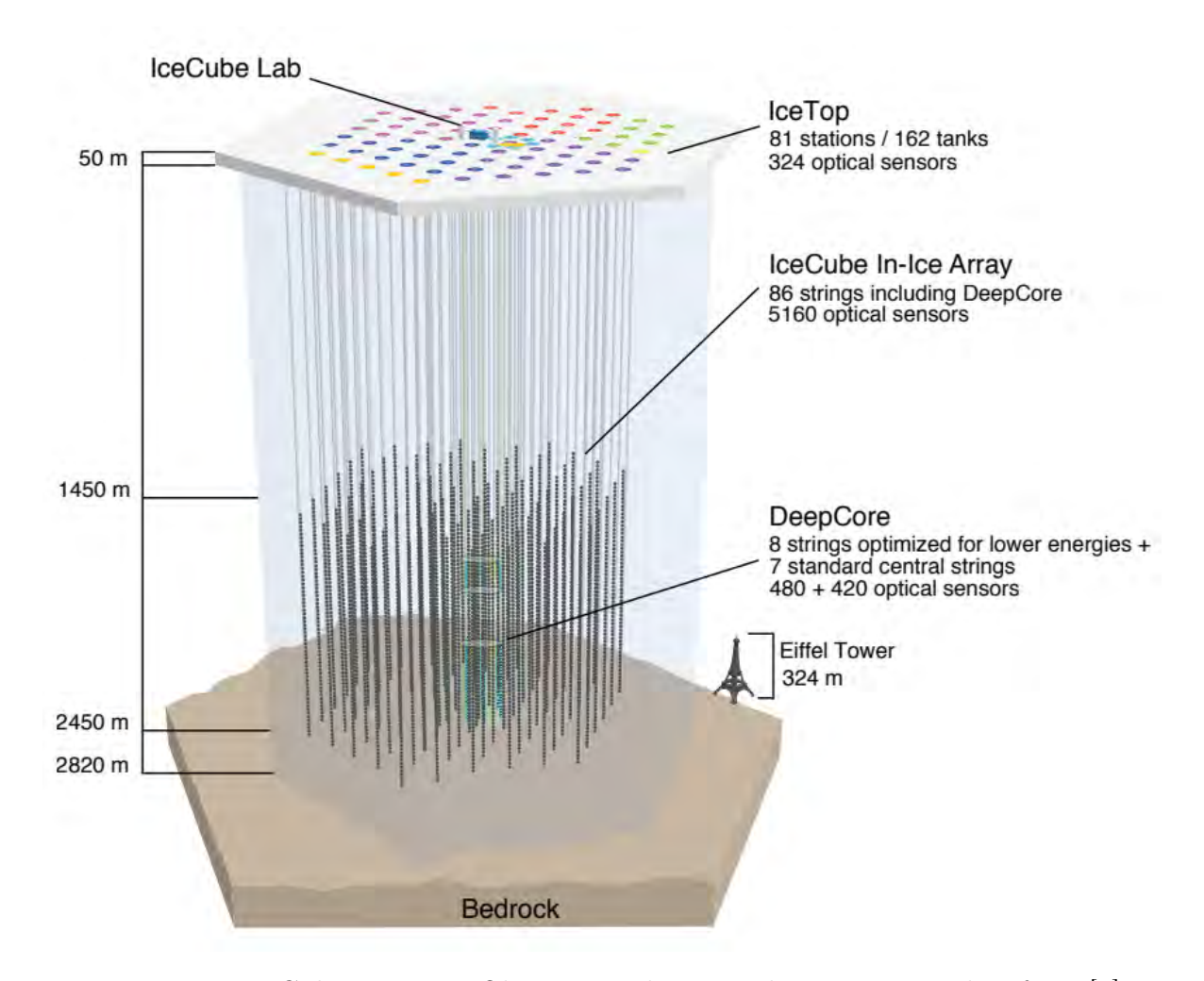


Figure 1.11: IceCube Neutrino Observatory layout. The Picture is taken from [9].

IceCube is a cubic-kilometer neutrino observatory at the South Pole, embedded 1450–2450 m deep in Antarctic ice. The array comprises 5, 160 digital optical modules (DOMs) on 86 strings. Each string consists of 60 DOMs mounted on a single cable with twisted copper wire

pairs, with a vertical spacing of 17 m between DOMs. The strings are laid out on a triangular grid within a hexagonal footprint, separated horizontally by 125 m [9]. This configuration is optimized to be most sensitive to astrophysical neutrinos with energies from about TeV to PeV scales [9]. Atmospheric muons and neutrinos are significant backgrounds. IceCube handles them by utilizing the Earth as a filter and by identifying up-going or down-going events within the detector.

IceCube has made several necessary steps in neutrino astronomy. The first detection of a high-energy astrophysical neutrino flux (2013) [60] opened the field, later followed by multi-messenger evidence linking a high-energy neutrino to the blazar TXS 0506+056 [30]. It also identified that the active galaxy NGC 1068 is a steady source of neutrinos [23]. Most recently, IceCube identified neutrinos coming from our own Milky Way. Using ten years of data and machine-learning tools, they observed an excess of neutrinos along the Galactic plane, with strong statistical confidence  $4.5\sigma$  [61].

Despite IceCube's advances, most detected astrophysical neutrinos have not been associated with known sources, suggesting the need for more sensitive telescopes. A northernhemisphere array, such as P-ONE, will complement the sky coverage of IceCube (South
Pole) and other telescopes, including KM3NeT and Baikal-GVD, by improving sensitivity
to southern-sky targets 2.1.

# Chapter 2

# The Pacific Ocean Neutrino Experiment

### 2.1 Introduction

During the past decade, the IceCube Neutrino Observatory [9] has been at the forefront of neutrino astronomy, detecting a diffuse flux of extraterrestrial neutrinos [60] and successfully identifying some sources of these high-energy neutrinos as discussed in Refs. [23, 30, 61]. However, most astrophysical neutrinos detected by IceCube have not been associated with known astronomical sources. There is a need for additional neutrino telescopes with improved sensitivity to discover new sources of neutrinos.

The P-ONE neutrino telescope will be deployed in the northern hemisphere's Cascadia 736 Basin, off the coast of Vancouver Island, utilizing the existing Ocean Networks Canada 737 underwater deep-sea infrastructure for deployment, data transmission, and cabling. P-ONE 738 will be built in the northern hemisphere, where it will be able to view the southern sky using 739 both cascades and track events. With this, it can view the inner regions of the Galactic plane, observing both sources of neutrinos and diffuse emission from the Galactic plane, as 741 discovered by the IceCube Neutrino Observatory [61]. In addition, since P-ONE will be 742 deployed in water using the latest technology for precise timing measurement [62] to fully exploit the reduced photon scattering, P-ONE will be able to reconstruct neutrino events 744 from astrophysical sources with higher precision, improving the sensitivity of the neutrino telescope for the Southern sky. Thus, P-ONE will complement existing or under-construction neutrino telescopes, such as IceCube, KM3NeT, Baikal GVD, and TRIDENT, to cover the full sky and provide more observational windows for neutrino astronomy as illustrated in Fig. 2.1.

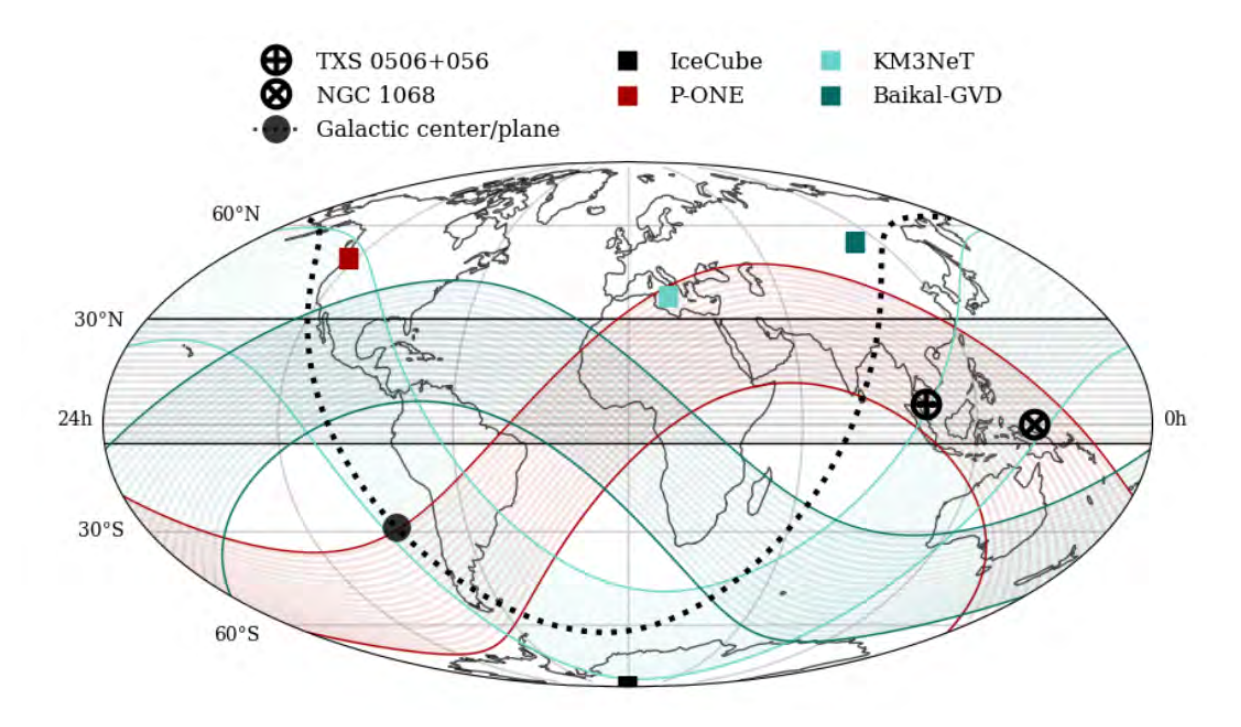


Figure 2.1: Neutrino Telescopes field of view. P-ONE's location in the northern Pacific Ocean will provide a sky view complementary to existing and planned neutrino telescopes in Antarctica, the Mediterranean, Lake Baikal, and the western Pacific [10]. Image courtesy. Lisa Schumacher.

In this chapter, we discuss two pathfinder missions deployed in 2018 and 2020 to study the optical properties and bioluminescence background of the Cascadia basin, identified as the site for the P-ONE deployment. We briefly discuss the potential P-ONE detector instrument, focusing on its design layout. We then introduce the test geometry used for event simulation in Ch. 3, track reconstruction in Ch. 4, and point source sensitivity forecast in Ch. 5.

### 5 2.2 Ocean Networks Canada

The P-ONE detector will be deployed in the Cascadia Basin region, located 2600 meters below sea level [16]. The detector will significantly benefit from the existing deep-sea infrastructure of Ocean Networks Canada (ONC) [63], utilizing its capabilities for construction, deployment, power, and data communication. The ONC shore station at Port Alberni will host the P-ONE data acquisition system as well.

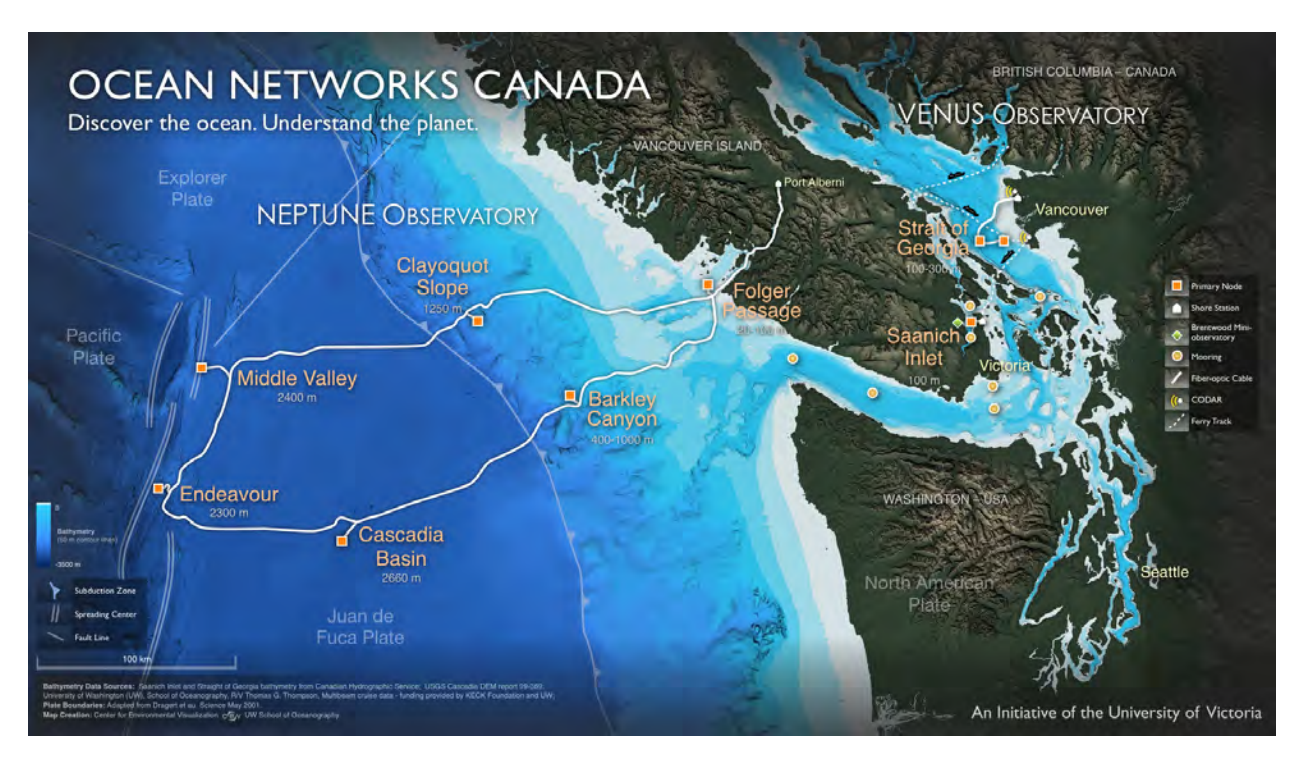


Figure 2.2: The Ocean Network Canada NEPTUNE Observatory. The STRAW and STRAW-b instruments for site investigation were deployed at the Cascadia Basin node. P-ONE is planned to be deployed at the Cascadia Basin as well. Image courtesy of ONC.

### 2.3 P-ONE Pathfinder Missions

In collaboration with Ocean Networks Canada, P-ONE collaboration deployed two pathfinder missions at the Cascadia Basin site, operated by Ocean Networks Canada (ONC), to inves-

tigate the feasibility of constructing and deploying the P-ONE detector. In 2018, STRAW (STRing for Absorption length in Water) [11,64–67] was deployed to investigate the optical 765 properties of the deep-sea water at the Cascadia Basin. The primary objectives of STRAW were to measure the attenuation length of deep-sea water at the Cascadia Basin and to 767 assess the background light resulting from both bioluminescence of marine organisms and 768 radioactive potassium, <sup>40</sup>K, present in the seawater. In 2020, STRAW-b was also deployed about 40 m from STRAW to further characterize the site [68]. The main goal of STRAW-b 770 was to study in detail the background noise, primarily from bioluminescence. Additionally, 771 its mission aims to assess the feasibility of deploying long mooring lines for P-ONE for long-772 term operation [12,68]. After a successful operational period following their deployment, the 773 two STRAW pathfinder missions were decommissioned in the summer of 2023.

#### $_{\scriptscriptstyle{775}}$ 2.3.1 STRAW

STRAW consisted of two 146 m vertical mooring lines separated by 37 m, instrumented with eight modules in total. The modules include three light emitter modules called Precision Optical Calibration Modules (POCAM), and five light sensor modules called STRAW Digital Optical Modules (sDOM). The blue string has one POCAM module and three sDOM modules, while the yellow string has two POCAM modules and two sDOM modules, as shown in Fig. 2.3. STRAW mooring lines were deployed at a depth of about 2600 meters at the Cascadia Basin. STRAW was deployed using a tow-down approach, in which the mooring lines were lowered into the water and then anchored to the sea floor.

The Fig. 2.4 and Fig. 2.5 show a POCAM and an sDOM picture, respectively, taken by
the ROV camera during the STRAW deployment inspection in 2018. Each POCAM is made
up of two glass hemispheres, with each hemisphere housing a system that enables isotropic

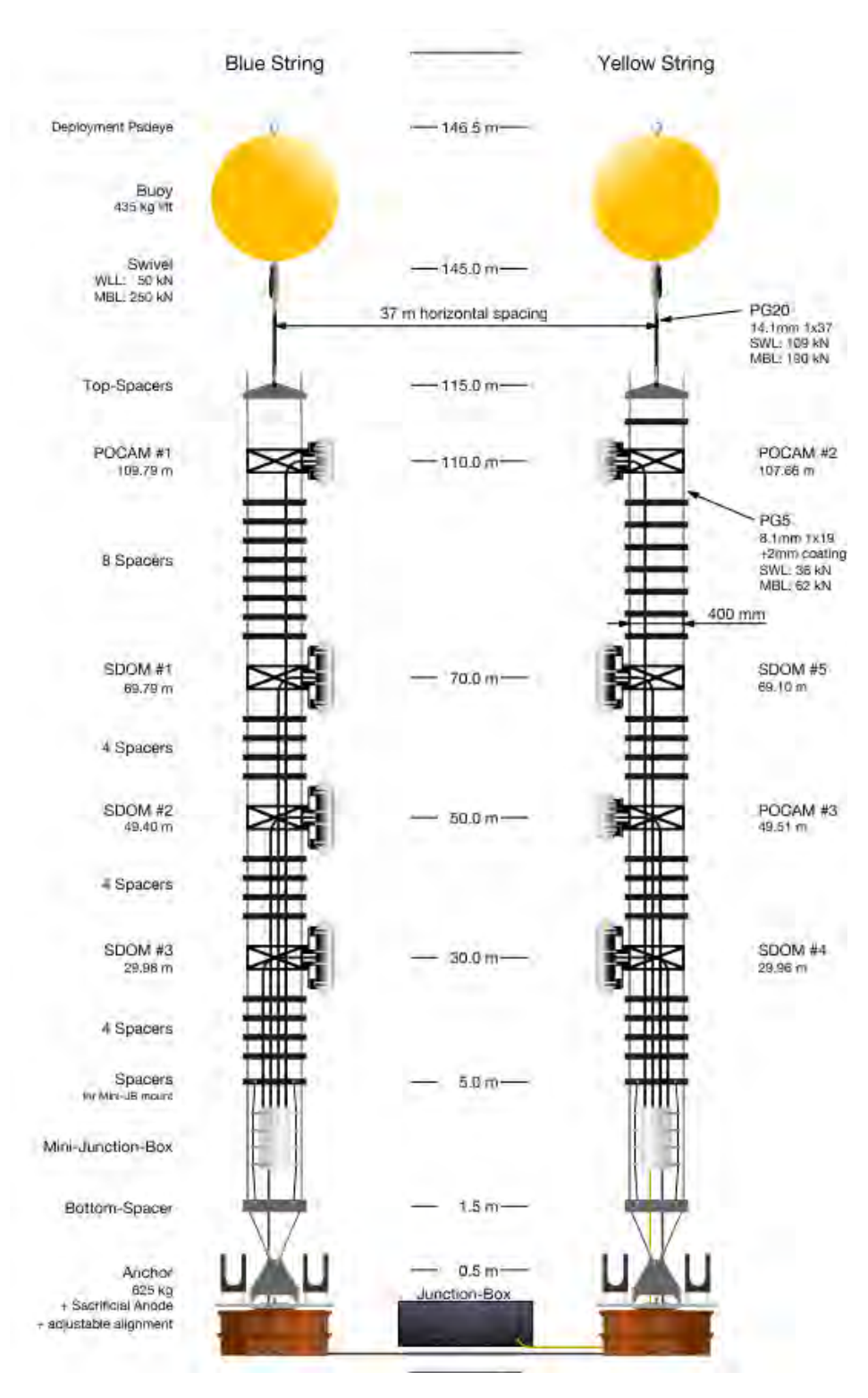


Figure 2.3: Detailed technical sketch of the two STRAW mooring lines showing all modules' exact (measured) geometry.

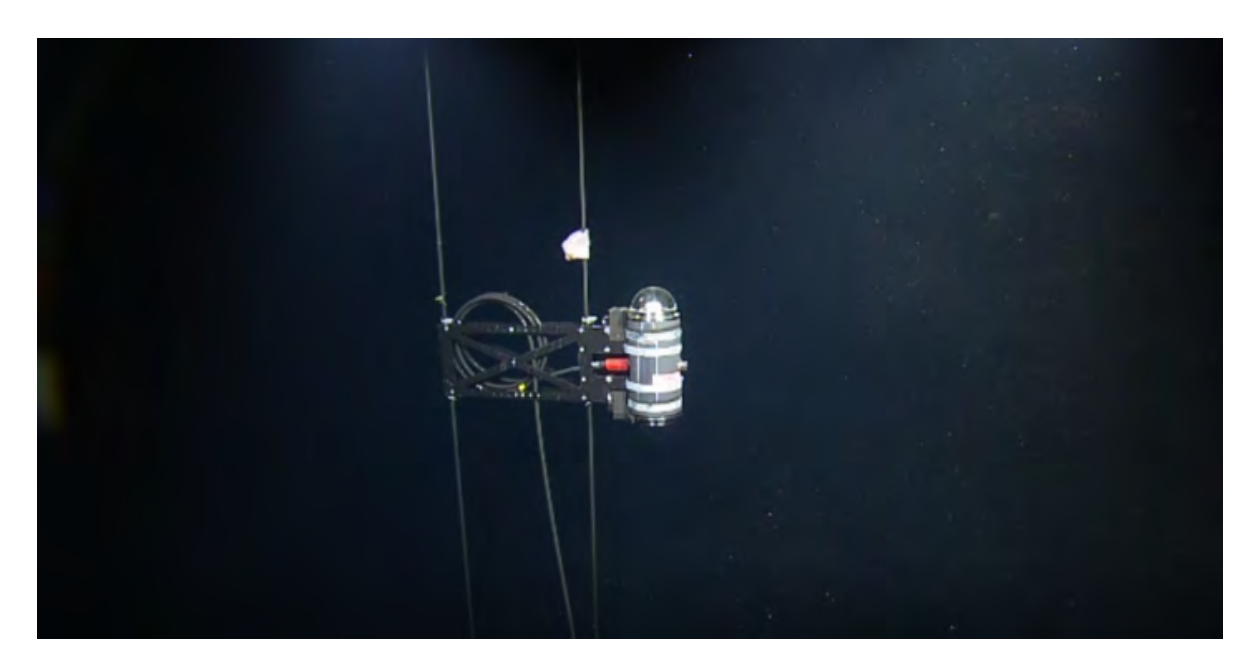


Figure 2.4: POCAM2 deployment Inspection in June 2018. Pictures courtesy of ONC.



Figure 2.5: sDOM4 deployment Inspection in June 2018. Pictures courtesy of ONC.

light emission from different multi-length LEDs. The adjustable light intensity allows the POCAM flash of light to reach a different range of distances for different possible attenuation lengths. The range of LED light frequencies used is from 350 nm to 600 nm. The sDOM houses two 3-inch PMTs to detect photons from POCAMs. The two PMTs are encapsulated

in a titanium cylinder, with one PMT facing upward and the other facing downward. The sDOM also monitors background light from radioactivity and bioluminescence. The expected maximum value for absorption length for blue and UV light in deep ocean water is about 50 meters [69]. The modules are 30 m, 50 m, 70 m and 70 m heights from the sea floor. This ensures that pairs of STRAW emitters and receivers cover a range of baselines comparable to the maximum absorption length expected for optical Cherenkov radiation. More details about the POCAM and sDOM are discussed in Refs. [64–67].

The measurement of light attenuation length is based on the fact that the POCAM 798 intensity is isotropic and consistent between flashes. By comparing the detected intensity in 799 sDOMs with different distances from the POCAM, the exponential decrease of light intensity 800 with distance is measured, and the attenuation length is extracted from the shape of the function. The sDOMs at fixed time intervals record photon hits arrival times from POCAM. 802 To compute the attenuation length from the arrival time information recorded at the sDOM, 803 the number of hit events that are recorded at the sDOM is determined. The attenuation 804 length is obtained by fitting the measured data to the parametric model built for the STRAW 805 detector, given by,

$$\mu(r) = \frac{p \cdot s}{4\pi r^2} \exp\left(\frac{-r}{l_{\text{attenuation}}(\lambda)}\right)$$
 (2.1)

where  $\mu$  is the mean number of photons detected by an sDOM, r is the distance between sDOM and POCAM. The terms p and s are functions that include all POCAM and sDOM nuisance parameters that can be measured, and  $l_{\text{attenuation}}$  is the model fit parameter. More details about the STRAW attenuation measurement can be found in [11,44].

For STRAW, four different LEDs were used to obtain measurements of attenuation length at four different wavelengths of 365 nm, 400 nm, 450 nm, and 585 nm. Fig. 2.6 shows the re-

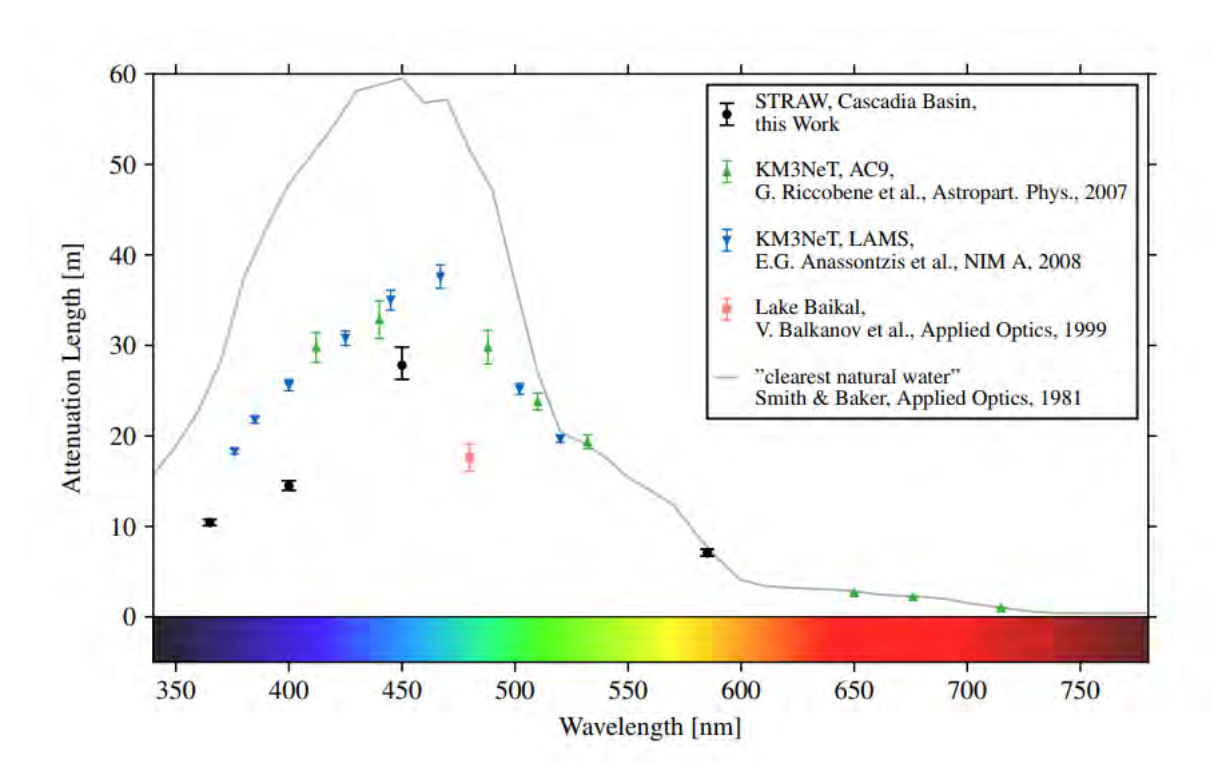


Figure 2.6: Attenuation length measurement results from two years of STRAW data are shown in black. The figure is taken from Ref. [11].

sults of the analysis of two years of STRAW data compared to measurements from previous experiments [70–72]. It shows the attenuation length as a function of light emitter wavelength. The results show optical attenuation of about  $(28 \pm 2)$  m at 450 nm corresponding closely to the Cherenkov light spectrum relevant for a neutrino telescope.

Over four years (2019-2023), the STRAW Pathfinder mission has monitored and measured background rates in the Cascadia basin. Potassium-40 ( $^{40}K$ ) decays contribute a baseline background for PMT rates, while bioluminescence activities contribute a highly variable background. The analysis of STRAW data revealed a baseline contribution to background rates of about 10 kHz from both Potassium-40 [11,44].

#### $_{ m 822}$ 2.3.2 STRAW-b

832

STRAW-b is a 444 m long mooring line consisting of ten Optical modules. Fig. 2.8 (left) illustrates the position of each module type from the bottom of the sea-floor. The bottom right picture of Fig. 2.8 shows an example of one of the STRAW-b modules on the mooring line. Each STRAW-b module is connected to a copper/fiber hybrid cable for power supply and data transmission. All data cables are connected to a mini junction box (MJB) located on the seafloor which also sends data to the NEPTUNE data infrastructure [68]. The picture in Fig. 2.7 was taken during STRAW-b deployment.

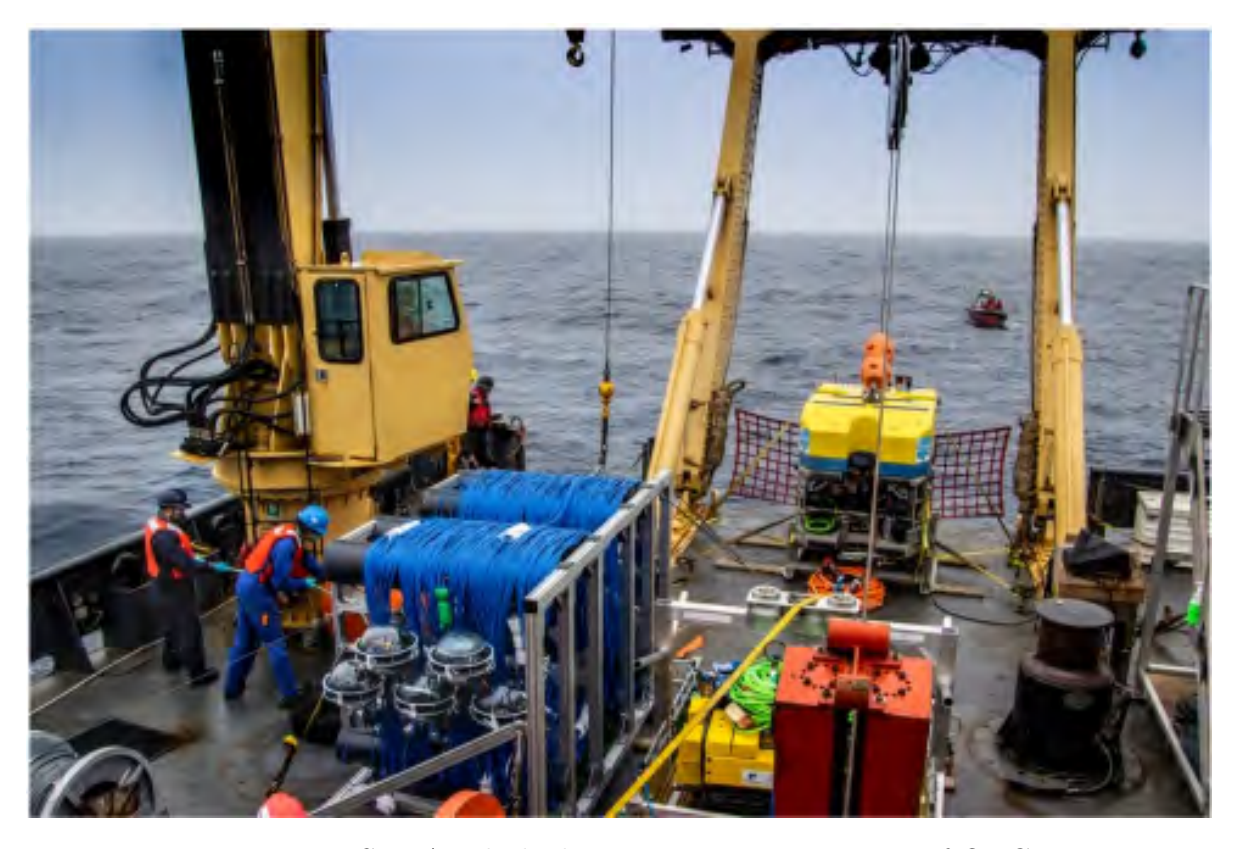


Figure 2.7: STRAW-b deployment. Picture courtesy of ONC.

The following highlights the types of modules instrumented in STRAW-b. More details about these modules can be found in Refs. [12, 68, 73].

1. Standard modules (3): Each Standard module is enclosed in a 13-inch glass pressure

sphere. These three standard modules do not contain any PMT. They are primarily to monitor environmental conditions rather than photon detection. The module contains a sensor to monitor environmental pressure, temperature, and humidity. It also has an accelerometer and magnetometer to determine orientation and account for mooring motion caused by currents.

833

834

835

836

837

853

854

855

- 2. LiDAR Modules (2): The two light detection and ranging (LiDAR) modules are
  used to confirm STRAW's attenuation length results and to measure the scattering
  and absorption lengths independently. They use a laser diode to emit 10 ns light pulse
  at 450 nm into the surrounding ocean water, and a lens collects the back-scattered
  photons and directs them to a micro PMT, which records how the signal intensity
  changes over time. In addition, LiDAR modules include two high-intensity broadspectrum LEDs oriented downward, which are used to calibrate the PMT-spectrometer
  modules placed below them, as shown in Fig. 2.8.
- 3. Muon-Tracker Module (1): This module aims to detect muons passing within the
  module. It contains two rectangular scintillator tiles coupled to Silicon photomultipliers
  (SiPMs). This module can help in calibration and validate pointing accuracy for future
  P-ONE modules. When a muon is measured, the setup constrains its path so that it
  must traverse through the two scintillators of the module. This known track can then
  be compared against the trajectory reconstructed from the detector's Cherenkov light
  data.
  - 4. **PMT-Spectrometer Modules (2)**: The two modules aim to characterize the bioluminescence emissions. Each PMT-Spectrometer module consists of three distinct sensors, all oriented upwards within the module: These are twelve PMTs as spectrom-

eters, a camera, and a mini-spectrometer. Each of the twelve PMTs uses its own lens and wavelength filter. These three distinct sensors enable independent measurements of bioluminescence. The camera is used to capture the bioluminescence, including the position.

856

857

858

859

- 5. Mini-Spectrometer Module (1): This module is composed of five Mini-Spectrometers
  and a low-light camera. The components used in this module are identical to the components used in the PMT-Spectrometer module. It complements the measurement of
  the spectrum of the PMT-spectrometer and the camera. The Mini-Spectrometer offers
  higher spectral resolution than the PMT-spectrometer and camera, but is less sensitive
  to light.
- 6. Wavelength-Shifting Optical Module (1): The WOM is an experimental module
  designed to boost signal-to-noise ratio by separating the photosensitive area from the
  PMT cathode. It uses a transparent, wavelength-shifting-painted tube with a PMT
  at each end to absorb UV light and guide up to 73% (41% in ice/water) of re-emitted
  photons by total internal reflection to the PMTs [12].

The results from two years of data revealed that bioluminescent activity produces highly variable photon rates, ranging from steady baselines of a few kilohertz to a maximum detection rate of 10 MHz, which is rarely exceeded. Most of the steady baseline emission was linked to Potassium-40 decay, while transient spikes from bioluminescence showed seasonal and periodic behavior, tied to ocean currents. The bioluminescence emission spectrum was found to be concentrated mainly in 440 - 500 nm wavelengths [12].

The STRAW and STRAW-b pathfinder missions have provided essential insights into the optical properties and environmental conditions of the Cascadia Basin site, which are



Figure 2.8: A sketch diagram of the STRAW-b mooring line(left), indicating the locations of all modules. Examples on the right show the housing glass sphere Standard Module (top right) and the PMT-Spectrometer (middle right and bottom right). Figure taken from [12]

required for the successful operation of the P-ONE neutrino telescope. These insights have

informed the beginning of the P-ONE design process.

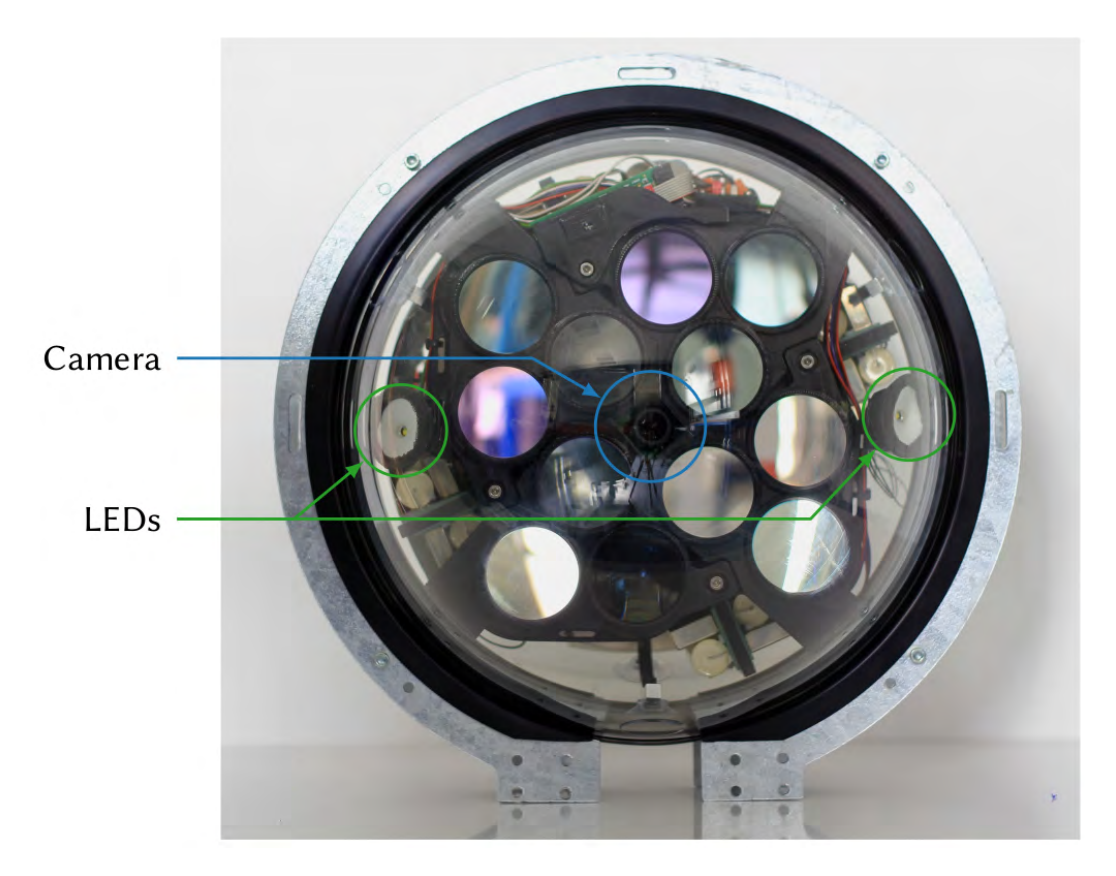


Figure 2.9: STRAW-b PMT-Spectrometer module. Image taken from Ref. [12].

### 2.4 P-ONE Instrumentation

Following the successful deployment, operation, and decommissioning of the P-ONE pathfinder 882 missions from 2018 to 2023, the P-ONE collaboration is now developing and working towards 883 realizing P-ONE arrays of detector instruments. The next milestone is the deployment of the 884 first instrumented mooring line in 2026, P-ONE-1, followed by the deployment of the P-ONE 885 demonstrator [74]. P-ONE-1 will be a 1 km long mooring line from the seafloor consisting 886 of 20 modules evenly spaced by 50 meters along the mooring line. Among the 20 modules 887 on the line, up to three will be P-ONE Calibration modules (P-CALs), and the rest will be 888 standard P-ONE Optical Modules (P-OM) [13, 15]. PONE-1 will be held in position by an 889 anchor at the seafloor and pulled taut by a sub-sea top buoyancy float that are attached to 890

the top of the cable.

892

910

communication and power to each instrument module on the mooring lines. At each module, 893 a connection is realized by branching off the needed copper and fiber lines via a titanium 894 end can, while the rest continue to the next module. A multi-layered sealing system helps 895 to preserve the operation in case a cable, an instrument, or a module fails on the mooring line. The titanium cylinders carry the mechanical load as integral parts of the detector line. 897 The mooring line cable terminates in a mooring junction box (mJB), which acts to control 898 the modules' power and interface with the NEPTUNE network of Ocean Networks Canada 890 (ONC) for data transmission. More technical details about P-ONE-1 development can be 900 found in Refs. [13]. P-ONE-1 is planned to be deployed using a bottom-up approach by pre-packing the 902  $\approx 1000$  m line on a deployment frame that is lowered to the seafloor in a deployment 903 frame. An ROV will inspect the structure, connect it to the NEPTUNE infrastructure 904 before the unfurling process. The ROV will release the buoyancy, and the line will be lifted ans by its buoyancy. The ROV will remain at the deployment frame monitoring the unfurling process [13]. A successful construction and deployment of P-ONE-1 will serve as a blueprint 907 for the refinement of the subsequent mooring lines. It will provide valuable lessons for the development of optical modules, calibration modules, mooring line deployment, and the 900

P-ONE will use a segmented single hybrid fiber-optic and copper cable to carry fiber

# 911 2.4.1 P-ONE Optical Module

operation of a complete mooring line.

A P-ONE Optical Module (P-OM) will be housed inside two 17-inch glass hemispheres attached to a mooring line using a titanium flange. Each hemisphere will contain 8 photomultiplier tubes (PMTs), for a total of 16 evenly spaced PMTs per P-OM. Each photomultiplier tube (PMT) has a programmable, self-regulated high-voltage power supply. The analog readouts of the PMTs are sent to the mainboard, where an ADC digitizes them at a sampling frequency rate of about 210 MHz. A high-voltage subsystem manages PMT power, while a field-programmable gate array(FPGA) provides the mainboard with a central control logic controls data acquisition, peripherals, synchronization, and communication [14,74].



Figure 2.10: Picture of P-OM prototype. Picture taken from Ref. [13].

### $_{220}$ 2.4.2 Calibration Systems

To accurately reconstruct incident event particle observables, the position of optical modules must be localized with high precision. Due to ocean currents, the position of mooring lines and their modules, the optical properties, and bioluminescence activity will change with time. Therefore, P-ONE will use a real-time monitoring and calibration system to deal with the effect of ocean currents [14]. The calibration system consists of beamed and isotropic



Figure 2.11: Picture of P-OM prototype. Picture taken from Ref. [13].

optical light pulsers, an acoustic positioning system, a camera system, and integrated devices to measure sedimentation, magnetic fields, and environmental parameters [14, 15, 75].

P-ONE will use P-ONE calibration modules (P-CAL) in addition to standard P-ONE Optical modules (P-OM). P-CAL will be a hybrid module for light detection, acoustic position, and calibration measurements. P-CAL modules will have the same design as the standard P-ONE Optical Modules but will replace 8 PMTs with optical calibration devices [75]. P-CAL will include optical light flasher, self-monitoring photosensors, a camera system as shown in Fig. 2.12(top right).

Each module P-ONE will be instrumented with 10 beamed sub-nanosecond light fashers of various wavelengths from 300 - 600 nm. These beamed pulsers will help to measure scattering, dispersion, and inter-module time synchronization. The diffuse flasher system in P-CAL will comprise 5 high-power nanosecond light pulsers, which sit under the white Teflon diffuser. The system will help generate well-calibrated isotropic flashes within the detector.

By measuring the intensity and arrival time of a flash at the other modules in the detector,

P-CAL can measure module efficiencies, water optical properties, and perform calibration of module positions. The optical position of the P-CAL diffuse flasher will be cross-checked by the acoustic position system within each module, as illustrated in Fig. 2.13.

The acoustic calibration system consists of an acoustic transceiver and acoustic receivers, 943 as shown in Fig. 2.13. Every P-OM and P-Cal module will house a piezo-acoustic receiver of the acoustic positioning system illustrated in Fig. 2.12. Two acoustic receivers are planned 945 to be installed in every P-ONE module. The measurement of the position of the P-OMs will 946 be based on measuring the time of flight (TOF) of the acoustic signals between emitters of known location and acoustic receivers. This acoustic positioning system will continuously 948 monitor the position of the mooring line and modules to a relative positioning resolution of 20 cm or better required for approximately 1 ns P-ONE PMTs timing resolution [62]. P-CAL 950 camera can take a picture from inside the module, which will help to monitor sedimenta-951 tion, biofouling, and bioluminescence activity near the P-CAL [75]. More details about the calibration system can be found in the following Ref. [15, 75, 76]. 953

## $_{\scriptscriptstyle{054}}$ 2.5 Detector Geometry Design

The optical attenuation length of ocean water (see Fig. 2.6) is smaller compared to that of
Antarctic ice (more than 100 m). Building an instrumented volume of the order of a km<sup>3</sup>
neutrino telescope at the Cascadia Basin with a uniformly infilled array structure of optical
sensors like IceCube will require thousands of instrumented lines. To reduce the associated

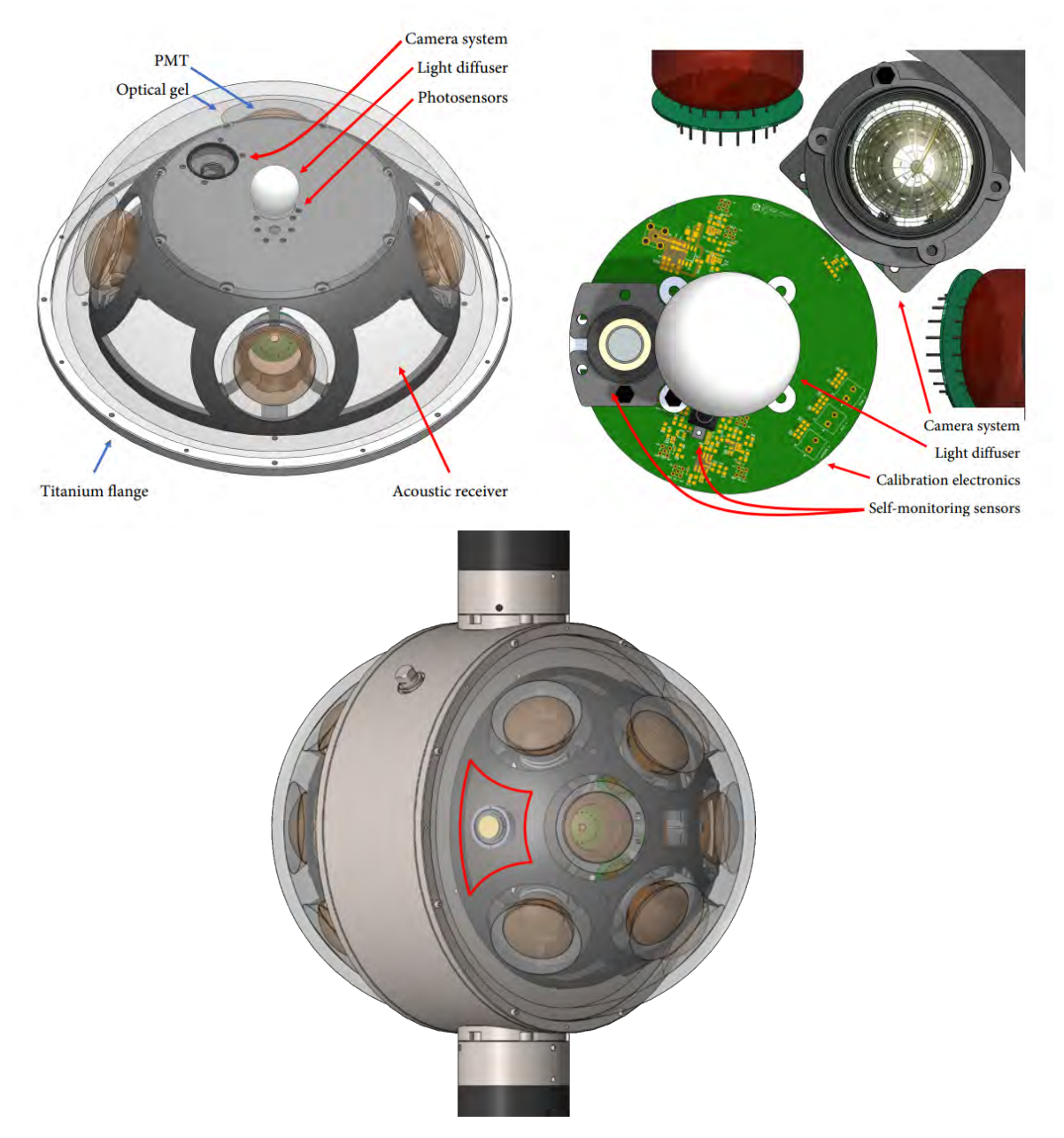


Figure 2.12: **Top left**: The P-CAL hemisphere layout view from CAD software. **Top right**: P-CAL interior optics, self-monitoring, and camera system. **Bottom**: Illustration of P-ONE optical module (P-OM) with integrated acoustic receiver highlighted in red. The top figures are taken from Ref. [14]. The bottom figure is taken from Ref. [15].

- high cost, P-ONE detector geometry is envisaged to have a clustered structure [16] similar to
- the Baikal-GVD detector (see Fig. 1.9). P-ONE is proposed to have 7 clusters, each cluster
- made of 10 mooring lines, as illustrated in Fig. 2.14.

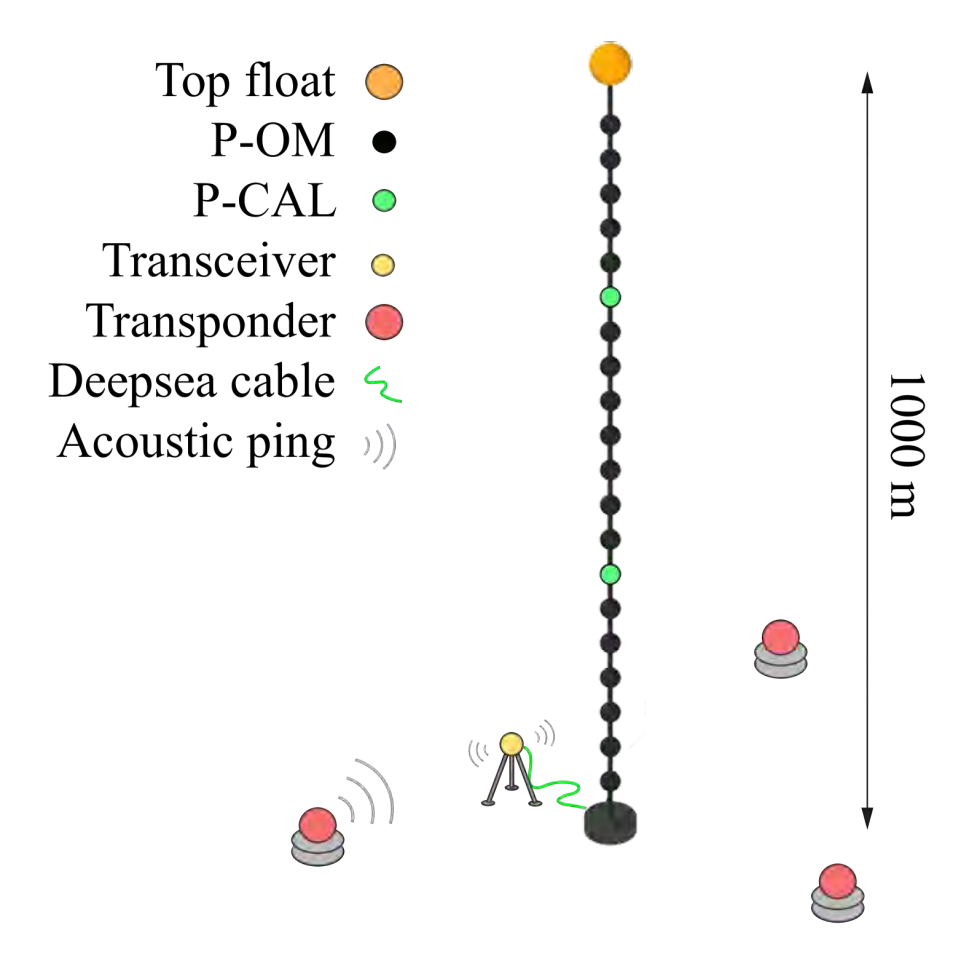


Figure 2.13: The figure shows the anticipated P-ONE acoustic positioning system. The three transponders(red) and acoustic transceiver (yellow) are all external to the P-ONE optical modules. The piezo-acoustic receivers will be housed in P-OMs(black) and P-CALs(green) as shown in Fig. 2.12. Two acoustic receivers are planned to be installed in every P-ONE module. The figure is taken from Ref. [15].

P-ONE detector geometry design optimization studies are currently an ongoing work by the P-ONE collaboration. The final geometry design will be determined by the one that maximizes the science output, while also considering cost and physical infrastructure constraints, and fits within the engineering constraints. The Fig. 2.15 shows a top view of the simulated detector geometry that we have used for the event Monte Carlo simulation (Ch. 3), reconstruction study (Ch. 4), and point sensitivity forecast study (Ch. 5).

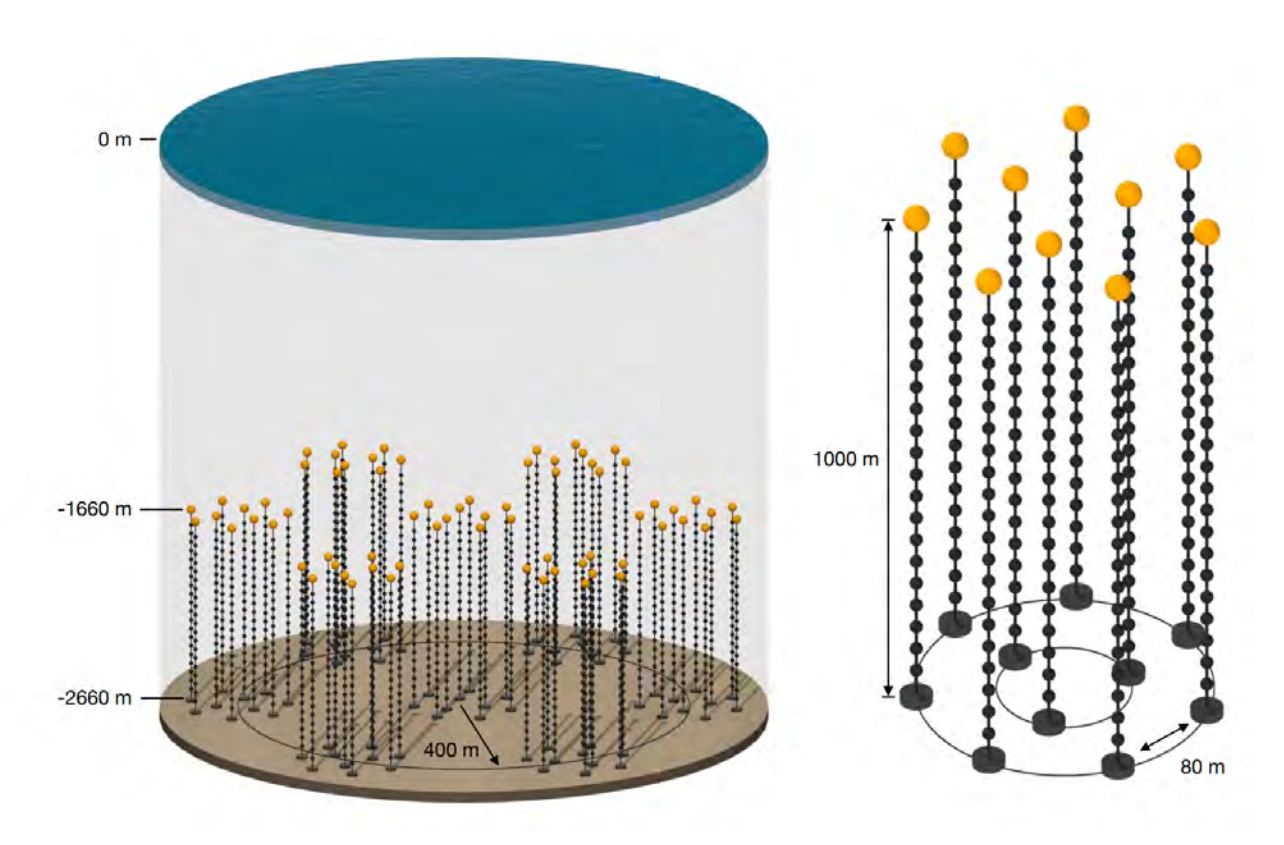


Figure 2.14: The plot on the left illustrates the P-ONE geometry configuration concept. P-ONE will be deployed in modules of seven clusters of mooring lines. The right plot shows a cluster consisting of ten mooring lines. The figure is taken from Ref. [16].

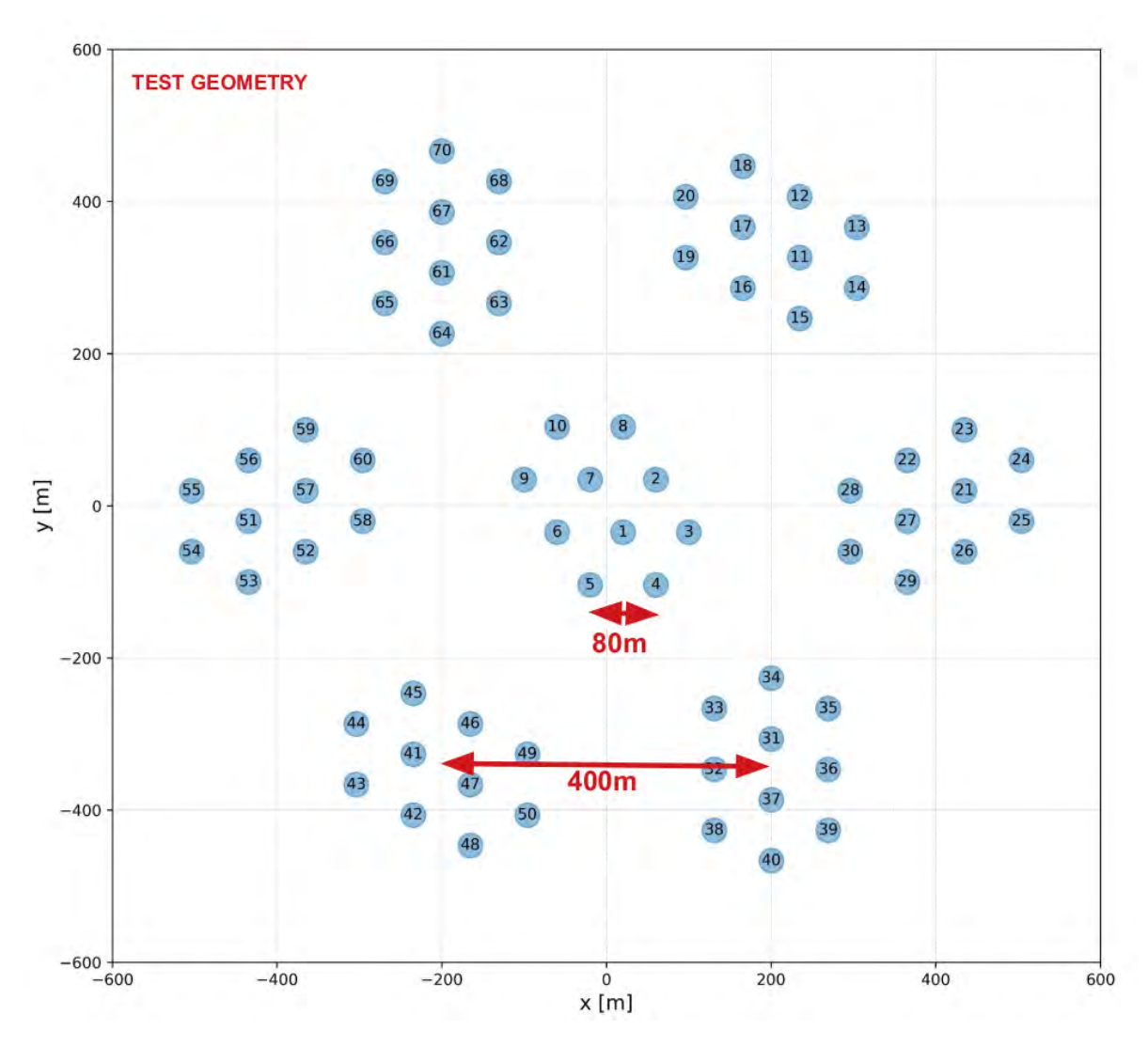


Figure 2.15: Top view of the simulated full 70-string P-ONE reference geometry. This test geometry has the following dimensions: The distance between cluster centers is 400 m. Each cluster consists of 10 mooring lines, each about 1 km long. The distance between the strings is about 80 m. Each string will contain 20 optical modules, and each optical module consists of 16 photomultiplier tubes [17]. The string-to-string spacing is based on a preliminary study [18].

# 968 Chapter 3

# 369 P-ONE Event Monte Carlo Simulation

Neutrino telescopes aim to detect light when a neutrino of astronomical origin interacts near or in the detector volume. However, the nature of the data recorded by a neutrino telescope also includes light from various sources. Atmospheric muons produce the majority 972 of triggered events [77, 78]. These occur when cosmic rays interact with the atmosphere, 973 producing mesons. These mesons subsequently decay into muons and can reach the detector from above. In addition to light from muons of atmospheric origin, noise hits originate from 975 the medium where the detector optical modules are deployed. For a detector deployed in deep-sea water, these include noise hits from bioluminescence and the decay of Potassium-40 977 processes, which are discussed more in Sec. 2.3. In the end, any real astrophysical neutrino 978 event will be contaminated by noise hits produced by these processes rather than by the atmospheric muon or any neutrino secondaries. We can also get entire events triggering 980 that do not contain any neutrinos or neutrino-induced secondaries, just atmospheric muons and noise hits, or (probably) even just bioluminescence without an atmospheric muon. We 982 usually call these background events.

### $_{984}$ 3.1 Simulation Flow

This chapter discusses the first detailed Monte Carlo event simulation for the Pacific Ocean
Neutrino Experiment. This involves generating both muon tracks and neutrino events in

the detector volume, propagating light from secondary particles in the detector medium, simulating the response of the optical module to the Cherenkov photon, and adding noise 988 hits. As a physical detector was not yet constructed at the time of writing this thesis, we 989 used the test geometry discussed in Sec. 2.5 to produce Monte Carlo simulations. This 990 geometry is not the final design of the detector geometry array. At the time of writing, 991 detector geometry optimization remains an ongoing effort to achieve a detector geometry that optimizes the science output while considering other engineering and cost constraints. 993 The first part of this simulation chain, shown in Fig. 3.1, from event generation to photon 994 propagation, uses tools previously used by the IceCube Collaboration to produce Monte 995 Carlo simulations. The detector response and trigger simulations utilize tools specifically 996 developed for the P-ONE Monte Carlo simulation.

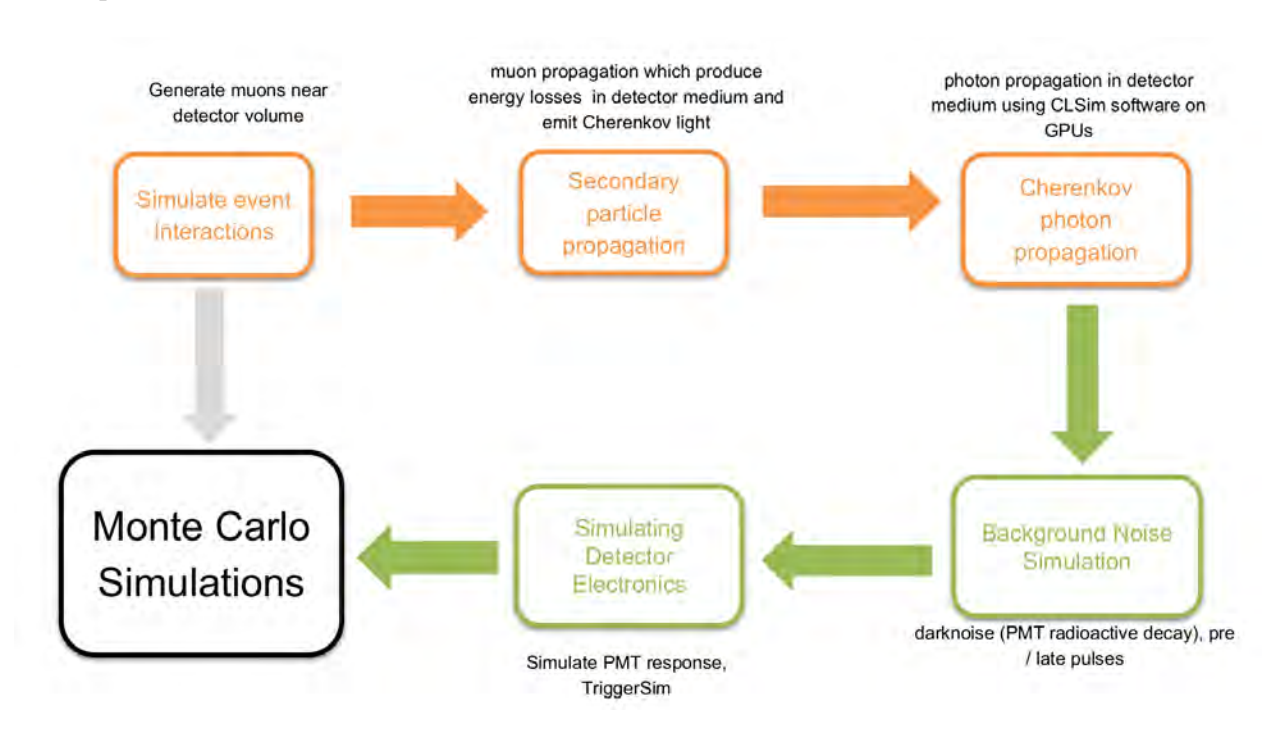


Figure 3.1: Simulation Chain

The diagram in Fig. 3.1 illustrates the simulation chain we used to produce events Monte
Carlo simulation for the PONE. The entire simulation chain runs on top of the IceCube

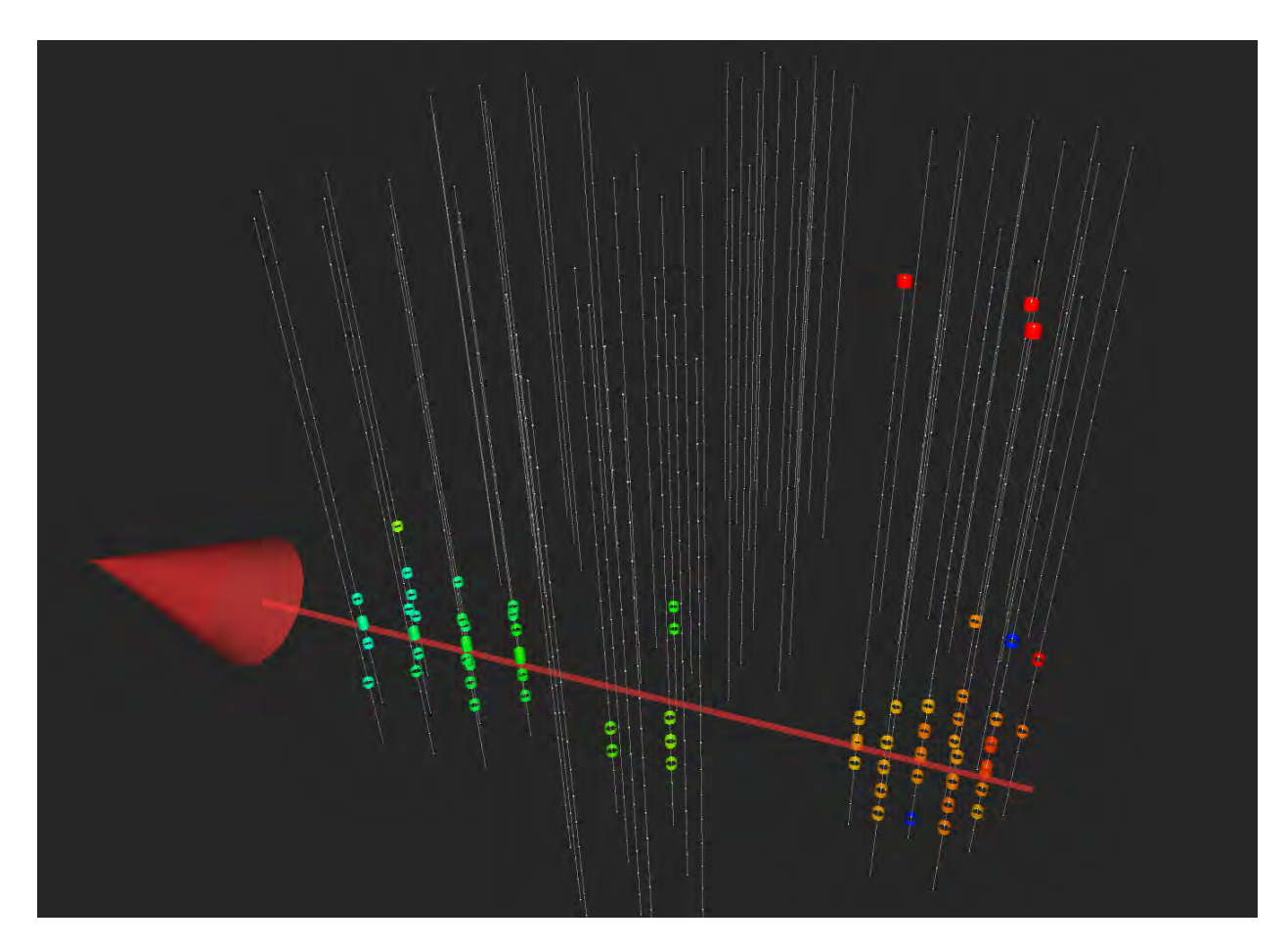


Figure 3.2: Display of an example of the simulated event at 500 TeV that crosses different clusters shown in the event viewer using Icetray software. The gray dots indicate the positions of individual DOM on the mooring line using simulated detector geometry in Fig. 2.15. The circle shows the simulated physics signal. Photoelectrons that arrived early are colored red, and those that arrived late are colored green.

Icetray software class. Each simulation step generates data stored in a serialized, tree-1000 based data structure, an I3-file. The screenshots in Fig. 3.3 and Fig. 3.4 show I3-Files in 1001 steam-shovel event viewer. This data can later be used to save additional information on the 1002 file or in any other data format for high-level analysis. We used high-performance computing 1003 clusters to generate and store these simulation datasets. The core modules of the simulation 1004 pipeline pone-offline were put together by Thomas McElroy. My contribution to the 1005 simulation part of the work focuses first on collaborating with Thomas McElroy on testing 1006 the simulation chain to work as expected, and secondly on using the pipeline to generate 1007

Monte Carlo datasets we used for building and testing track likelihood reconstruction and the Monte Carlo simulation dataset used for neutrino point source analysis Ch. 5.

The rest of the chapter details each step of the simulation chain. Sec. 3.2 discusses
the generation of events using the generator previously used by the IceCube collaboration.
Sec. 3.4 discusses the photon propagation method using the CLsim photon propagation software framework. Sec. 3.5 discusses an effort to simulate the detector response using basic assumptions.

### 3.2 Event Generation

#### 1016 3.2.1 Neutrinos Simulation

1029

To simulate neutrino events for the P-ONE, we have used the LeptonInjector [79], a software developed by the IceCube collaboration. LeptonInjector is a high-energy neutrino event
generator designed for large-volume Cherenkov detectors. LeptonInjector can generate a
neutrino flux of all flavors and a broad range of energies from 10 GeV to 100 PeV, which
is necessary for neutrino-nucleon deep inelastic scattering (DIS) regime and the Glashov
resonance (GR) interaction relevant for neutrino telescope.

Unlike neutrino generators [80,81], which start neutrino event simulation at the Earth's surface and simulate neutrino propagation through the entire Earth, LeptonInjector simulates neutrino events within and around the detector volume [79]. The neutrino event energy is sampled based on a single power-law spectrum. LeptonInjector samples the final state kinematics (energy and momentum transfer) of a generated event from pre-calculated spline tables of differential cross sections of relevant neutrino interactions [79].

The events generated at an arbitrary rate by LeptonInjector are re-weighted to match a

physical neutrino flux using LeptonWeighter. Neutrino fluxes are calculated using nuSQuIDS [82]. LeptonInjector uses a modified Preliminary Reference Earth Model (PREM) [83] to calculate the column depth for a neutrino on its path to the detector. LeptonWeighter uses nuSQuIDS to calculate the neutrino absorption probabilities and neutrino oscillation in matter and vacuum. This information is used to determine the probability that a neutrino of a specific flavor and energy arrives at the detector.

For the analysis discussed in Ch. 5, we used the LeptonInjector [79] to obtain a Monte
Carlo dataset sample of muon neutrino interaction events in the detector. These simulations
include muon neutrino events simulated in the energy range from 1 TeV to 1 PeV following
the  $E^{-1}$  energy spectrum. We simulated neutrino events arriving from all directions of the
sky, sampled uniformly over all azimuth angles and zenith angles.

### 3.2.2 Cosmic Ray Muons Simulation

CORSIKA (COsmic Ray SImulations for KAscade) is a program that has become the stan-1042 dard tool for simulating cosmic-ray air showers [84]. CORSIKA simulates the propagation 1043 of cosmic rays through the atmosphere, their interactions, and the resulting production of 1044 secondary particles, including muons and neutrinos. The simulation tracks these particles 1045 down to the surface level, accounting for energy losses and hadronic interactions, and can be 1046 weighted to match arbitrary cosmic-ray flux models. However, simulating entire air showers 1047 with CORSIKA is computationally intensive, especially when large sample sizes are needed 1048 to estimate rare background rates with sufficient statistical precision. 1049

To overcome these limitations, IceCube developed the MuonGun [85] based on MUPAGE [86]. Rather than simulating full air showers from the top of the atmosphere, MuonGun parameterizes the distribution of muons arriving at the detector based on previously run

CORSIKA simulations. This allows for rapid and efficient generation of large numbers of single-muon events, which is the largest background after veto selections. The energy distribution of injected muons can be customized, and the simulation can be reweighted to match different cosmic-ray flux models. This approach enables the production of much larger sample sizes than CORSIKA alone.

MuonGun is also used in specialized modes, such as the Floodlight mode, to simulate single muons near the detector volume. In this mode, it is used to simulate neutrino events instead of cosmic ray muons. This represents a simulation of charged current muon neutrino interactions. These simulated single muons can be used for the development and testing of track reconstruction algorithms.

The development and testing of the track reconstruction algorithm discussed in Ch. 4 is based on simulated single muons using MuonGun Floodlight mode. Muons were injected starting from a cylindrical surface with a 60 m margin surrounding the detector volume. We generated 500,000 single muons with energies from 100 GeV to 1 PeV following  $E_{\mu}^{-1}$  power-law spectrum across all zenith angles.

### 3.3 Lepton Propagation

When a neutrino interacts near the detector volume of a neutrino telescope, it produces secondary particles. Among these, the charged leptons generated as products of neutrino interactions are of particular interest, as they propagate through the detector medium and are responsible for Cherenkov radiation.

Initially, the IceCube experiment utilized the Muon Monte Carlo (MMC) [41] program for muons and other charged lepton propagation. The Propagator with Optimal Precision

and Optimized Speed for All Leptons (PROPOSAL) [87,88] was developed as a significant update and replacement for MMC, offering improved accuracy and performance.

The most recent updates to PROPOSAL [88] include the implementation of state-of-theart cross-section parametrizations for key processes, such as ionization, bremsstrahlung, photonuclear interactions, electron pair production, as well as the Landau-Pomeranchuk-Migdal and Ter-Mikaelian effects. Additionally, the treatment of muon and tau decays has been refined, and Molière scattering is now implemented with multiple parametrization options to enhance the accuracy of angular deflection modeling.

The PROPOSAL we used in our simulation is implemented in the IceCube icetray software, written in C++, and provides a Python interface that we utilized throughout the entire simulation workflow.

# 1086 3.4 Photon Propagation

The photon propagation step of the simulation involves the propagation of Cherenkov photons generated from simulated secondary particles produced by neutrino interactions. Understanding the optical properties of the detector medium is crucial for accurately modeling
the propagation of photons through neutrino detectors. These optical properties include the
speed of light in that medium, the scattering, and the absorption of Cherenkov photons.
More details about photon propagation can be found in Ref. [89, 90].

Historically, people built interpolated look-up tables of expected photoelectron timing
distributions at a digital optical module for all possible configurations of the light source
and receiver. Photonics [89] were utilized for photon propagation with look-up tables interpolated using splines. Then, these lookup tables were used during the simulation to sample

the number of photons at given arrival times.

Methods that use direct photon propagation during the simulation process were developed as discussed in Refs. [91–93]. These methods are based on tracking each single photon. While direct photon propagation improves accuracy and addresses other drawbacks associated with using look-up tables, tracking individual photons is computationally expensive. This process is accelerated using parallel computation on graphics processing units (GPUs) and high-performance computing machines [93].

For the photon propagation simulation step in our work, we utilized the CLsim [93] from
the IceTray software framework. For this work, CLsim was configured <sup>1</sup> with seawater optical
properties based on the measurements by the STRAW pathfinder mission (see Sec. 2.3).

### 3.5 Detector Electronic Simulation

Simulation of the response of Digital Optical Modules (DOMs) involves simulating the re-1108 sponse of the photomultiplier tube (PMT) and the optical module mainboard electronics in 1100 response to the detected photoelectrons [94]. For neutrino detectors operating in ocean wa-1110 ter or sea-water the detector response simulation must also account for environmental back-1111 ground noise <sup>2</sup>. Two important sources of this background noise in deep-sea water are biolu-1112 minescence and radioactive decay from potassium-40 (<sup>40</sup>K) [11,95]. Dissolved potassium-40 1113 in seawater undergoes beta decay, producing photons that contribute a predictable back-1114 ground rate. Bioluminescence arises from marine organisms, and contributes background 1115

<sup>&</sup>lt;sup>1</sup>As stated in Ref. [44], Jakub Stacho implemented this configuration in our simulation chain using linear interpolation between the four measured attenuation lengths at distinct wavelengths. Scattering was represented by a mix of Rayleigh and Petzold scattering functions for ocean waters, following parameters previously used in ANTARES.

<sup>&</sup>lt;sup>2</sup>Background noise here does not refer to voltage fluctuations in the electronics, but rather to real photoelectrons arising from sources other than high-energy secondary particles produced by neutrinos or cosmic rays.

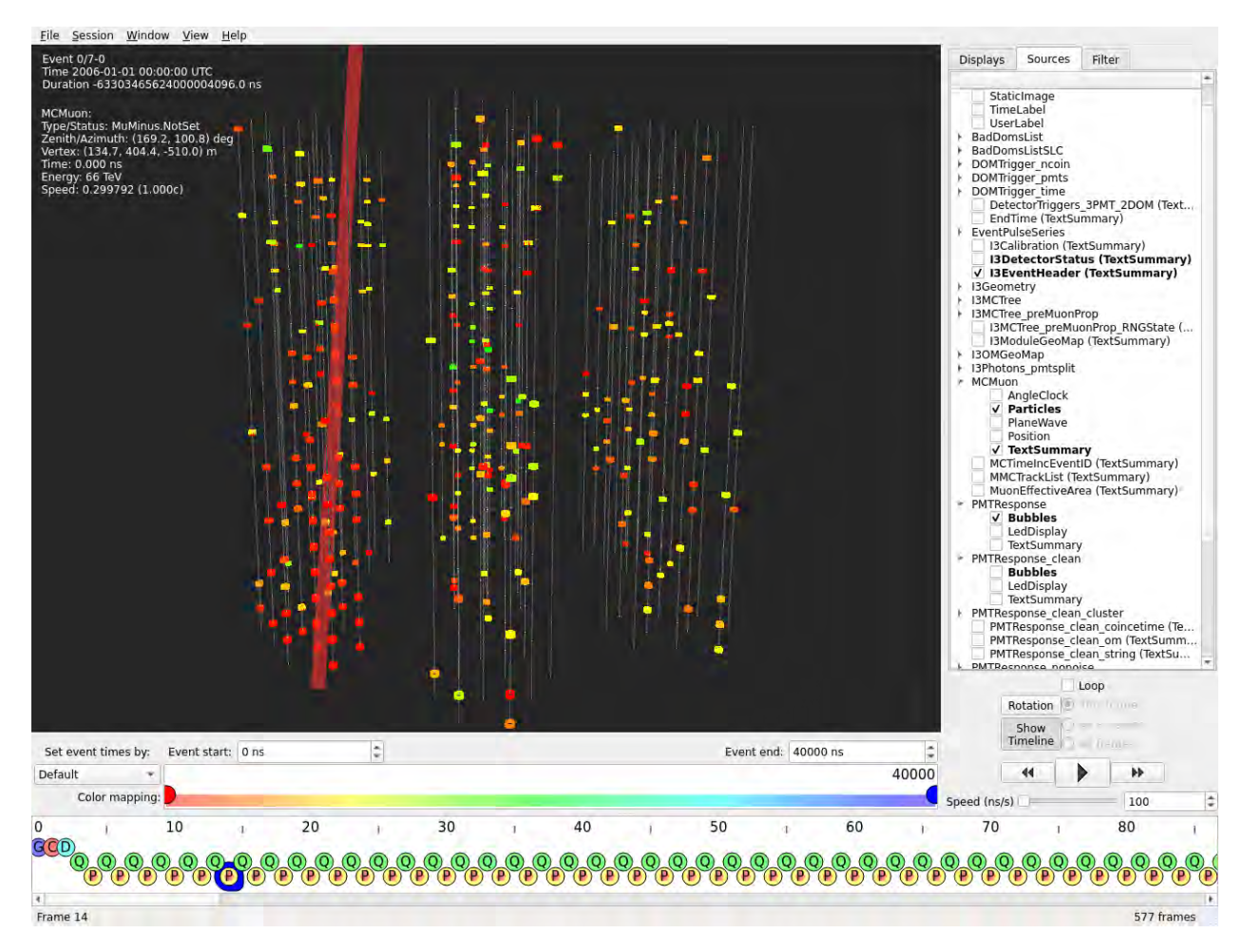


Figure 3.3: An example of a simulated high-energy muon with uncleaned pulses. Credit Nathan Whitehorn.

noise rates that are variable and often much higher than those from  ${}^{40}K$  [11, 12, 67, 68].

The Monte Carlo simulation employed in this study uses simplified models of detector response, background noise, and detector trigger. Currently, the software code PONEDOMLauncher<sup>3</sup>, used to simulate the detector response, is implemented in Python using the Icetray software framework and its data structures. At the time of writing, the optical modules are still in development. Many aspects of the detector response simulation are currently under study and undergoing continuous improvement, in part by incorporating more data from lab

 $<sup>^3</sup>$ This code is written by Tomas MCElroy, who at the time was a postdoc at the University of Victoria, and refactored by Claudio Kopper

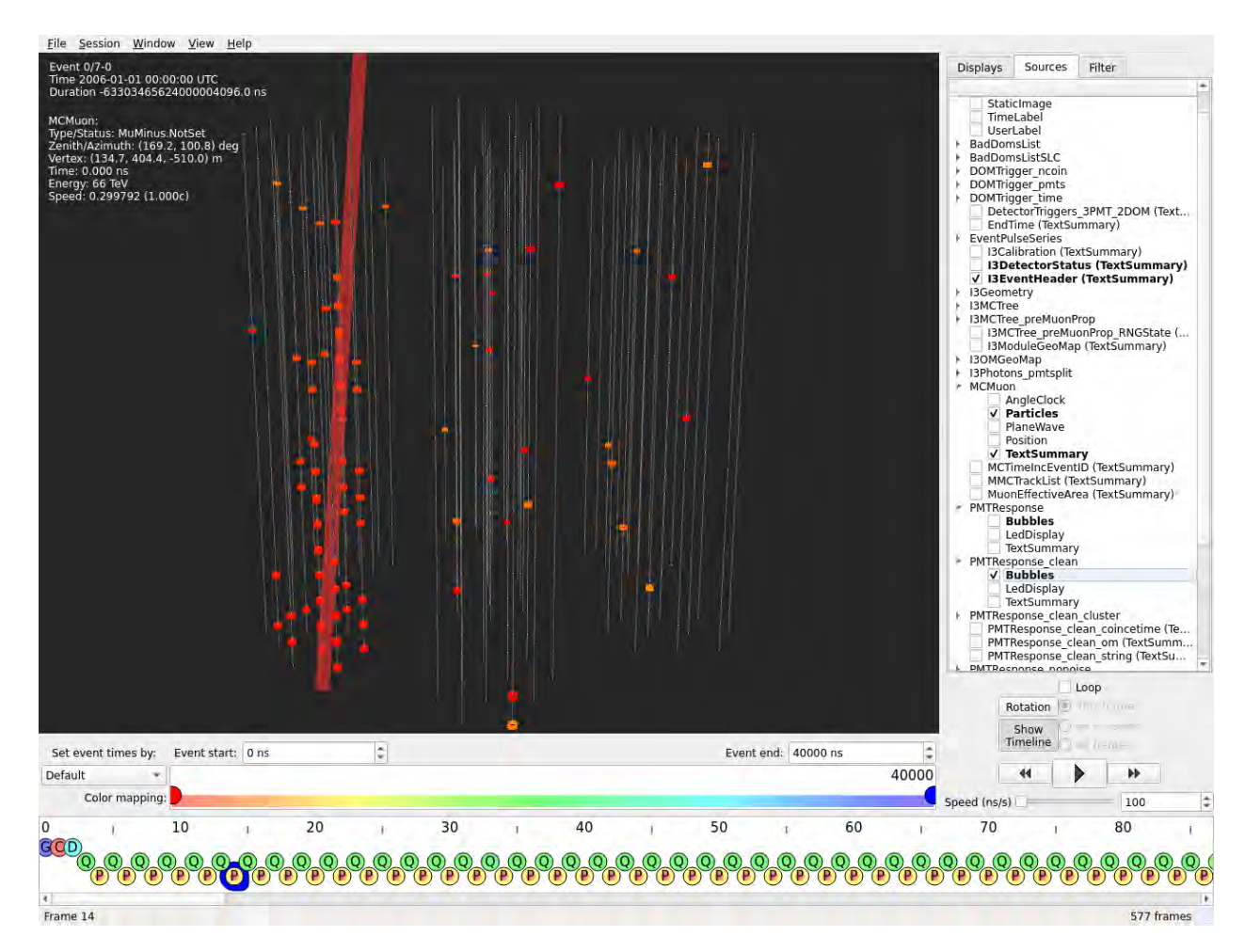


Figure 3.4: An example of a simulated high-energy muon with cleaned pulses. Credit Nathan Whitehorn.

#### measurements. 1123

1127

1129

1131

For our simulation, a simple DOM simulator uses the output from a detailed event 1124 simulation using CLsim as illustrated in Fig.3.1. To add a simple electronic model, for 1125 each photoelectron time, we add a time offset sampled from a normal distribution based on 1126 the PMT transit time spread of around 1.3 ns, as measured in the lab. For each pulse, there is a chance of generating an afterpulse, and a characteristic time delay of  $2 \mu s$  is simulated. 1128 We add dark noise by sampling the time of occurrence from an exponential distribution. The time differences here are sampled from an exponential distribution, as this corresponds to a 1130 Poisson process of independent events with a constant rate of 10 kHz per optical Module.

The actual P-ONE trigger algorithms are also being designed and developed at the time of writing. Two trigger levels are planned. This consists of the local coincidence within each module and an overall detector trigger. For this study, we have used a basic placeholder P-ONE detector trigger simulation. The optical module local coincidence requires at least 3 PMTs within a 10 ns time window for a single DOM. The simulation require that at least one module pass the local coincidence criterion for the event to be considered further.

# 3.6 Summary

We have adapted tools developed by the IceCube Neutrino observatory collaboration to pro-1130 duce event simulations for the Pacific Ocean Neutrino Experiment. The current simulation 1140 utilizes a test geometry, and an ongoing effort is underway to produce an optimal geometry 1141 design. We have developed a basic model for detector electronic simulation for this first 1142 detailed Monte Carlo simulation. This simulation pipeline needs improvement of the back-1143 ground noise simulation, in addition to the signal from the physics event simulation. This 1144 involves including results on the bioluminescence noise studies and on background noise from 1145 potassium-40 results conducted by a collaborator and improving simulation of background 1146 noise from Potassium-40. Another aspect of the event simulation work that needs improve-1147 ment is the detector response model simulation using lab data, which the collaboration is working on. Nevertheless, this initial version of the Monte Carlo is sufficient for us to esti-1140 mate the expected angular resolution of P-ONE and its sensitivity to astrophysical neutrino 1150 sources. 1151

# Chapter 4

# 53 Track Event Reconstruction

The ability of a neutrino telescope to discover astrophysical sources of high-energy neutrinos 1154 depends significantly on its angular resolution. A good reconstruction of event direction is 1155 needed to trace the origin of high-energy cosmic rays that produce these high-energy astro-1156 physical neutrinos. This chapter describes a track event reconstruction algorithm developed 1157 for the P-ONE using a Monte Carlo simulation. Sec. 4.1 describes a likelihood function that 1158 models the arrival time of Cherenkov photons recorded by photomultiplier sensors. Sec. 4.2 1159 discusses parameterization of the Cherenkov photon arrival time distribution. Sec. 4.3 dis-1160 cusses a reconstruction method to address the minimizer convergence in the narrow likelihood 1161 space near the solutions. In Sec. 4.4, we discuss the performance of this reconstruction al-1162 gorithm. We tested the performance using a Monte Carlo simulation of muon track events 1163 generated using the MuonGun event generator, following the simulation chain discussed in 1164 detail in Ch. 3. This is a preliminary event reconstruction method, which is unavoidable in 1165 any case, since a final algorithm will need to be tuned for factors such as noise rates and 1166 variability in optical properties, which can only be measured in situ once real detector strings 1167 are in place. This chapter is adapted from the work presented in the proceedings in Ref. [17]. 1168

#### 4.1 Likelihood Function

1169

Following standard maximum likelihood reconstruction techniques used by AMANDA [19] 1170 and later refined by IceCube [96], we have developed a likelihood-based reconstruction algo-1171 rithm to determine the trajectory of a muon passing through the P-ONE detector. PMTs 1172 in optical modules record the hit time information and the charge information. In Ref. [96], 1173 the IceCube collaboration used unbinned likelihood approaches to model the arrival times of 1174 photons for track direction reconstruction. The track geometry is encoded in the time part 1175 of the likelihood, while the amplitude term encodes the muon energy. The amplitude term 1176 is dependent on the stochastic muon energy losses, and one needs to know the muon energy 1177 to model it in a robust way [96]. Our current reconstruction ignores the amplitude term, as 1178 the time likelihood is the most important for track direction reconstruction. 1170

For each P-OM i that recorded light during the event, the data  $\mathbf{t}_i = \{t_{ij}\}$  consists of the time stamps  $t_{ij}$  of the corresponding light pulses j recorded by the P-OM. The trajectory  $\mathbf{x}(t)$ , the position of the muon as a function of time, is parameterized using five parameters: the location  $\mathbf{r_0} = (x_0, y_0, z_0)$  of the muon at some arbitrary time  $t_0$ , and the direction of the track  $\mathbf{p} = (\theta, \phi)$ . The zenith angle  $\theta$  and the azimuthal angle  $\phi$  mark the origin of the muon in the sky and are the parameters of interest of our reconstruction algorithm.

For a given track hypothesis  $\Theta=(r_0,p)$  and any pulse timestamp  $t_{ij}$ , we calculate the residual time for pulse j at P-OM i as

$$t_{ij}^{res} = t_{ij} - t_i^{geo}(\mathbf{\Theta}) \tag{4.1}$$

where  $t_{ij}$  is the hit time observed taking into account the scattering in the detector medium and  $t_i^{geo}$  is the hit time that would be observed if there were no scattering, given by the

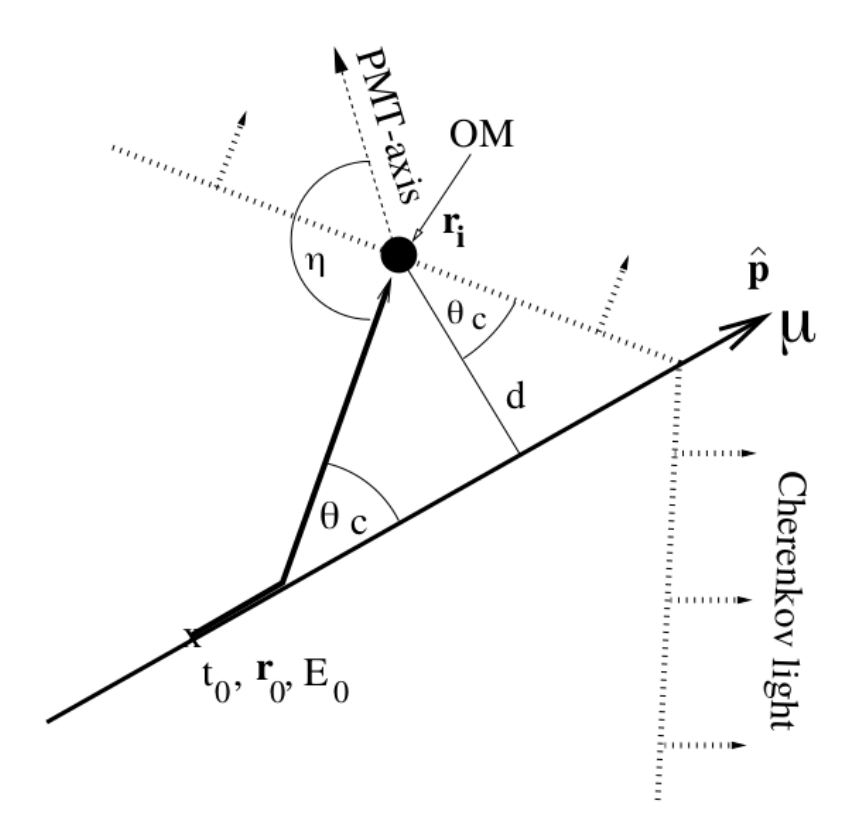


Figure 4.1: Parameters defining Cherenkov light of a muon near an Optical Module. Figure taken from Ref. [19]).

geometric formulae Eq. (4.2) from Ref. [19]. The geometric time is defined based on the geometry in Fig. 4.1 and is given by the equation below<sup>1</sup>.

$$t_i^{geo} = t_0 + \frac{\hat{\boldsymbol{p}} \cdot (\boldsymbol{r_i} - \boldsymbol{r_o}) + d \tan(\theta_c)}{c_{\text{vac}}},$$
(4.2)

where  $c_{\text{vac}}$  is the speed of light in vacuum.

At each P-OM, the distribution of residual times can be described using a two-component mixture model. It consists of a uniform probability density function,  $f_b(t^{res})$ , that accounts for detector noise hits. It also includes a photon arrival time probability density function,  $f_s(t^{res} \mid \Theta)$ , which characterizes the propagation of a photon from the track  $\Theta$  to the receiv-

 $<sup>^{1}\</sup>mathrm{A}$  derivation of this formula is shown in Refs. [21,97]

ing P-OM through water.

1198

The full likelihood function reads

$$\log \mathcal{L}\left(\boldsymbol{\Theta} \mid \boldsymbol{t^{res}}\right) = \sum_{i} \left\{ \sum_{j} \log \left[ p_{i}^{s} f_{s} \left( t_{ij}^{res} \mid \boldsymbol{\Theta} \right) + p_{i}^{b} f_{b} \left( t_{ij}^{res} \right) \right] \right\}$$
(4.3)

The probabilities of the mixture

$$p_i^s = 1 - p_i^b = 1 - \frac{q_b}{q_i^{tot}} \tag{4.4}$$

are easily determined from the expected noise  $q_b$  and the total measured charge  $q_i^{tot}$  in the OM i. The best-fit parameters  $\hat{\Theta}$  correspond to the global maximum of Eq. (4.3).

## 2 4.2 Photon Arrival Time Parametrization

The performance of maximum likelihood methods is dependent on the precision of the as-1203 sumed likelihood model function. This likelihood function depends on the accurate parametriza-1204 tion of the photon arrival time residual probability density function. Here, we derive the residual time pdfs  $f(t^{res} \mid \Theta)$  from large-scale simulations of muons with varying energies 1206 and random directions through the P-ONE detector using the simulation chain described in 1207 Ch. 3. Specifically, we simulated muons isotropically in all directions within the cylindrical 1208 volume defined by simulated detector geometry. Muons<sup>2</sup> are generated starting from a fidu-1209 cial cylindrical surface surrounding the instrumented simulated volume. To define this we use geometry margin extended 60 m beyond the outer boundaries of the simulated detector 1211 volume. For each muon, we tabulate the residual times of the photon pulses  $t_{ij}^{res}$  as a func-1212

<sup>&</sup>lt;sup>2</sup>We used MuonGun in its Floodlight mode. This generates single muons in detector volume.

tion of the distance of closest approach of the muon to the DOM  $d_i(\Theta)$  that a photon would travel between its emission point on the track and the receiving P-OM i. The expected hit time of a pulse,  $t_i^{geo}$ , is computed according to Eq. (4.2) using the implementation <sup>3</sup> from IceTray, and taking into account the optical properties of the Cascadia Basin.

#### 4.2.1 Mixture Model PDF

1217

1222

Previous efforts in reconstruction for neutrino telescopes using likelihood methods have explored analytical parametrization of Cherenkov photon time residuals. In Ref. [19], the
AMANDA collaboration investigated the parametrization of the time residual PDF using the
Pandel distribution function. The Pandel probability density function is given by Eq. 4.5.

$$pdf\left(t^{res} \mid d\right) = \frac{1}{N(d)} \frac{\tau^{-d/\lambda} \cdot t_{res}^{(d/\lambda - 1)}}{\Gamma(d/\lambda)} \cdot e^{-\left(t_{res} \cdot \left(\frac{1}{\tau} + \frac{c_{\text{medium}}}{\lambda_a}\right)\right)}$$
(4.5)

$$N(d) = e^{-d/\lambda_a} \cdot \left(1 + \frac{\tau \cdot c_{\text{medium}}}{\lambda_a}\right)^{-d/\lambda}$$
(4.6)

Where  $\lambda_a$  is the absorption length,  $\Gamma(d/\lambda)$  is the Gamma function. N(d) is the normalization factor given by Eq. (4.6). The free parameters  $\lambda$ ,  $\tau$  are functions of the photon distance d and other geometrical parameters [19].

The Pandel PDF has zero probability for a negative time residual. In reality, negative time residuals occur due to both transit time jitter in the detector PMT and random dark noise recorded by the PMT. To cope with negative time residuals, Ref. [20] studied an approximation of the convoluted Pandel function, which incorporates detector effects through convolution with a Gaussian error model. In Ref. [99], the approximated CPandel

<sup>&</sup>lt;sup>3</sup>we used I3Calculator utility module of the phys-services project from the IceTray software framework by the IceCube collaboration [98]

parametrization is used for track reconstruction in P-ONE.

We first describe an effort to parametrize the time residual using a mixture model prob-1232 ability density function given by Eq. (4.7), motivated by Ref. [100]. The mixture model PDF is composed of three skewed normal probability density functions Eq. (4.8), a gamma 1234 PDF (4.9), and a uniform PDF. Each skewed gamma component has three parameters and 1235 a relative normalization factor. Each parameter  $\mu_j(d)$ ,  $\sigma_j(d)$ ,  $r_j(d)$ , and  $\theta(d)$  is a function of 1236 the distance of closest approach of the muon to the DOM. The gamma distribution is also a 1237 function of two parameters and a normalization factor. Each function is given a correspond-1238 ing weight that is a function of the distance to the secondary particle that emits Cherenkov 1239 photons. In this study, the uniform PDF models the effect of random noise. The asymmetric 1240 normal distribution functions model the impact of PMT jitter and scattered photons. The 1241 gamma PDF fits the tail of heavily scattered photons and photons from very far track hits. 1242 The fitted PDF components of the mixture model PDF are shown in Figs. 4.2, 4.3, and 4.4 1243 for the closest distances of 10 m, 30 m, and 100 m, respectively. 1244

$$pdf(t^{res} \mid d) = \sum_{j}^{3} w_{aj} \cdot \text{AG}\left[t^{res} \mid \mu_{j}(d), \ \sigma_{j}(d), \ r_{j}(d)\right] + w_{g} \cdot \text{Gamma}\left(t^{res} \mid k, \ \theta(d)\right) + w_{u} \cdot \text{Unif.}$$

$$(4.7)$$

The Asymmetric Gaussian functions AG in Eq. 4.7 are defined by the following Eq. 4.8.

$$\operatorname{AG}(x \mid \mu, \sigma, r) = \frac{2}{\sqrt{2\pi} \cdot \sigma(r+1)} \cdot \begin{cases} \exp\left(-\frac{1}{2} \left(\frac{x-\mu}{\sigma}\right)^{2}\right), & x < \mu \\ \exp\left(-\frac{1}{2} \left(\frac{x-\mu}{\sigma r}\right)^{2}\right), & x \ge \mu \end{cases}$$
(4.8)

The Gamma distribution is defined by

1245

1246

$$f(x \mid (k, \theta)) = \frac{1}{\Gamma(k)\theta^k} \cdot x^{k-1} e^{-\frac{x}{\theta}}$$
(4.9)

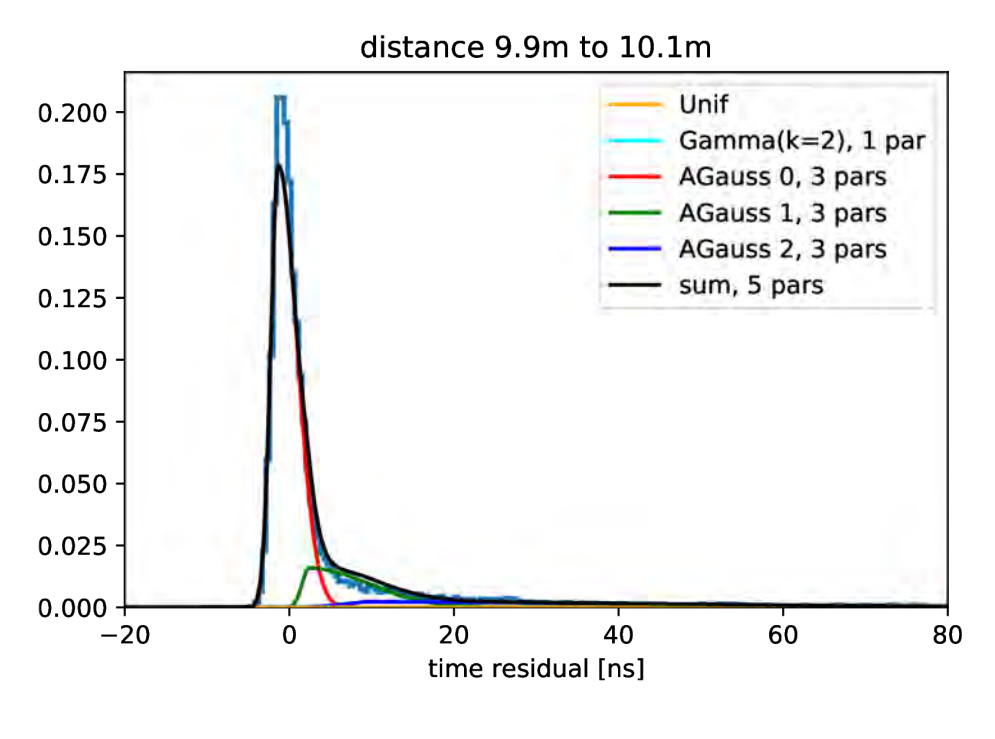
Here,  $\theta(d)$  is the scale parameter and is a function of the effective distance. k is the shape parameter. In our case, we use k=2.0.

At each given distance of closest approach d, we fit these 15 model parameters to match 1249 the model PDF to the time residual PDF from the simulation, looking at the time resid-1250 ual distributions within  $20\,\mathrm{cm}$  slices. We use a TensorFlow-based fitting tool  $^4$  leveraging 1251 gradients using GPUs on computing clusters. For each distance, we fit the mixture model 1252 with 15 parameters, and the dependence of the fitted parameters on distance was then es-1253 tablished using a parametrization with third-degree polynomials. The plots in Figs. 4.2, 4.3, 1254 and 4.4 show histograms of the residual time PDF from the Monte Carlo simulation for 20 1255 cm slices around effective distances of 10 m, 30 m, and 100 m. The figure also compares the MC time residual with the pdf parameterization using the new mixture model. Using the 1257 time residuals distribution from our Monte Carlo simulation, the PDF parametrization using 1258 this mixture model showed an improvement over the CPandel parametrization as shown in 1259 Fig. 4.5. 1260

## 1261 4.2.2 Photosplines PDF

The analytical parametrization of the photon's arrival time residuals using the mixture model PDF presents an improvement over the CPandel PDF as shown by the plots in Fig. 4.5. However, the method needs refinement in fitting model parameters, especially for time residuals

<sup>&</sup>lt;sup>4</sup>The tool uses the maximum likelihood method to fit a mixture model to the MC data samples utilizing TensorFlow for automatic differentiation and gradient-based optimization (L-BFGS algorithm). Hans Niederhausen wrote the core algorithm. I adapted the code to do the fitting and established a parametrization of the mmpdf model fitted parameters as a function of distance d.



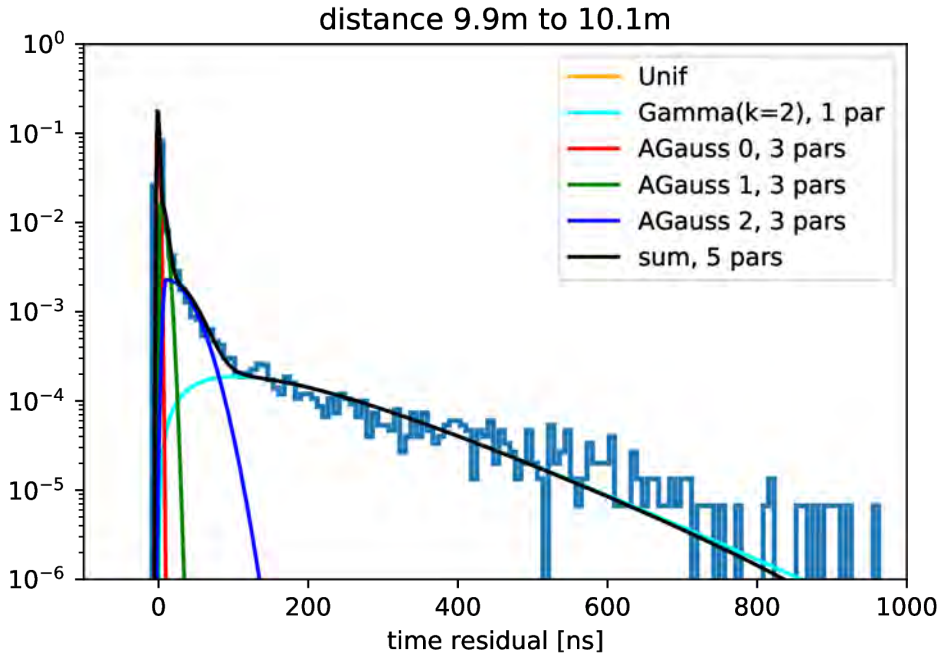
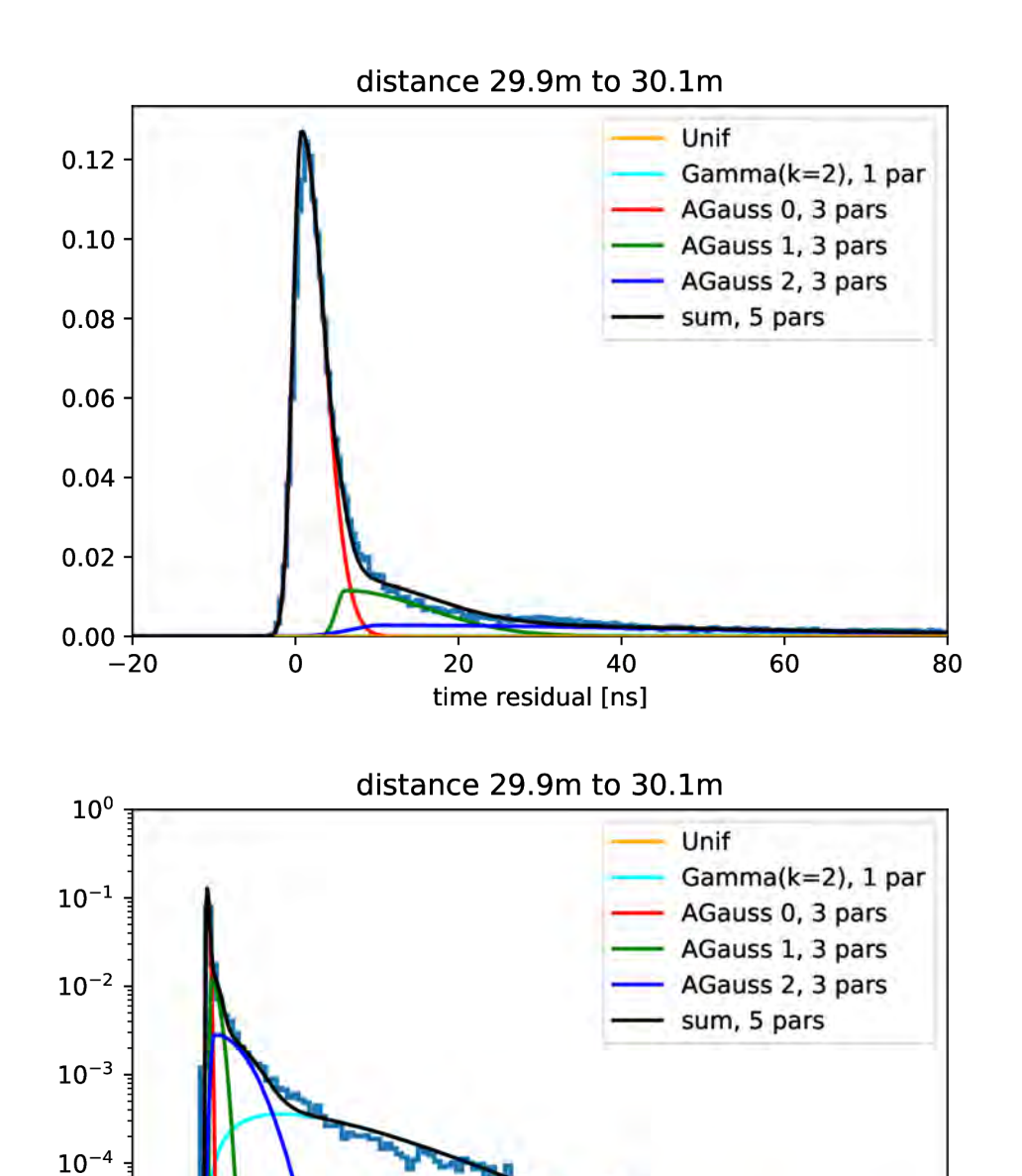
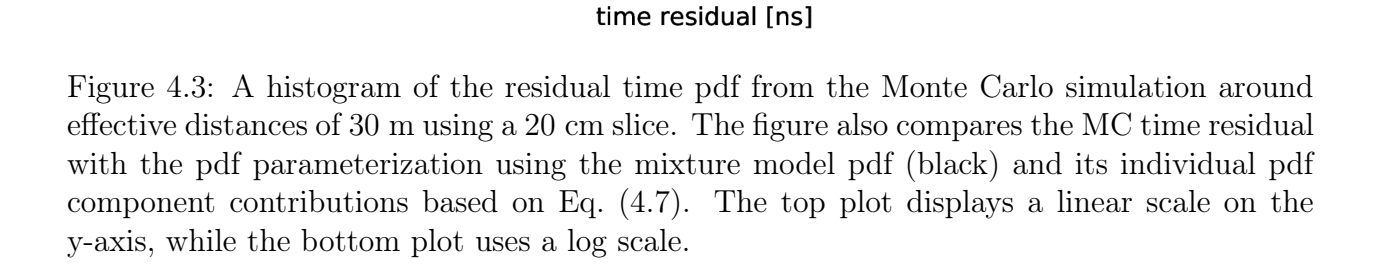


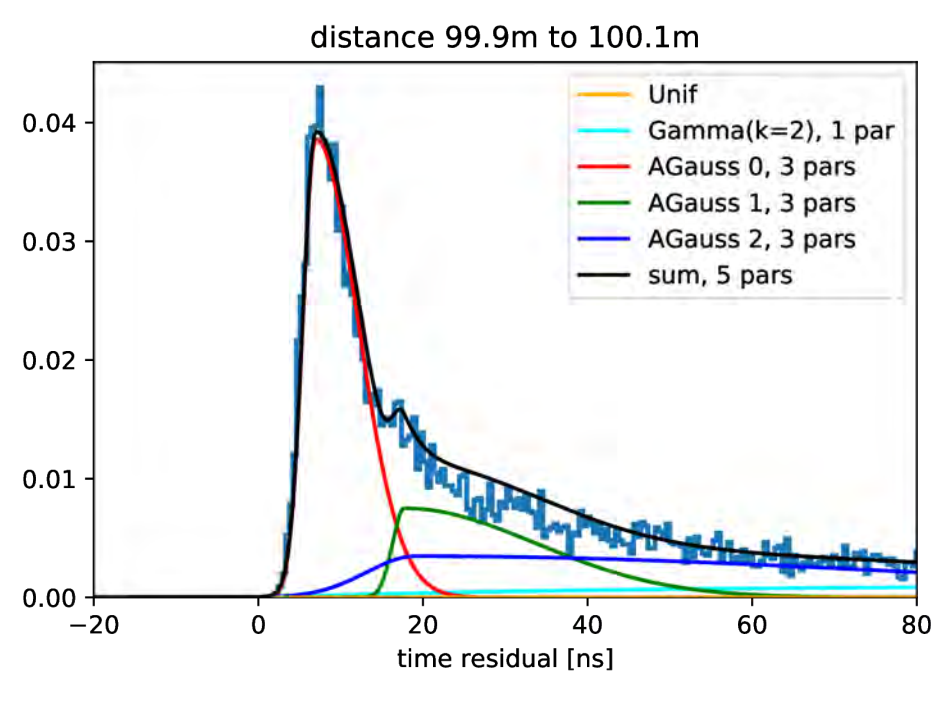
Figure 4.2: A histogram of the residual time pdf from the Monte Carlo simulation around effective distances of 10 m using a 20 cm slice. The figure also compares the MC time residual with the pdf parameterization using the mixture model pdf (black) and its individual pdf component contributions based on Eq. (4.7). The top plot displays a linear scale on the y-axis, while the bottom plot uses a log scale.





 $10^{-5}$ 

 $10^{-6}$ 



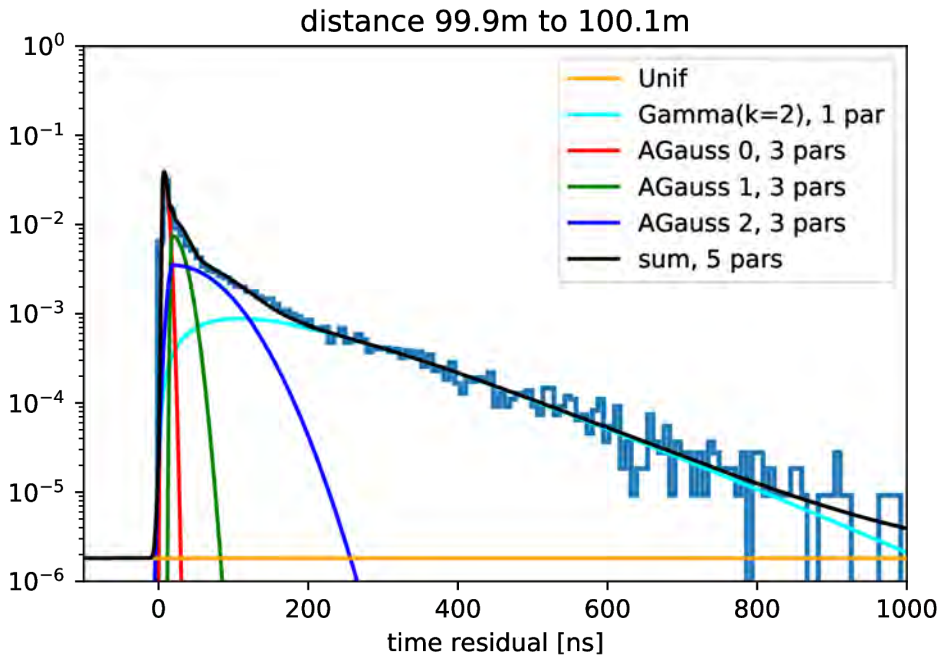


Figure 4.4: Histograms of the residual time pdf from the Monte Carlo simulation around effective distances of 100 m using a 20 cm slice. The figure also compares the MC time residual with the pdf parameterization using the mixture model pdf (black) and its individual pdf component contributions based on Eq. (4.7). The top plot displays a linear scale on the y-axis, while the bottom plot uses a log scale.

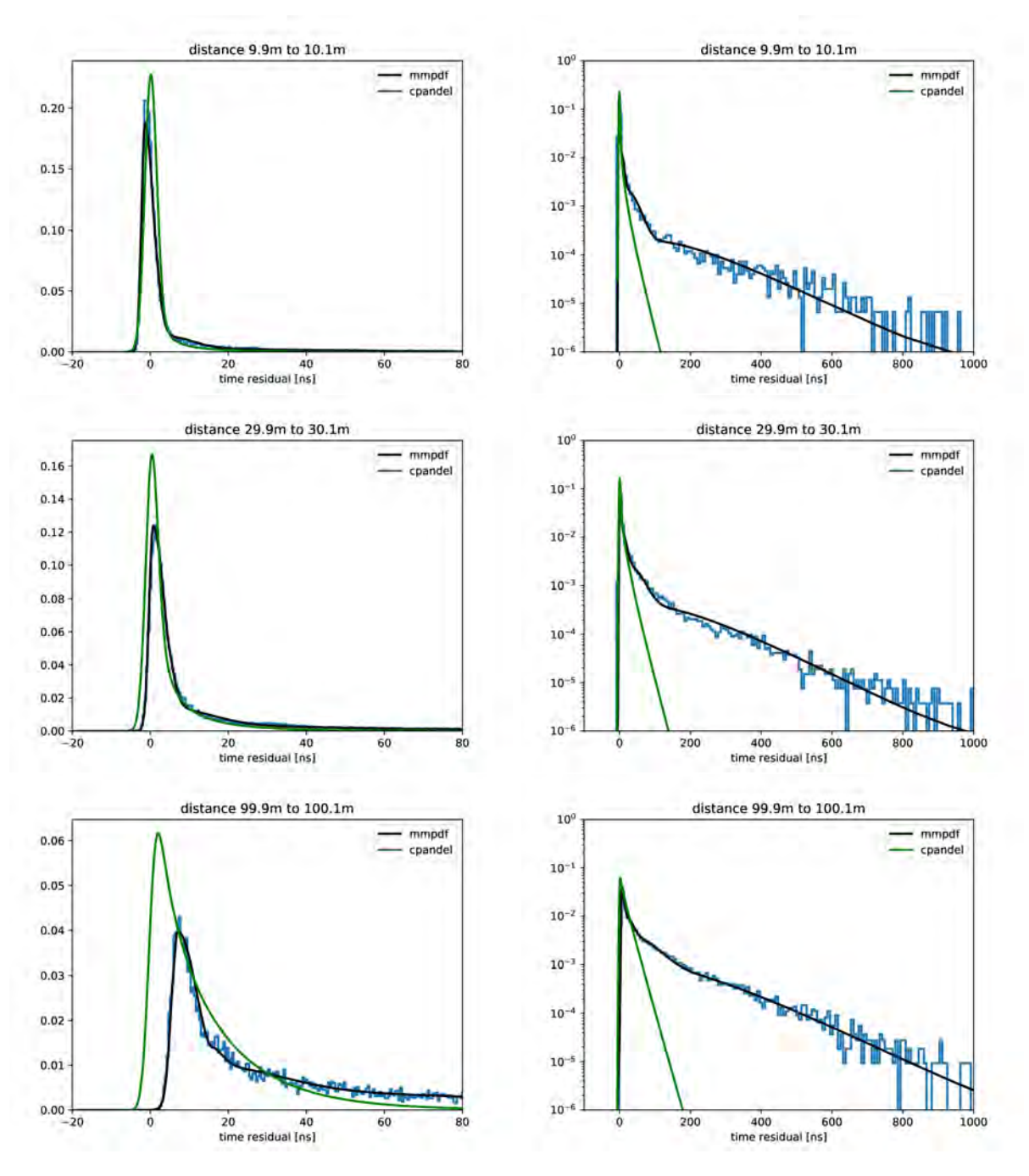


Figure 4.5: Comparison of CPandel vs mixture model PDF (mmpdf) parametrization of the MC simulation time residual histograms for DOM distance around 10 m (top plots), 30 m (middle plots), and 100 m (bottom plots) using 20 cm slices. The right plots display a linear scale on the y-axis, while the bottom plots use a log scale on the y-axis. The results for the CPandel PDF [20] implemented in IceCube IceTray software framework as discussed in Ref. [21]. Here we used the following free parameters: tau scale of  $\tau = 20$  ns, an absorption length  $\lambda_a = 25$  m, and a scattering length  $\lambda = 120$  m. The plots are for timing uncertainty of the PMT of  $\sigma = 1.5$  ns.

at shorter distances between the track and the hit DOM. Hits that are too close to the track introduce numerical instability within the likelihood space, as shown, for example, in the likelihood profile scan in the top right plot of Fig. 4.11, which complicates the numerical minimization of likelihood functions. As an interim solution, we alternatively fit the time residuals using nonparametric spline techniques [101].

To construct the splines, we approximate  $f_s(t^{res} | \Theta) \approx f_s(t^{res} | d(\Theta))$  and construct the function numerically by interpolating the corresponding 2D histogram using a nonparametric B-spline interpolation technique [101]. An example is shown in Figs. 4.6 and
4.8 demonstrating that the B-spline representation of  $f_s(t^{res} | d(\Theta))$  evaluated at d = 10 m
and at d = 100 m matches well with the simulated photon arrival times recorded at that distance.

## $_{\scriptscriptstyle{276}}$ 4.3 Reconstruction Implementation

A fast reconstruction, such as Line-Fit [19, 102], is used as an initial starting point for a more robust reconstruction, such as a maximum-likelihood reconstruction.

We implemented the likelihood function in Eq. 4.3 in C++ using modules and services
from the icetray software framework [98]. In particular, we use dataclasses, physics-services,
and gulliver <sup>5</sup> from IceCube icetray [98]. At the time of writing, the implementation code
for likelihood resides in the pone-software repository.

To make a Gulliver likelihood fit, we use I3SimpleFitter from Gulliver-modules that implement a simple fit. Fig. 4.9 shows the components (services) needed for the likelihood fitter. The event log-likelihood services, which evaluate likelihood for a set of parameters

<sup>&</sup>lt;sup>5</sup>Gulliver is a generic utility for log-likelihood function-based reconstruction algorithms. It provides base classes for event likelihood functions, minimization algorithms, parameterizations, and seeding services [103]

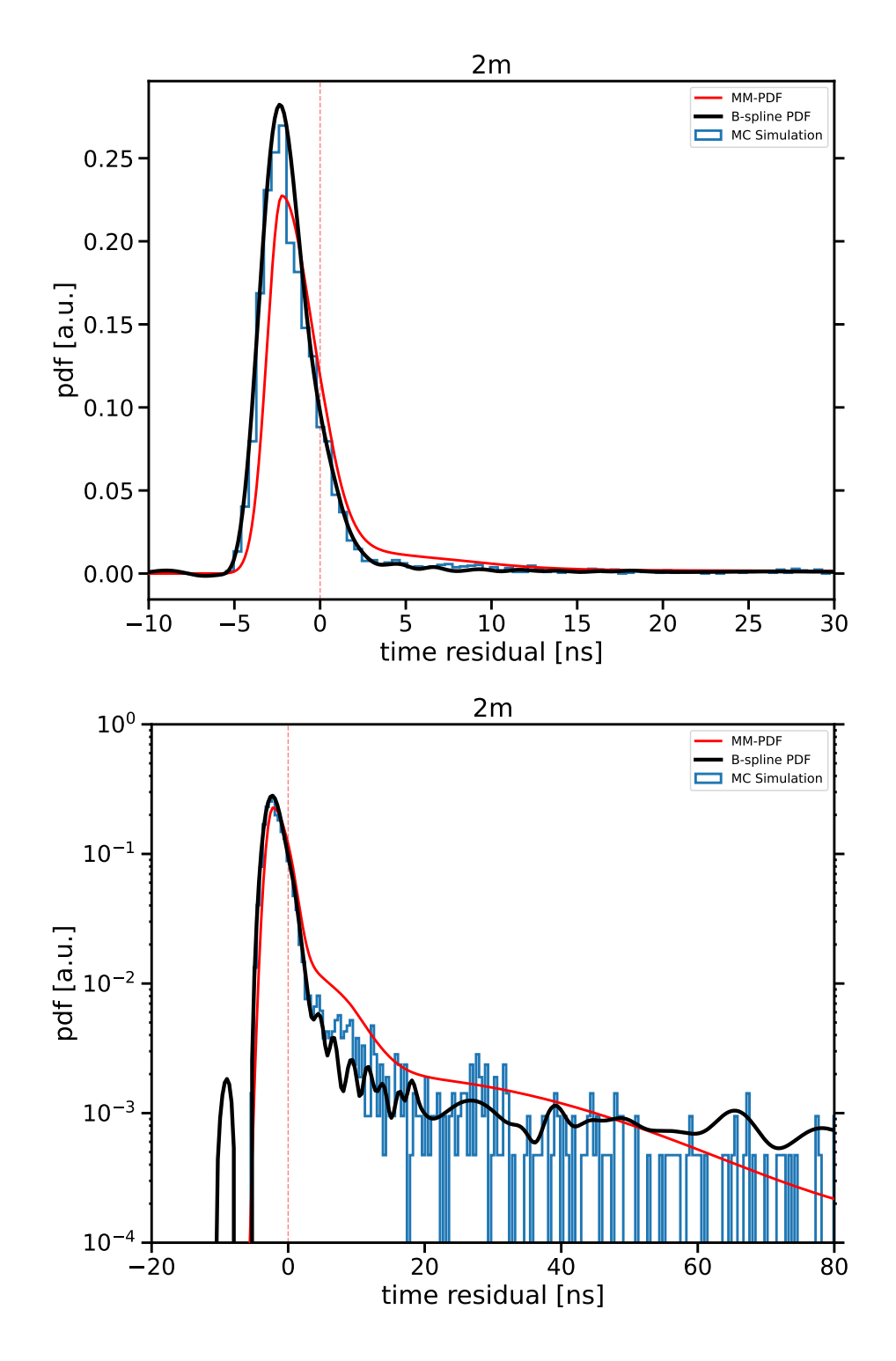


Figure 4.6: Histograms of the residual time pdf from the Monte Carlo simulation around effective distances of 2 m using a 20 cm slice. The figure also compares the MC time residual with the B-splines PDF (black) and the mixture model PDF (red). The top plot displays a linear scale on the y-axis, while the bottom plot uses a log scale.

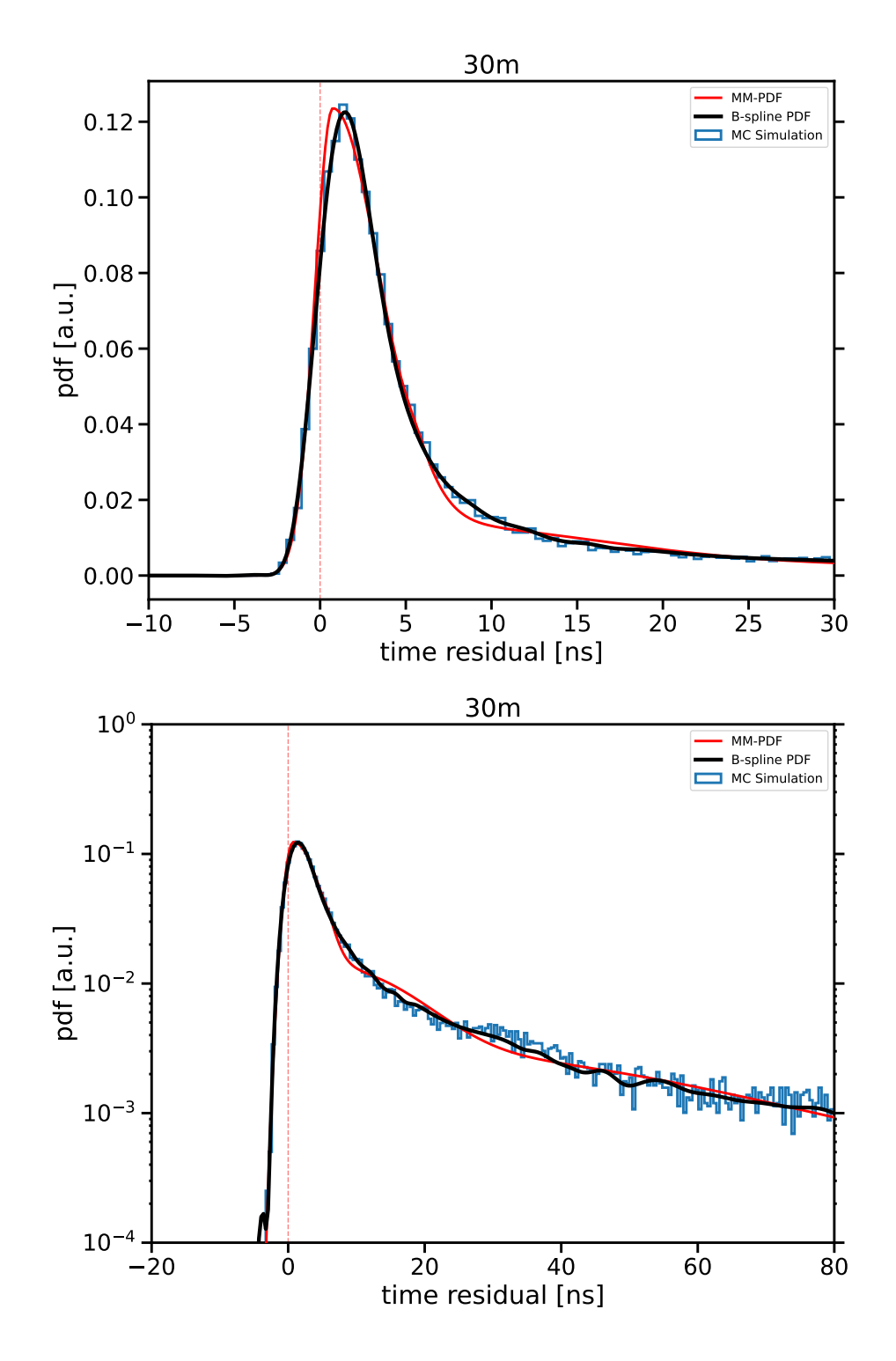


Figure 4.7: Histograms of the residual time pdf from the Monte Carlo simulation around effective distances of 30 m using a 20 cm slice. The figure also compares the MC time residual with the B-splines PDF (black) and Mixture Model PDF (red). The top plot displays a linear scale on the y-axis, while the bottom plot uses a log scale.

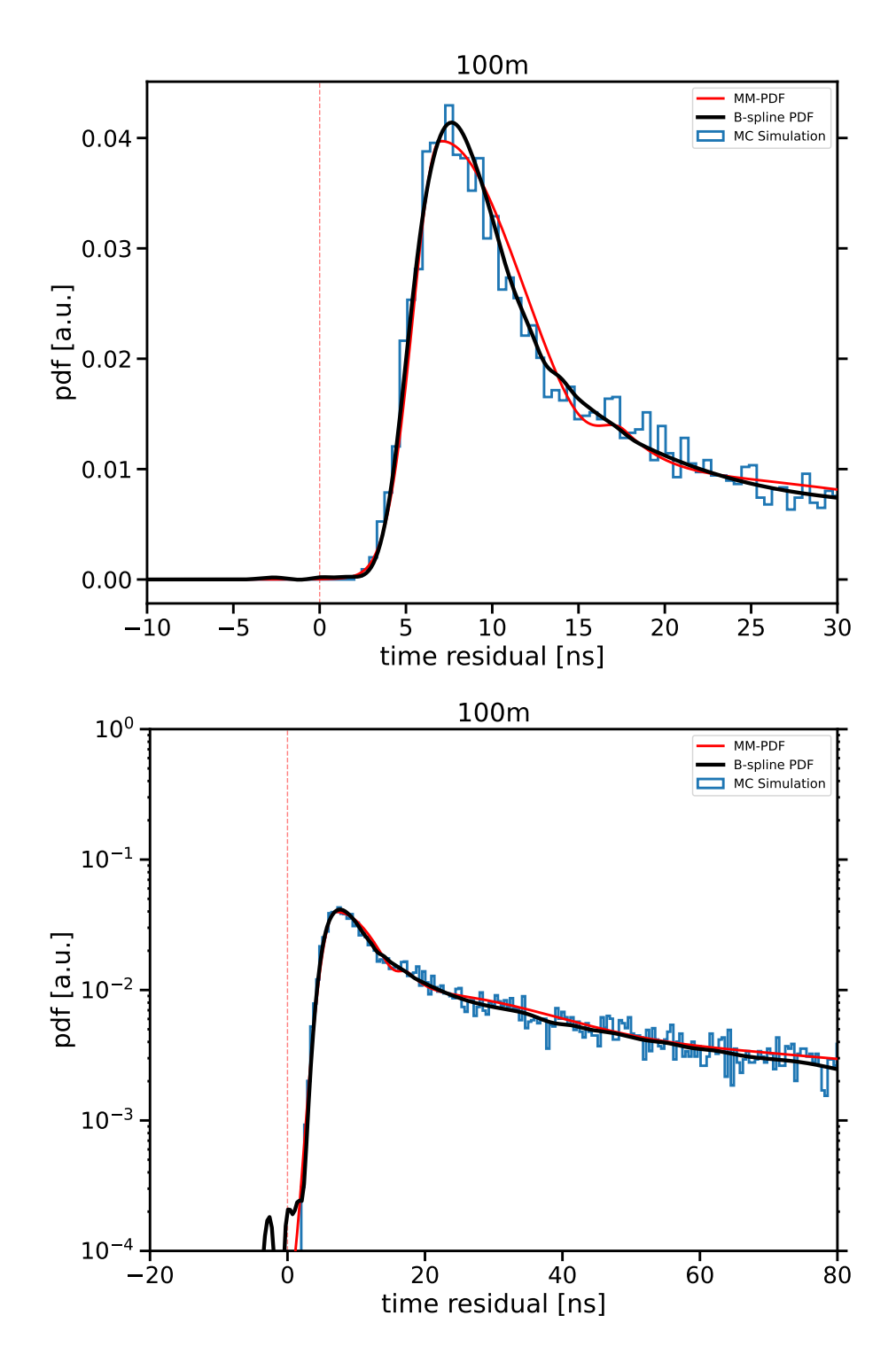


Figure 4.8: Histograms of the residual time pdf from the Monte Carlo simulation around effective distances of 100 m using a 20 cm slice. The figure also compares the MC time residual with the B-splines PDF (black) and the mixture model PDF (red). The top plot displays a linear scale on the y-axis, while the bottom plot uses a log scale.

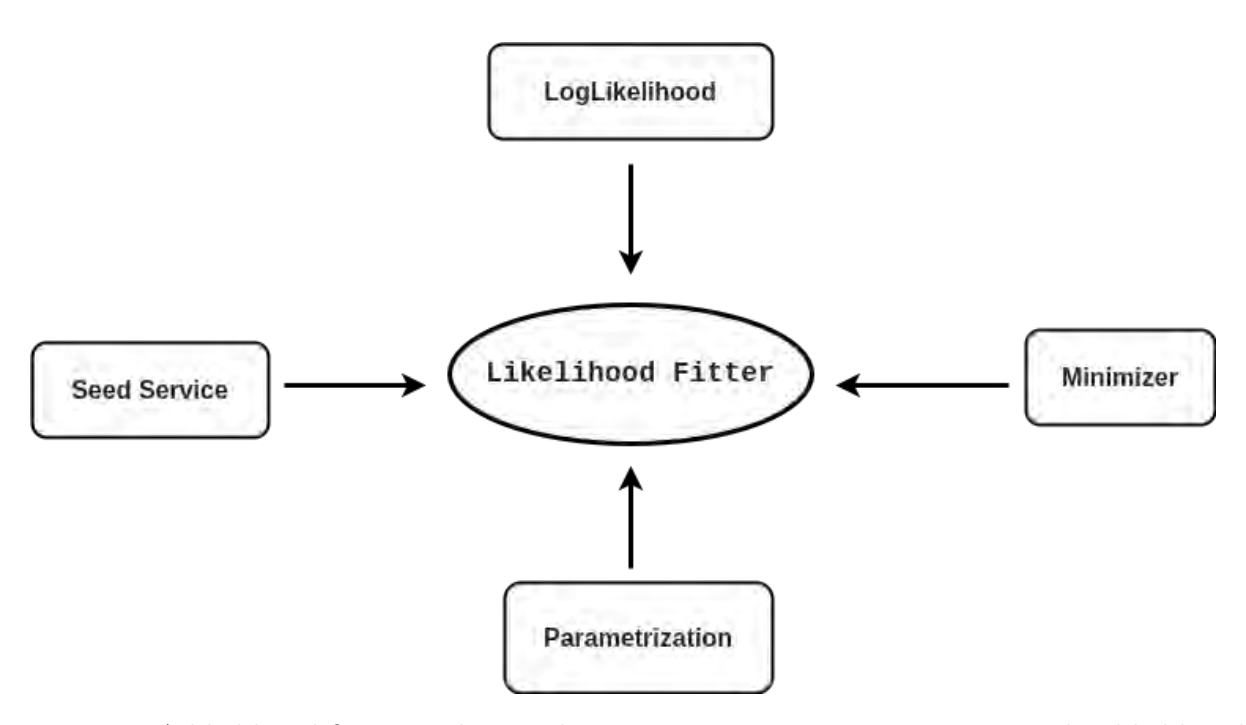


Figure 4.9: A likelihood fitter needs a seed service, a parametrization service, a log-likelihood service, and a minimizer service. Diagram adapted per Gulliver from IceTray documentation

of a given particle hypothesis, are implemented by inheriting I3EventLogLikelihoodBase
base class from the Gulliver. We used I3BasicSeedServiceFactory that handles the initial parameter guess (seed). The fitter uses the I3GLSimplexFactory minimizer service
to perform optimization of the likelihood fit, using the simplex [104] algorithm. We used
I3HalfSphereParametrizationFactory parametrization service to control how the track
parameters are adjusted during the fit, including step sizes and bounds for each parameter.

#### 4.3.1 Likelihood Scans

1292

We performed likelihood profile scans to verify whether the likelihood functions we constructed accurately describe the time residuals from the Monte Carlo simulation. For every given pair of azimuth and zenith angles in the grid, we fit for the event vertex with the direction held fixed, seeding with the Monte Carlo truth vertex and time information. This calculates the log-likelihood value for each event hypothesis at every direction point in the grid. The simple fitter utilizes seeding, parameterization, minimizer services, and a likelihood function, as described in Sec. 4.3.

If the likelihood describes the Monte Carlo simulation well, the minimum from the grid 1300 scan should be very close to, but not precisely at, the optimum of the likelihood space due to 1301 statistical fluctuations in the data. For example, as shown in the profile likelihood scans in 1302 Figs. 4.10 and 4.11, the minimum from the grid scan is close to the direction of the simple fit 1303 in both cases. For these events, the opening angle between the Monte Carlo true direction 1304 and the simple fit reconstruction direction is less than 0.1 degrees. This suggests that for 1305 events that pass through multiple clusters in the detector volume, likelihood reconstruction 1306 can potentially achieve an angular resolution that is several times better than that of the in-ice IceCube. 1308

However, for some events, we found that using B-splines provided a smoother likelihood space and eliminated the numerical instability found using the mixture model PDF
parametrization, as shown in Fig. 4.11. The imperfection in determining the mixture model
PDF parametrization could be improved in future work. For example, instead of determining
the model parameters using a fitting procedure that employs a likelihood method, as discussed in Sec. 4.2.1, future work can utilize a neural network approach to provide a smoother
PDF.

#### 1316 4.3.2 Reconstruction Method

There is an improvement in the likelihood description of the time residual PDF using the
B-spline PDF compared to using the mixture model PDF parametrization, especially at very
small distances of closest approach (see Fig. 4.11 and Fig. 4.6). However, correctly identifying

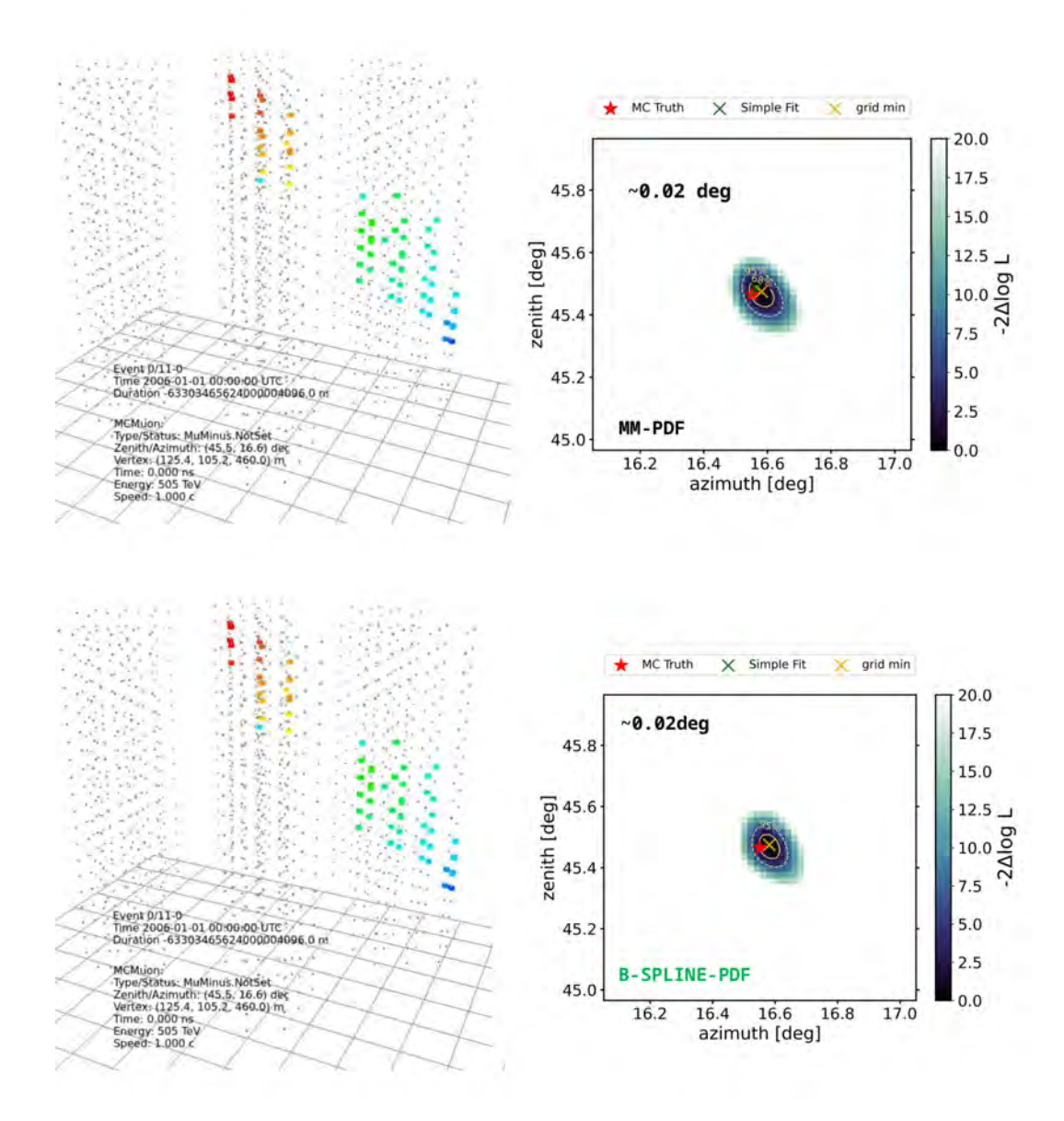


Figure 4.10: The left diagrams are visualizations of a simulated 505 TeV event as it passes through the detector volume in the event viewer. The color-coding indicates the arrival time of the photoelectrons, with red marking early arrivals and green marking late arrivals. The right-hand plots show the profile likelihood scans for the event shown in the left diagrams. The color bar is a test statistic,  $-2(\log \mathcal{L} - \min(\log \mathcal{L}))$ , indicating how much each log-likelihood deviates from the minimum. The green cross shows the direction found by a simple fitter seeded with the Monte Carlo truth for all parameters. The orange cross shows the direction of the minimum likelihood found during the grid scan. The top plots utilize a likelihood based on our mixture model PDF (see Eq. 4.7). The bottom-right plot uses the B-spline PDF parameterization instead of the mixture model shown in Fig. 4.2.2. Figure courtesy of H. Niederhausen.

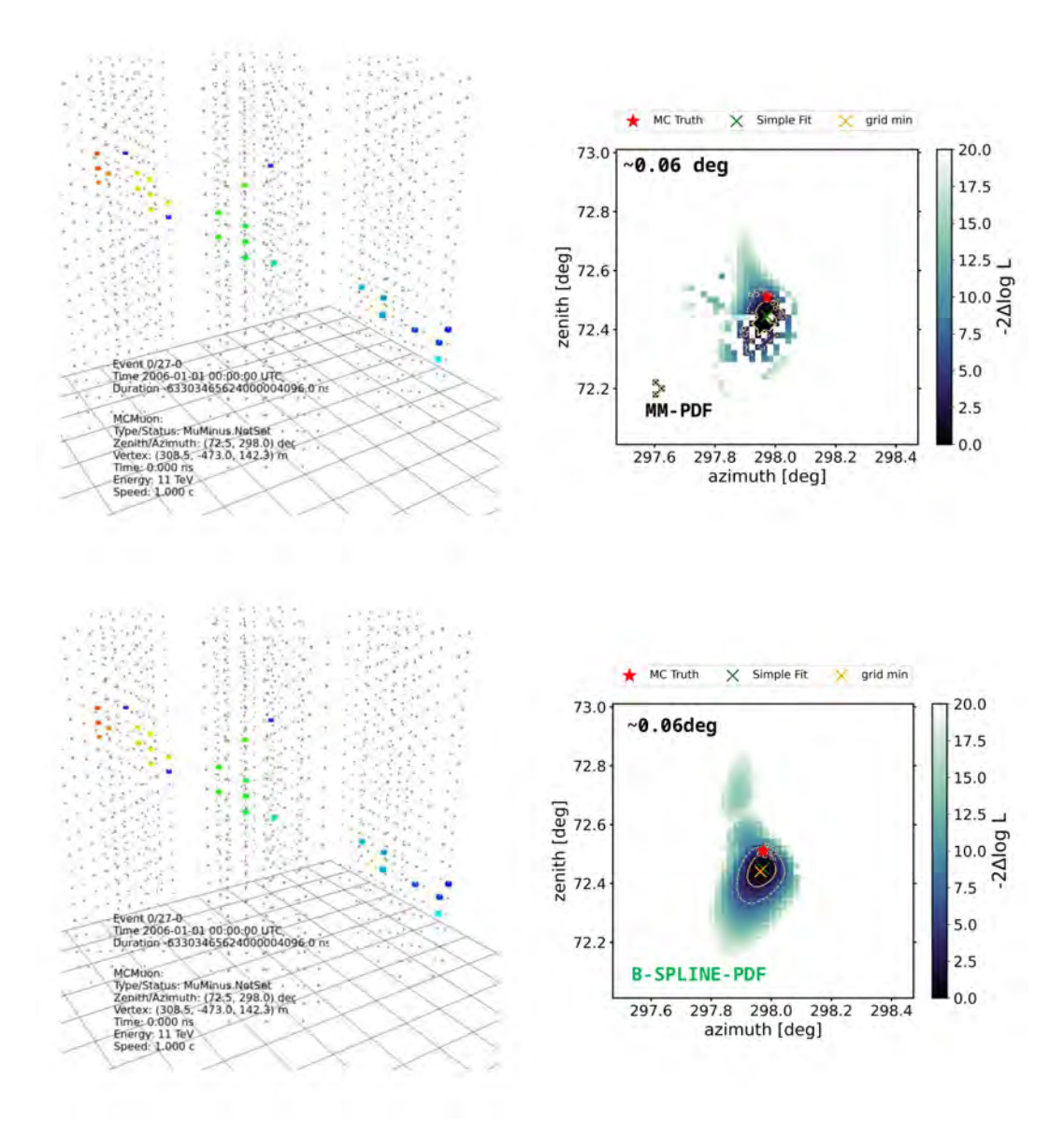
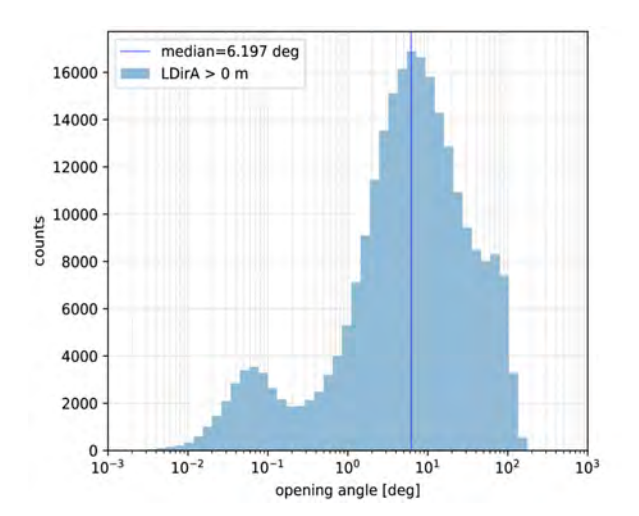


Figure 4.11: The left diagrams are visualizations of a simulated 11 TeV event as it passes through the detector volume in the event viewer. The color-coding indicates the arrival time of the photoelectrons, with red marking early arrivals and green marking late arrivals. The right-hand plots show the profile likelihood scans for the event shown in the left diagrams. The color bar is a test statistic,  $-2(\log \mathcal{L} - \min(\log \mathcal{L}))$ , indicating how much each log-likelihood deviates from the minimum. The green cross shows the direction found by a simple fitter seeded with the Monte Carlo truth for all parameters. The orange cross shows the direction of the minimum likelihood found during the grid scan. The top plots utilize a likelihood based on our mixture model PDF (see Eq. 4.7). The bottom-right plot uses the B-spline PDF parameterization instead of the mixture model shown in Fig. 4.2.2. Figure courtesy of H. Niederhausen.



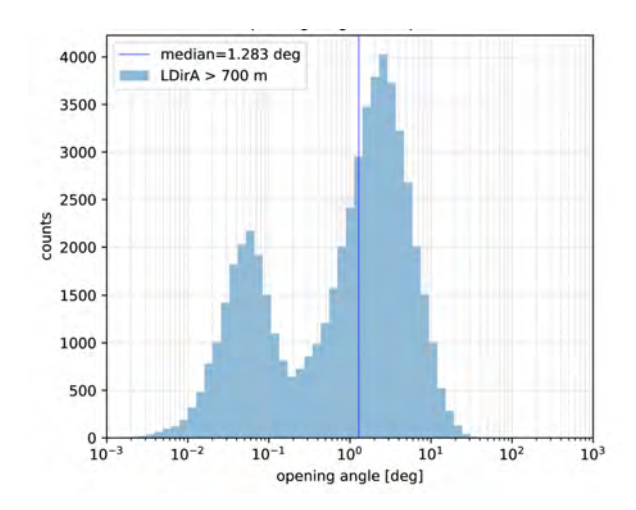


Figure 4.12: Distribution of the opening angles between reconstructed and true direction using a simple fitter and LineFit as seed. For all events in these histograms, the minimizer indicated that it converged, and we selected events that have a valid track length (LDirA: see Sec. 4.4.1). In the left plot, around 93% of events are stuck in local minima. In the right plot, only 25% of the simulated events with track length greater than or equal to 700 m have an opening angle less than 0.1 degree.

 $\hat{\Theta}$  is challenging because it requires global optimization of a nonlinear likelihood function in a five-dimensional parameter space. In addition, because of the low scattering coefficient in ocean water, the correct solutions correspond to very narrow minima in the negative log-likelihood space (see Fig. 4.16 and Fig. 4.18) and are therefore easily missed. Using the simple fitter with a realistic initial guess, such as LineFit algorithm  $^6$ , the minimizer does not converge to the global minimum if the initial starting seed is very far from the solution of the likelihood space, as shown by Fig. 4.12.

#### 4.3.2.1 Numerical Optimization

1327

To address this problem, we employ convolution techniques as represented in Fig. 4.13. The convolution of the time residual PDF with a Gaussian distribution, which is a function of

<sup>&</sup>lt;sup>6</sup>We used the LineFit algorithm implemented in Python using the Icetray software framework and dataclasses [99]. This algorithm does not account for the optical properties and Cherenkov cone of light propagation in the detector medium. However, the IceCube collaboration utilizes an improved Line-Fit algorithm that accounts for corrections for scattering and optical properties [102].

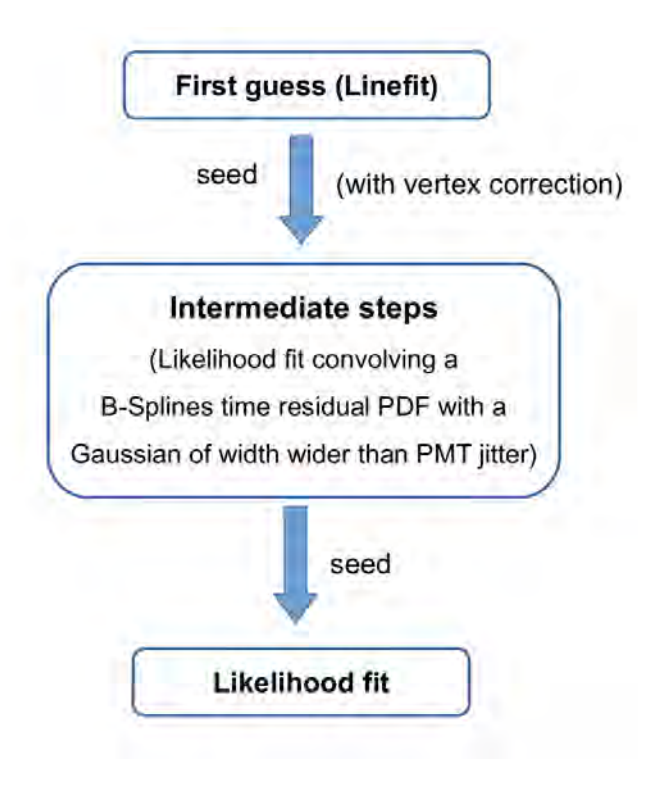


Figure 4.13: Flow diagram for our baseline reconstruction method.

the Gaussian variance, broadens the likelihood minima. One could implement this convo-1330 lution for the mixture model PDF parametrization in Eq. (4.7). However, in addition to 1331 eliminating the numerical instability found using the mixture model PDF (see Fig. 4.18), 1332 the B-Splines PDF already supports this convolution (see Fig 4.14). Therefore, we used the 1333 B-spline PDF as the baseline for the current reconstruction. This reconstruction method 1334 performs a series of Gaussian-convolved likelihood optimizations, starting with  $\sigma = 35 \,\mathrm{ns}$ 1335 (most broadening) and ending with  $\sigma = 0$  ns (no broadening). Each optimization uses start-1336 ing values (seed) taken from the previous solution. The very first fit ( $\sigma = 35 \, \text{ns}$ ) starts from 1337 the result of a LineFit algorithm. This Gaussian-convolved iterative fitting method is vi-1338 sualized in Fig. 4.16. Each minimization is performed using the SIMPLEX algorithm [104]. 1339 The direction of the likelihood minimum and the simple fitter direction move progressively 1340 in the direction of the Monte Carlo truth as the Gaussian width becomes smaller. Therefore, 1341

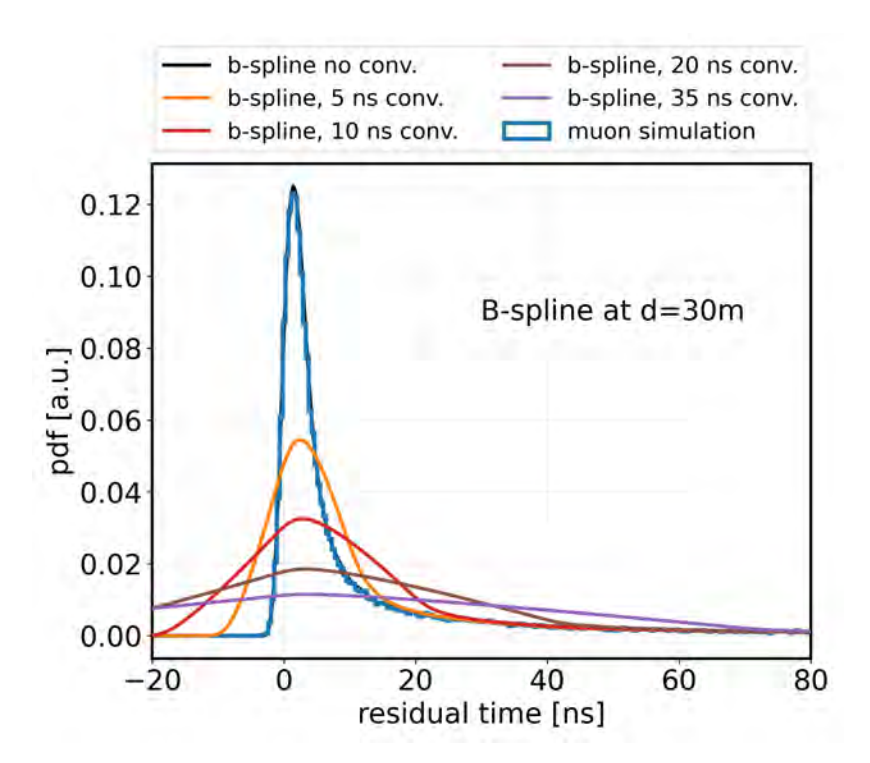


Figure 4.14: An example of B-splines PDFs convolution. The plot shows a histogram of residual times of photons recorded at a distance of 30 m from the emission point on the muon track (blue) and the B-spline (black), as well as convolutions of the B-spline with different Gaussian widths used as a benchmark for reconstruction.

starting with a simple guess, such as LineFit, the idea is that the minimizer will move in 1342 a direction closer to the truth in each iteration step. This works well for some good events, 1343 even if the initial seed direction is far away from the solution of the global minimum, as 1344 shown in Fig. 4.16. However, this method does not work for events with a bad likelihood 1345 space (see Fig. 4.18). Therefore, at present, we do not have a method that guarantees global 1346 convergence. However, when studying the reconstruction performance on simulated muons, 1347 we can approximate global convergence by using the true values of the track trajectory as a 1348 seed to a single-likelihood optimization without convolution. 1349

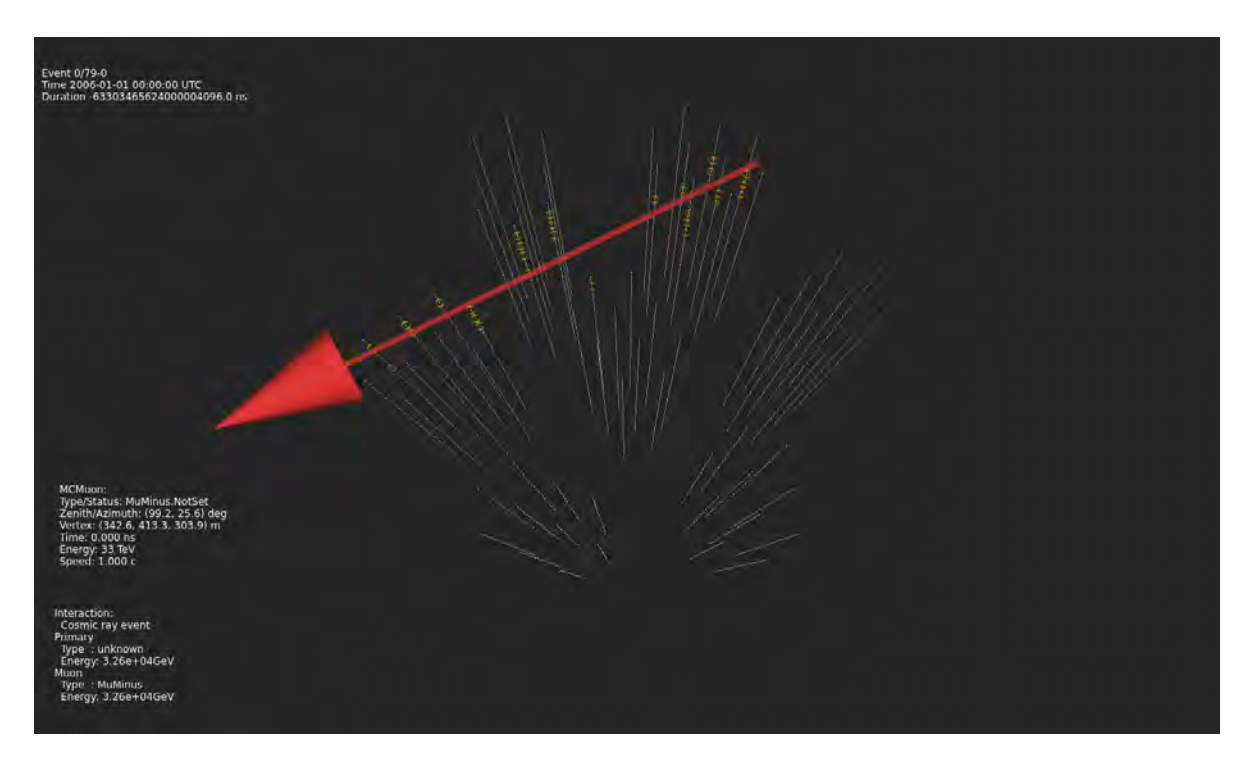


Figure 4.15: A screenshot of the event viewer of a simulated track event of 33 TeV that is estimated to have a visible length of approximately 900 m in the detector volume.

## 4.4 Reconstruction Performance

#### 1351 4.4.1 Event Selection

We studied the performance of the event reconstruction on events that pass the basic simulation trigger level discussed in Ch.3. Additionally, we select events where the reconstruction converged, and we can calculate a reconstructed length <sup>7</sup>.

### 4.4.2 Angular Resolution

1355

To evaluate the performance of our reconstruction method, we use simulated single muons (cf. Ch. 3) with muon energies distributed as  $\propto E^{-1}$  and random trajectories through the

<sup>&</sup>lt;sup>7</sup>For each event we calculate the LDirA quantity, which is the projected distance along the track from the first to the last DOM / PMT with at least one direct hit, with a time residual in the [-15 ns, +15 ns] interval. We used the Direct Hits utility function from the icetray software framework.

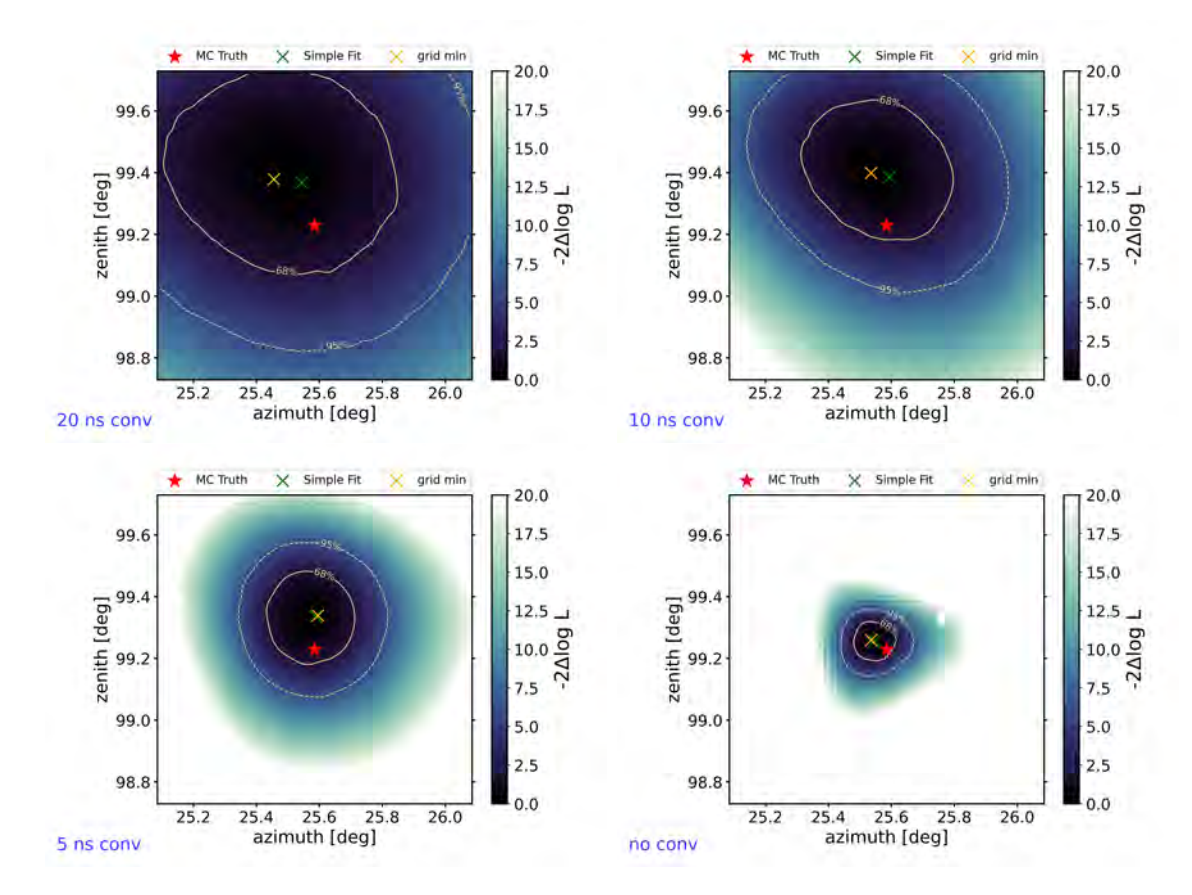


Figure 4.16: Profile scans for simulated event in Fig. 4.15 using 20 ns convolution (upper left), 10 ns convolution (top-right), 5 ns convolution (bottom left). The plot in the bottom right uses no convolution. Additionally, a 35 ns convolution has been performed but is not shown in the plot. For this event, LineFit has an opening angle of 3.24 degrees. A simple fitter starting from LineFit results in an opening angle 2.69 degrees. However, starting from the LineFit seed and performing iterative fits yields an opening angle of 0.053 degrees.

P-ONE detector. We reconstruct these muons using the algorithm in Fig. 4.13 described in Sec. 4.3.2.1. Specifically, we reconstruct each event twice. First, using the Gaussianconvolved iterative likelihood fits, seeded with LineFit at the first convolution iteration ( $\sigma = 35 \, \mathrm{ns}$ ). Second, we performed a likelihood fit using the actual values  $\Theta$  as a seed but without using intermediate steps convolutions. Comparisons between the likelihood values at the respective solutions reveal that those found by the truth-seeded fit generally have values smaller than or equal to those obtained with the Gaussian-convolved iterative fit. Hence, we consider the truth-seeded fits to represent the performance that can be achieved in the

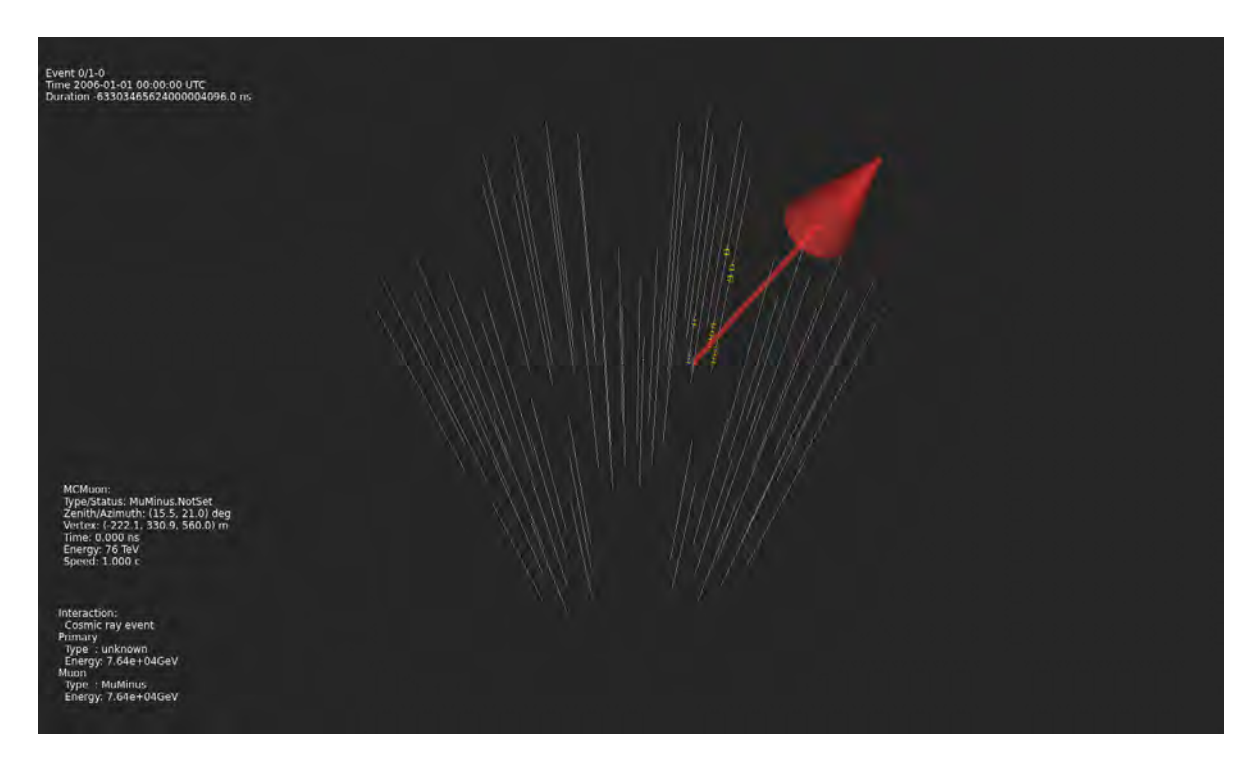


Figure 4.17: A screenshot of the event viewer of a simulated track event of 76 TeV that is estimated to have a visible length of 160 m in the detector volume.

future once global convergence has been further optimized. To quantify the accuracy of the reconstruction, we use the angular distance, or opening angle, between the actual trajectory  $\Theta$  and the estimated one  $\hat{\Theta}$ , as a metric.

Fig. 4.19 shows the median angular resolution as a function of the muon energy for muons 1369 with various minimum track lengths, as computed based on the Gaussian-convolved iterative 1370 fit. Small values of angular resolution arise when long tracks are well reconstructed. The 1371 resolutions are provided for both optimization strategies: Gaussian convolutions and truth 1372 seeding. As expected, accuracy improves with the muon's energy and the estimated length 1373 of its track in the detector. Based on the truth-seeded solutions, we conclude that P-ONE 1374 should be able to reach an angular resolution with  $> 700 \,\mathrm{m}$  muon tracks of  $\sim 0.1^{\circ}$  at  $1 \,\mathrm{TeV}$ , 1375 which improves to  $\sim 0.05^{\circ}$  at 1 PeV. These values are a  $\sim 4$  times better than those currently 1376 achieved by IceCube (blue solid line) [96]. 1377

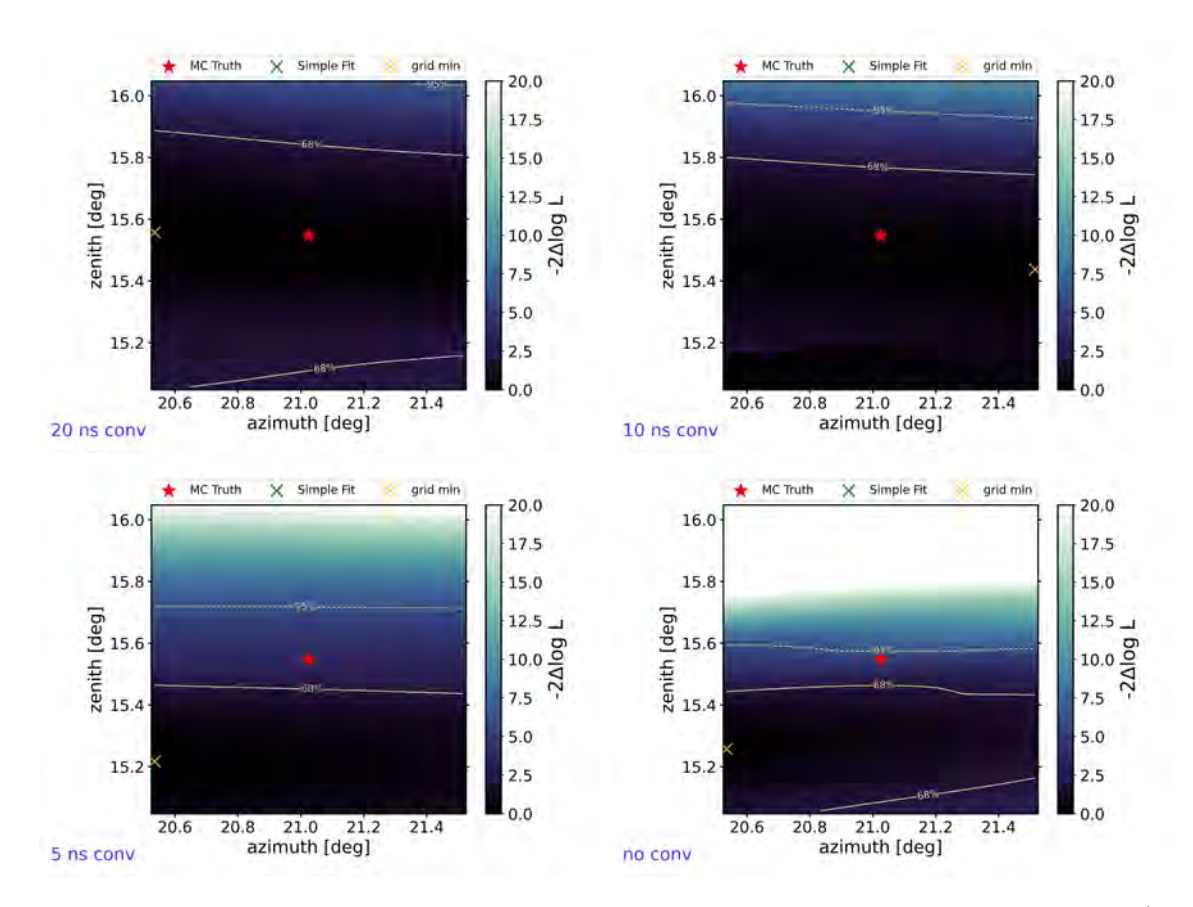


Figure 4.18: Profile scans for simulated event in Fig. 4.17 using 20 ns convolution (upper left), 10 ns convolution (top-right), 5 ns convolution (bottom left). The plot in the bottom right does not use convolution. Additionally, a 35 ns convolution has been performed but is not shown in the plot. For this event, LineFit has an opening angle of 9.02 degrees. A simple fitter starting from LineFit results in an opening angle 2.67 degrees. However, starting from the LineFit seed and performing iterative fits yields an opening angle of 8.34 degrees.

The one-dimensional distribution of the opening angle is shown in Fig. 4.20 for muon tracks with length larger than 700 m (top figure) and 100 m (bottom figure), for both the Gaussian-convolved iterative fits and the truth-seeded method. At the moment, we don't know for sure what the failure mode for the events presents in the second hump in Fig. 4.20 as a result of using Gaussian-convolved iterative fits. It could be a minimizer failure or a local minima in the likelihood space, but further investigation is a subject for future work. Around 74% (63%) of events with track lengths greater than 700 m have opening angles

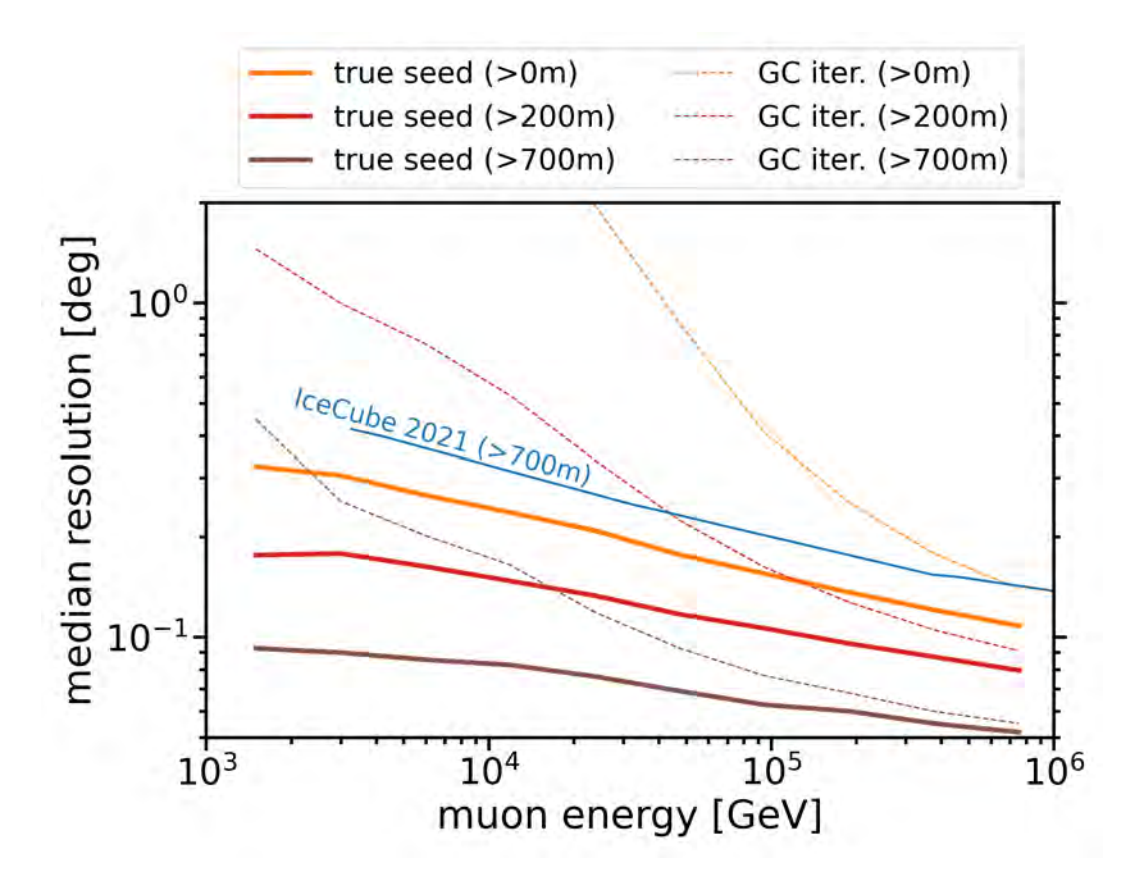


Figure 4.19: The figure shows the median of the opening angle as a function of muon energy for different selections based on the estimated visible track length. The solid lines represent the resolution for the likelihood fit seeded with truth values without using an intermediate step convolution method. The dashed lines are the results using the Gaussian-convolution iterative strategy discussed in Sec. 4.3.2.1. The median was calculated for muon simulations following an energy spectrum of  $E^{-1}$ 

less than 0.1° in the truth-seeded (Gaussian-convolved iterations) method. Ongoing work on global convergence is expected to reduce the population of mis-reconstructed events for the Gaussian-convolved iterations-based method.

## 388 4.5 Outlook

Maximum likelihood reconstruction performance is affected by the initial starting guess. If
the starting points are very far away from the truth, the minimizer may not be able to
converge. Current reconstruction discussed in Sec. 4.3.2.1 can be improved using an initial

guess better than LineFit. The development of improved seed algorithms based on machine learning can provide a better initial seed than LineFit. We investigated the performance of 1393 our current reconstruction if a machine learning reconstruction method were to achieve a  $1^{\circ}$ 1394 resolution. The results of this study are shown in Figs. 4.21 and 4.22. An improved seed to 1395 about 1° resolution will improve current reconstruction performance. As shown in Fig. 4.21, 1396 events in the hump in histogram in Fig. 4.20) will have their angular resolution improved (see 1397 Fig.4.21). This will even increase the statistics of 700 m track length events that even failed 1398 reconstruction, starting with LineFit(see Fig. 4.21 vs Fig. 4.21). As shown in Fig. 4.22, 1399 much improvement is expected for events in the lower energy region and events that have 1400 a track length of more than 700 m. In addition to using an improved starting point, the 1401 current reconstruction can be further enhanced by employing more advanced minimization 1402 techniques, such as using a gradient-based minimization, beyond the simple fit used. 1403

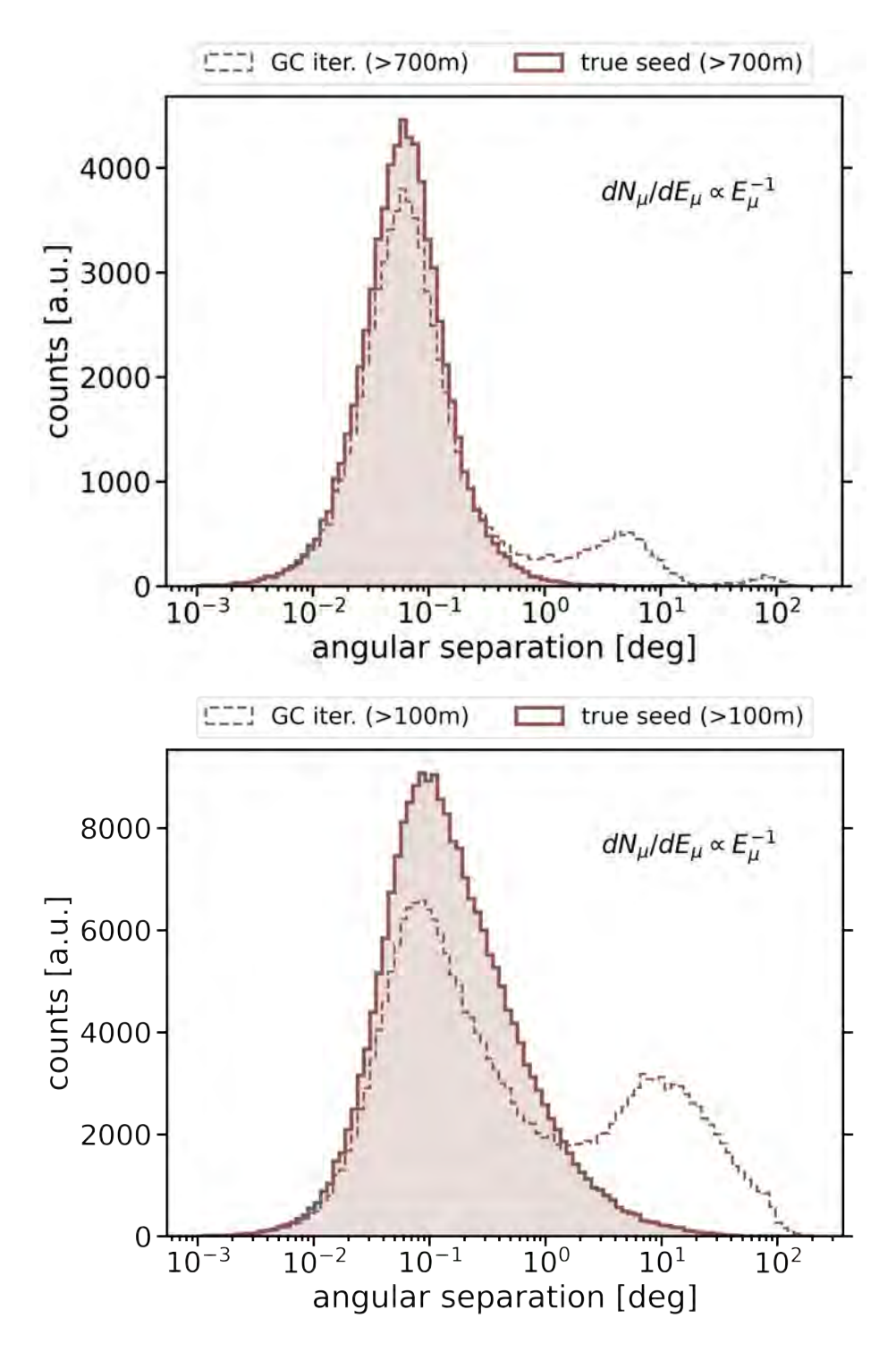


Figure 4.20: The opening angle distribution for muon tracks with a visible length larger than 700 m (top figure) and 100 m (bottom figure). The histograms with a solid line represent the event resolution for the likelihood fit seeded with truth values without using an intermediate step convolution method. The histogram with a dashed line is the result using the Gaussian-convolution iterative strategy.

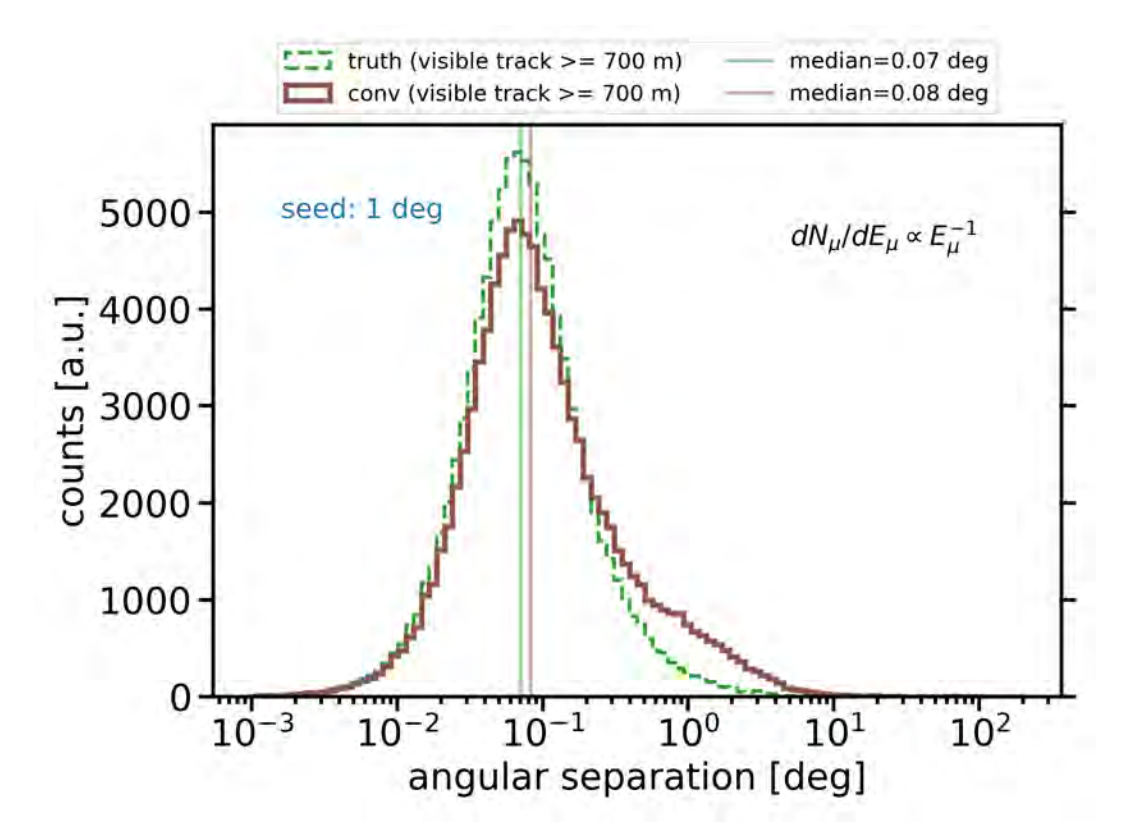


Figure 4.21: Reconstruction performance plot using a hypothetical seed. Using the von Mises-Fisher distribution from scipy [22], we generated hypothetical seeds that are 1 degree away from the event's true directions in median opening angle. The plot shows the distribution of expected angular resolution, starting with these hypothetical seeds that have a 1-degree opening angle.

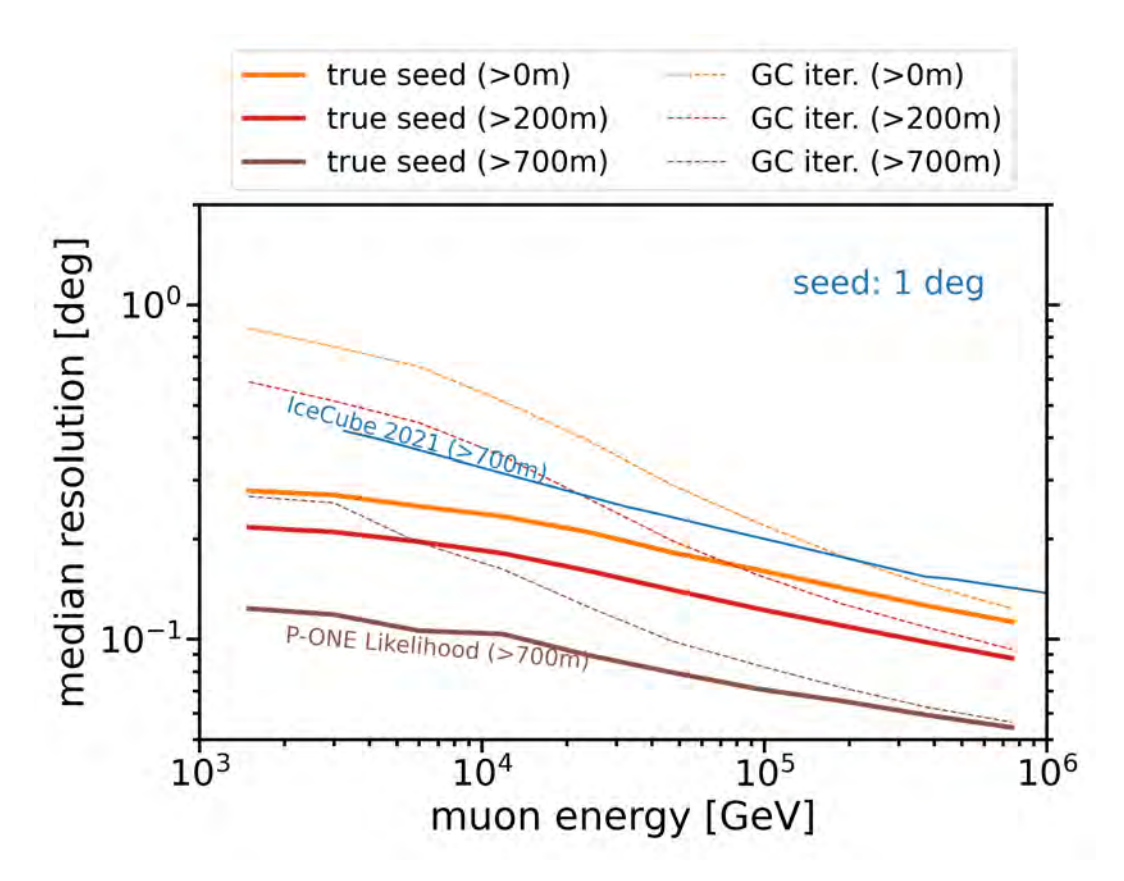


Figure 4.22: Reconstruction performance plot using a hypothetical seed. Using the von Mises-Fisher distribution from scipy [22], we generated hypothetical seeds that are 1 degree away from the event's true directions in median opening angle. The plots show the expected angular resolution as a function of muon energy. The solid lines represent the results of a likelihood fit using a truth seed as the initial guess, without a convolution strategy. The dotted lines indicate the expected performance from the Gaussian-convolution iterations in Sec. 4.2.2 seeded with a hypothetical seed, which is a 1-degree median opening from true event directions.

## Chapter 5

# Neutrino Point Source Analysis

This chapter aims to forecast the sensitivity of P-ONE to steady-state point sources of high-energy astrophysical neutrino events using Monte Carlo simulations. We evaluated the expected performance of P-ONE for some known point source discovered by IceCube. We 1408 extended our calculations to a generic steady-point source located at different declinations. 1409 Sec. 5.1 discusses the Monte Carlo simulation dataset that we use to get a sample of at-1410 mospheric neutrinos as the primary source of background and astrophysical neutrino events. 1411 In Sec. 5.2, we discuss the method used to study the sensitivity of P-ONE based on count-1412 ing the number of events in an angular search bin that encompasses the possible neutrino 1413 source [105, 106]. We determine the flux of a steady-state point source required to observe 1414 excess events above background events at a given significance level [107]. In Sec. 5.3, we 1415 show the expected performance for some known neutrino source, NGC 1068, discovered by 1416 IceCube [23], and for a generic point source at different declinations. 1417

## 5.1 MC Simulation Dataset

#### Neutrino Events

In this analysis, we need a Monte Carlo simulation dataset that includes neutrinos of astrophysical origin and background events from atmospheric neutrinos. The atmospheric neutrino events result from interactions of cosmic rays with the Earth's atmosphere.

We used the LeptonInjector simulation software [79] to obtain a Monte Carlo data set 1423 of neutrino interaction events in the detector. The details of the simulation workflow we 1424 used, from event generation to detector response simulation, are discussed in Ch. 3. These 1425 simulations include muon neutrino events simulated in the energy range from 1 TeV to 1426 1 PeV following the  $E^{-1}$  energy spectrum. This is because below 1 TeV the number of 1427 triggered neutrino events is expected to be negligible for the P-ONE, and above 1 PeV the 1428 astrophysical neutrino flux rate is very small. The latter can be seen from the plot in Fig. 1.3 1429 and the top plot of Fig. 5.1. 1430

These Monte Carlo simulations are reweighted to the desired physical spectra. For diffuse astrophysical events, we used the energy spectrum of  $E^{-2.28}$  and flux normalization measured by IceCube in Ref. [108]. To obtain background events in addition to signal events, we weighted the simulated neutrino events to different physical flux models of atmospheric neutrinos. We used the variants of the flux model H3a\_SIBYLL23C for both conventional and prompt background flux. The IceCube collaboration had already implemented these models in the nuflux library [109].

The plots in Fig. 5.1 show the expected rate of events from the diffuse flux of conventional and prompt atmospheric neutrinos, the diffuse flux of astrophysical neutrinos, and the flux from NGC 1068 [23] as a function of the muon neutrino energy and zenith for a livetime of 10 years. From this weighted Monte Carlo simulation, we obtain a dataset in which we expect approximately 230,000 atmospheric neutrino events from conventional and prompt sources, about 40 neutrino events from NGC 1068, and 4,100 neutrino events from diffuse

<sup>&</sup>lt;sup>1</sup>The conventional and prompt differential fluxes are expressed in units of  $\text{GeV}^{-1} \cdot \text{cm}^{-2} \cdot \text{sec}^{-1} \cdot \text{sr}^{-1}$ . Typically, the event rates are expressed in (Hz) after applying weights to these differential fluxes.

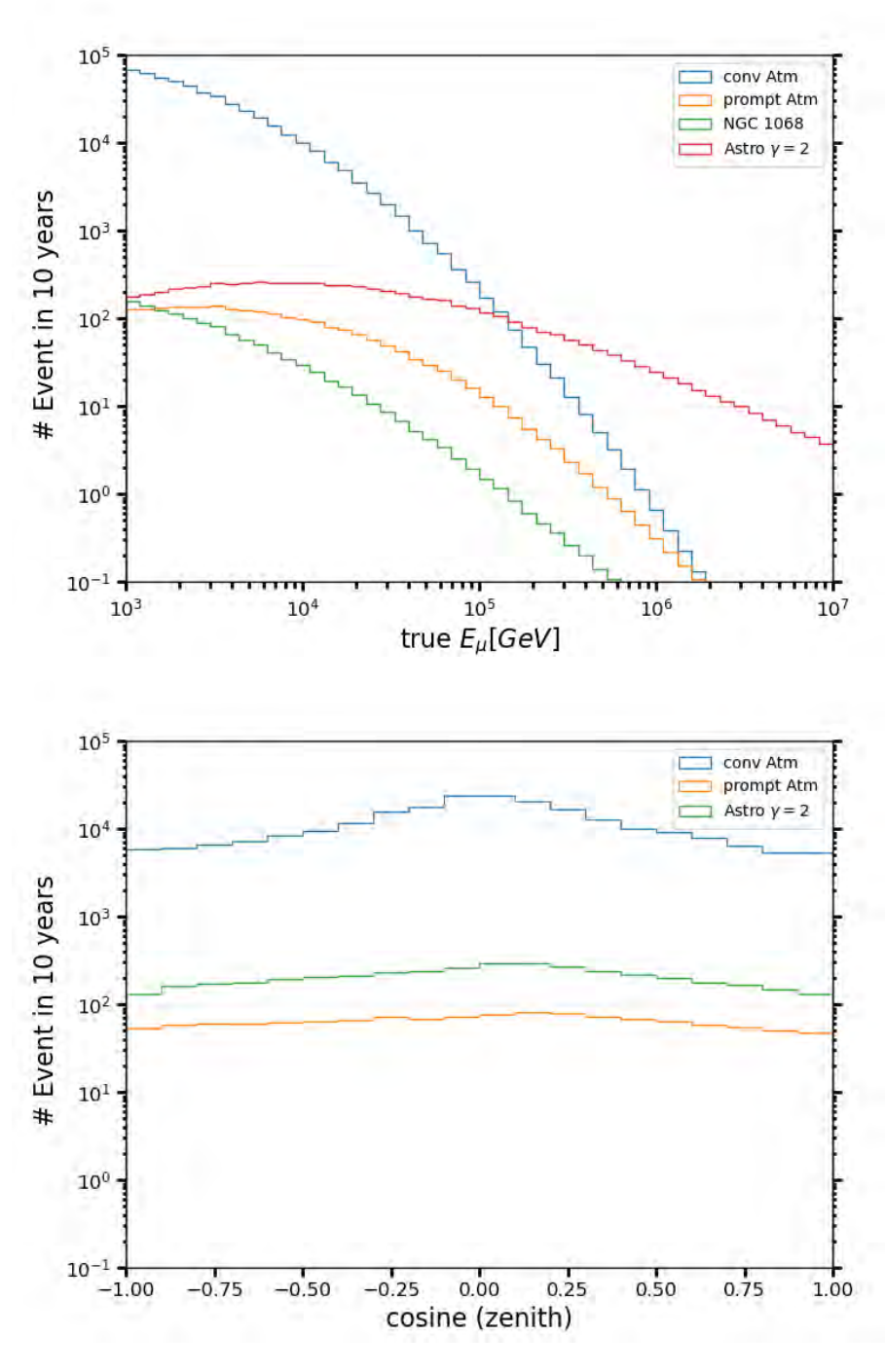


Figure 5.1: Top plot shows the distribution of expected event rate from a flux of conventional and prompt atmospheric neutrinos, a diffuse flux of astrophysical neutrinos, and the flux of neutrino events from NGC 1068 [23] source as a function of muon neutrino energy bin for a livetime of 10 years of P-ONE detector operation. The bottom plot shows the distribution of expected neutrino events as a function of the zenith angle for the fluxes of conventional and prompt atmospheric neutrinos, as well as a diffuse flux of astrophysical neutrinos.

astrophysical sources over 10 years of live time.

#### 1445 Angular Resolution

Each event angular resolution used in this analysis is based on the assumed angular reso-1446 lution, rather than the results of a real reconstruction, due to the problem of convergence 1447 to the global minimum in our current track reconstruction, as discussed in Chapter 4. For 1448 this analysis, we generated a dataset sample with angular resolutions of the events set to 1449 the results obtained by sampling the true directions of MC events using a von Mises-Fisher 1450 (vMF) distribution. For each event, we start with the true event direction from the Lep-1451 ton Injector MC simulation, treating the generated direction as the mean direction for a 1452 von Mises-Fisher distribution and randomly drawing a reconstructed direction based on the 1453 assumed track reconstruction angular resolution. 1454

As discussed in Ch. 4, the angular resolution of the P-ONE detector track is expected to
be less than 0.1 degrees. We sampled the angular resolution of the direction from the proper
direction resolution to create a sample with a median angular resolution of 0.08 degrees

Another caveat in this data sample is that the sampling was done assuming the track
angular resolution is independent of the event energy bin. Therefore, the distribution of
event angular resolution obtained from this sampling across different energy bins appears
flat.

The Fig. 5.2 shows the distribution of opening angles between the Lepton Injector MC simulation event true direction and the sampled direction using the vMF distribution, as-

<sup>&</sup>lt;sup>2</sup>Here the angular resolution is taken as the median of the distribution of opening angle between simulated event true and reconstructed directions. The expected median angular resolution value used here represents the achievable angular resolution limit by the likelihood reconstruction Ch. 4. These were obtained using truth seed instead of Gaussian convoluted strategies as shown in Figs. 4.20 and 4.19.

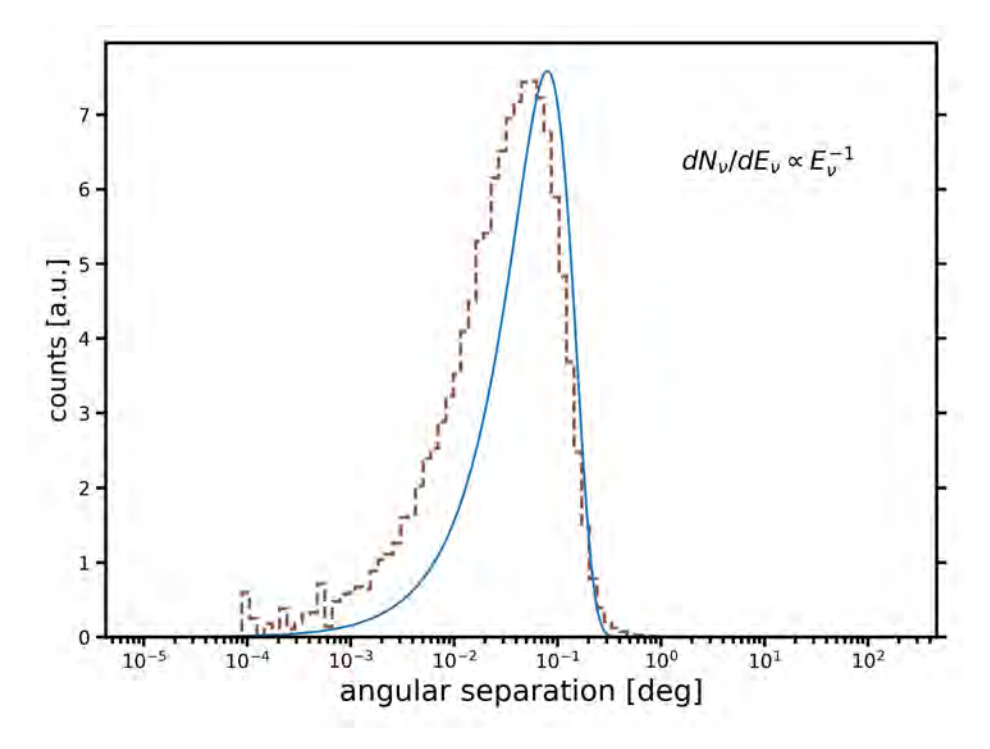


Figure 5.2: The plots show the distribution of the event angular distance between true direction and sampled direction using von Mises-Fisher distribution assuming a median angular resolution of 0.08 degree. The solid line uses the Rayleigh distribution.

suming an expected median angular resolution of 0.08 degrees. The size of angular error for some MC events is shown in Fig. 5.5, where the radius of the circle represents the angular resolution we obtained using this method. For comparison purposes, using this sampling method, we also generated three additional dataset samples with reconstructed directions sampled using a median angular resolution of 1.2, 0.6, and 0.01 degrees for each, as shown in Tables 5.1 and 5.2.

#### 1470 Neutrino Effective Area

To assess the detector efficiency in terms of the number of events that P-ONE would detect,
we compute the effective area. This is the size of the detector expressed as the cross-sectional
area of a target for neutrino interaction. Absorption effects of the Earth are taken into

account when computing the effective area. The effective area depends on both the neutrino energy and the angle of incidence. To calculate the effective area, neutrino events were simulated using LeptonInjector following an  $E_{\nu}^{-1}$  energy spectrum and then reweighted to a signal spectrum of  $E_{\nu}^{-2}$  using LeptonWeighter software [79].

The neutrino effective is calculated as

1478

$$A_{\text{eff}} = \frac{\pi r_{\text{gen}}^2 \Omega_{\text{gen}} \sum_{i} \frac{p_{\text{int},i}}{N p_{\text{gen},i}}}{\Omega \Delta E}$$
(5.1)

where  $\Delta E$  is the range of energies being summed over,  $\Omega_{\rm gen}$  the solid angle over which the simulation was generated,  $\Omega$  the solid angle for which the effective area is being computed,  $p_{{\rm gen},i}$  and  $p_{{\rm int},i}$  are generation and interaction probabilities of the individual event, respectively, and N is the number of generated events.

The plot in Fig. 5.3 shows the neutrino effective area as a function of the neutrino energy for different altitude bands. The effective area increases with neutrino energy for events that reach the detector from above the horizon (i.e., down-going events, with a zenith angle less than 90°). Above 100 TeV neutrino energy, the effective area decreases for neutrino events that travel through the Earth and reach the detector from below (up-going events) as the interaction cross section increases with neutrino energy. Due to the location of P-ONE and Earth's rotation, these events consist of events from the northern sky and the southern sky.

## 5.2 Analysis Method

This analysis assumes a point-like source of high-energy neutrinos that emits events continuously during the detector observation live-time interval. We utilize a method described in

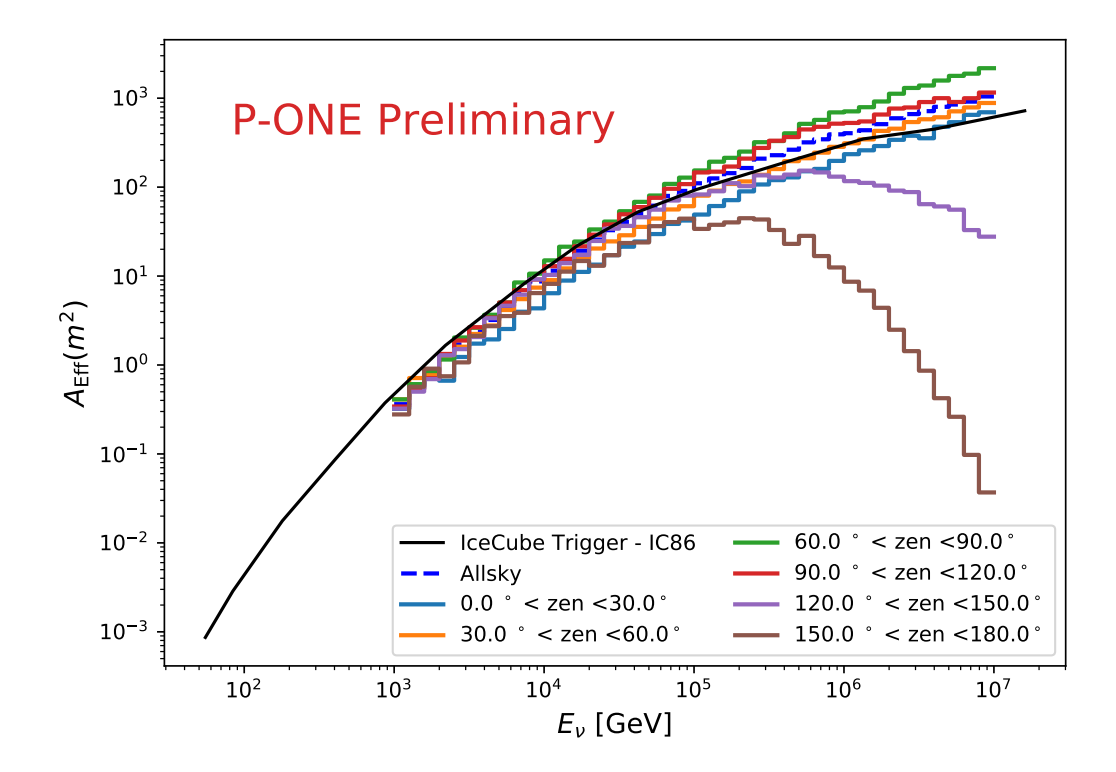


Figure 5.3: Effective area of the simulated P-ONE test geometry (see Fig. 2.15) as a function of neutrino energy for different zenith angle bands at trigger level. The effects of Earth absorption on neutrinos with core-crossing trajectories are visible at high energies for events that enter the detector from below. The trigger applied here looks for events with pulses on at least 3 PMTs within a 10 ns window. The current simulated test geometry has an effective area at trigger level comparable to that of the IceCube detector, as expected based on their comparable geometric volumes [24].

Ref. [105] that counts events in a small angular search bin around a possible source. We then compare this count to the expected number of background events in that bin.

## 5.2.1 Expected Background Events

We used Monte Carlo simulations to calculate the expected number of background events in a search bin surrounding a potential steady-point source. We consider an isotropic background flux across the entire sky. The background event rate does not vary with the azimuthal coordinate and depends only on the altitude coordinate. Additionally, we assume that the background event rate and detector response are uniform across an altitude band that encompasses the source location in local coordinates.

For a given event observation time, we convert the source's position from equatorial co-1502 ordinates (right ascension and declination) to horizontal coordinates (azimuth and altitude) 1503 using a coordinate transformation. We define an altitude band around the source in local 1504 coordinates, within which we calculate the average number of background events in a search 1505 bin. The calculation begins by determining the number of background events within this 1506 altitude band. Then we scale this number to the size of the search bin by the solid angle, as 1507 described in Eq. (5.2). In this analysis, the altitude band width is set to at least 1 degree, 1508 assuming that the event rate remains approximately constant across the band and that it 1509 contains a sufficient number of events for stable estimation. Computing the number of events 1510 in a band first and scaling to the size of the search bin in the band averages the background 1511 event distribution across the altitude band. This provides a more stable background estimate 1512 than purely bin-based event calculations. 1513

The number of expected background events in the bin is given by

1514

$$N_{\text{background}}^{\text{bin}} = \frac{\Delta\Omega}{\Omega_{\text{band}}} N_{\text{background}}^{\text{band}},$$
 (5.2)

where  $\Delta\Omega \approx \pi \Delta \psi^2$  is the solid angle of the bin.  $\Delta\psi$  is the expected angular resolution in radians.  $\Omega_{\rm band} = 2\pi (\sin\theta_2 - \sin\theta_1)$  is the solid angle of the band, and  $\theta_1$  and  $\theta_2$  are the altitude values of the bands such that  $\theta_2 > \theta_1$ .

For a single sidereal day, a distant object should be at the exact location in the local horizontal azimuth and altitude coordinate system, as shown in the Fig.5.4 for the case of NGC 1068 [23]. Therefore, for computational efficiency, we computed the number of

background events for a single day of observation and scaled it to the number of days in the live time under consideration. To calculate the number of background events for a single 1522 day, we divide the day into observation time bins, each covering a half-hour interval. This 1523 resulted in 48 observation time bins for a single day. For each observation time bin, we 1524 compute the location of the source in azimuth and altitude coordinate systems using a time 1525 corresponding to the center of the time bin. Then we computed the expected number of 1526 background events in the time bin,  $N_{\rm background}^{\rm bin}$ , following Eq. (5.2), and the sum for all time 1527 bins for a single observation day. This number is scaled with the days corresponding to the 1528 detector livetime to give the average expected background events. 1529

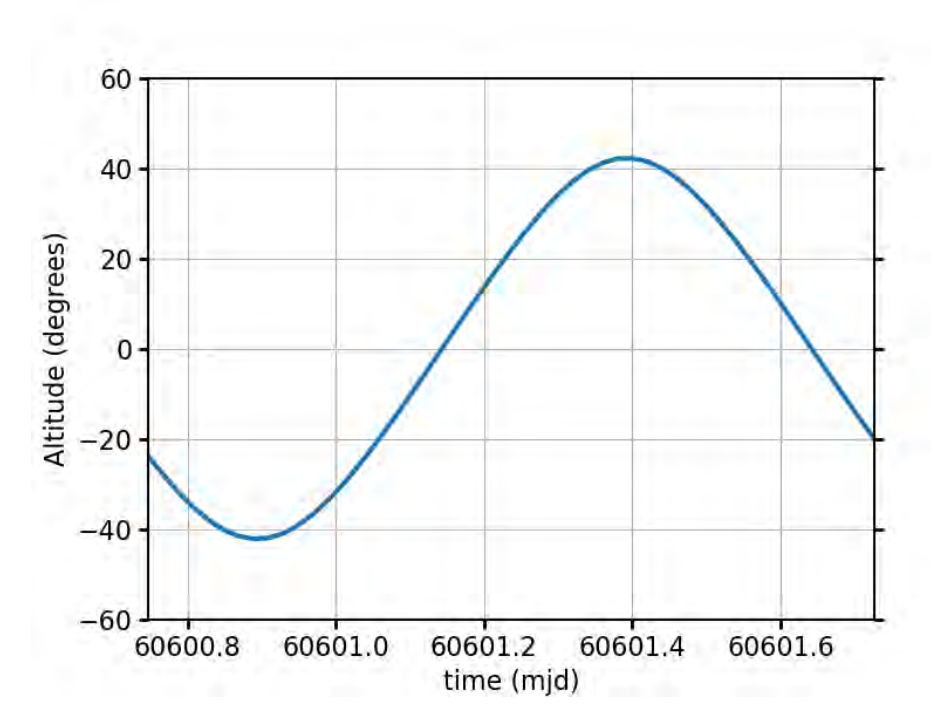


Figure 5.4: The figure shows the altitude as a function of MJD time for the source NGC 1068, as seen by a detector at the P-ONE location over a single day. In subsequent days, the source transits to the same position in the local horizontal coordinates.

### 5.2.2 Expected Signal Events

1538

To compute the expectation of signal events in an angular bin, we use the same procedure described in Sec. 5.2.1. Furthermore, we only use Monte Carlo events with an angular resolution equal to or less than the size of the angular search bin. We use an angular search bin radius of size equal to a factor of 1.58(see Ref. [105]) times 0.08 deg, the expected median of the angular resolution of the track event reconstruction Ch. 4 which bin contains 82% of the signal events. We select all MC events in an altitude band around the source position in local coordinates and weight them based on the source signal flux model.

The number of expected signal events is obtained from the following Eq.  $(5.3)^3$ 

$$\mu_s(\delta_s, \gamma) \equiv \int_0^\infty \int_{t_{\text{start}}}^{t_{\text{end}}} dt \ A_{eff}(E_\nu, \ a_s(\delta_s, \ \alpha_s, \ t)) \ \Phi_s(E_\nu, \ \gamma)$$
 (5.3)

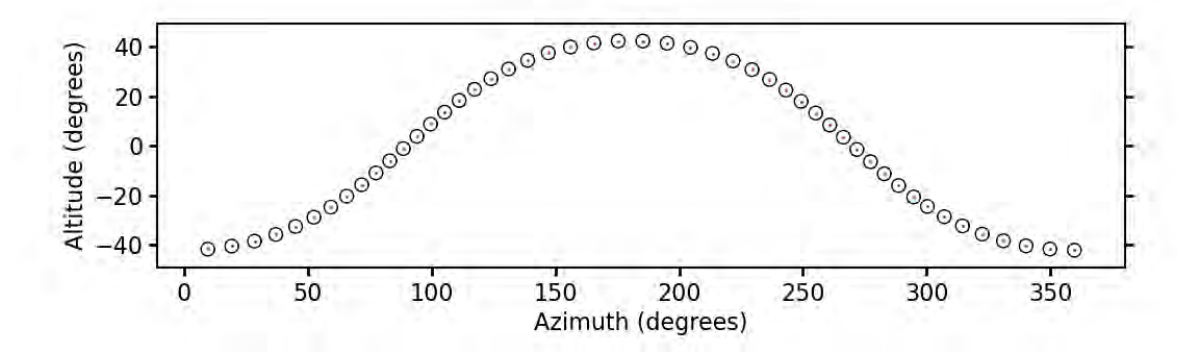
where  $A_{eff}(E_{\nu}, a_s(\delta_s, \alpha_s, t))$  is the detector effective area as a function of event energy  $E_{\nu}$ ,
source altitude  $a_s$ , the latter is in turn a function of the right ascension  $\alpha_s$  and the declination  $\delta_s$  and the observation time of the event t as shown in Fig. 5.4 as an example.  $\Phi(E_{\nu}, \gamma)$  is
the point source flux model as an energy and spectral index function.

For our analysis, we have considered a steady point source with events distributed according to a single power-law flux model [110,111], as given by Eq. (5.4).

$$\frac{d\Phi_{\nu}}{dE_{\nu}} = \Phi_0 \left(\frac{E_{\nu}}{E_0}\right)^{-\gamma} \tag{5.4}$$

with  $\gamma$  the spectral index and  $\Phi_0$  the flux normalization at fixed energy  $E_0$ , which has units of  $\text{GeV}^{-1} \, \text{cm}^{-2} \, \text{s}^{-1}$  from Ref. [23]

<sup>&</sup>lt;sup>3</sup>For expected signal event computation implementation, I give credit to Hans Niederhausen and Martin Wolf from their helpful discussions and their write-up document about Skyllh signal generation development.



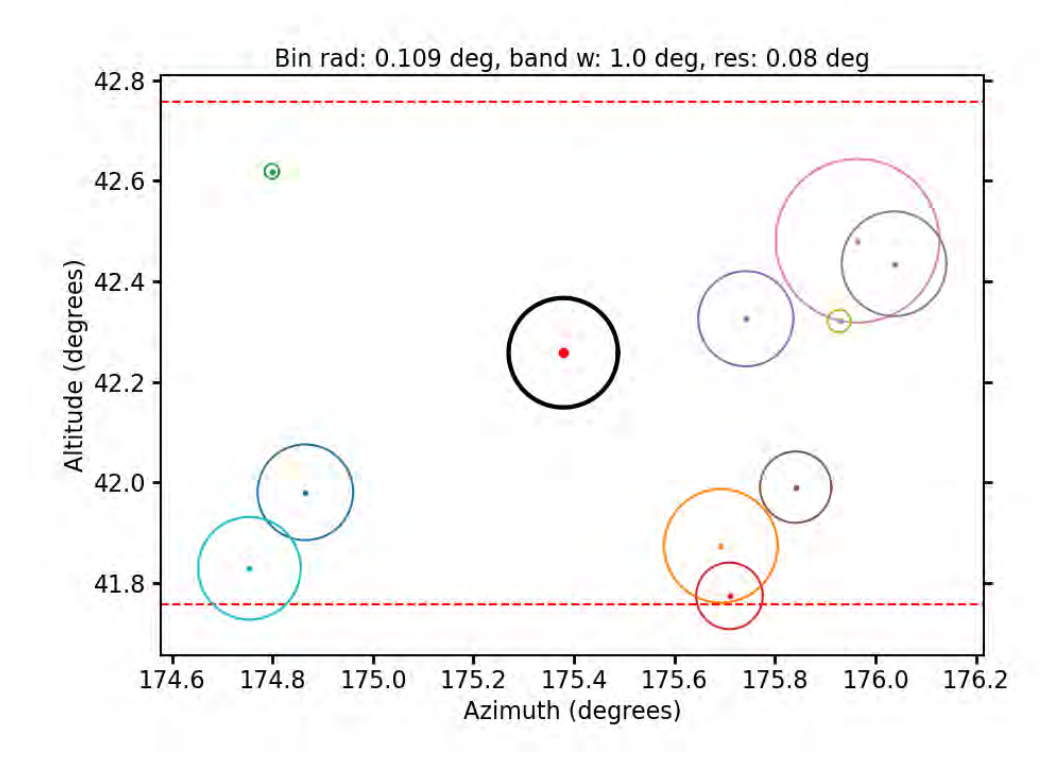


Figure 5.5: The top plot shows the time bins of a single day from discretization. The bottom plot shows a section of the altitude band used when calculating the number of expected events in an angular search bin at one specific central time bin of a day. The dotted red line shows the boundaries of the altitude band. The black circle shows the size of the angular bin. Other circles show the angular error on MC events resulting from vMF sampling with an angular error of 0.08 degrees. Events with smaller circles than the black one are used to calculate the expected signal, while those with larger circles are not counted in during the analysis.

The integral is evaluated by discretizing the integral above into small time segments  $\tau$  of width  $\Delta T_{\tau}$ , each covering a small range in the local coordinate  $a_s(\sigma_s, \alpha_s, t_{\tau})$ ).

$$N_s = \Phi_0 \sum_{\tau} \frac{\Delta T_{\tau}}{\Omega_{\tau}} \sum_{m=1}^{M} \omega_{m,\tau} \left(\frac{E_{m,\tau}}{E_0}\right)^{\gamma}$$
 (5.5)

 $\Omega_{\tau}$  is the solid angle of the band as defined above in Eq. (5.2). The index m is indexed over the number of MC events in the time segment  $\Delta T_{\tau}$ . The term  $\omega_{m,\tau}$  is the Monte Carlo event weight and has unit GeV · sr · cm<sup>2</sup>. The  $E_{m,\tau}$  is the Monte Carlo event energy.

## 5.2.3 Expected Significance

As we expect a good track angular resolution as discussed in Ch. 4, the number of background events,  $N_b$ , within an angular search bin is minimal. For example for both 1-year and 10-year livetimes, the expected background is below one event, given the current median angular resolution of  $0.08^{\circ}$ , as shown in the third rows of Tables 5.1 and 5.2. Therefore, the calculation of statistical significance of any excess (or deficit) using using approximations [112,113] is not valid.

Instead, we rely on significance calculation using exact probability as discussed in Ref. [105].

We estimate the statistical significance of an excess observed above background events in an angular search bin by calculating the probability of Poisson fluctuations of both the observed number of source and background events,  $N_{obs}$ . This involves calculating the probability of detecting N events or more in the source bin, given each possible fluctuation in the total number of observed background events  $N_b$  using Eq. (5.6) as described in Ref. [105]. This means computing the p-value as the probability of counting events equal to or greater than the expected events, under the background-only hypothesis (no signal). The significance

level corresponds to the one-sided tail probability of a Gaussian distribution, Eq. (5.8) as discussed in Ref. [114], Ref. [115].

As the number of events assumes discrete values and follows a Poisson distribution, the significance expectation should be the median over the significances for all possible total numbers of events N from the source bin  $^4$ . To find the weighted median of significance, we first compute the significance for each N using the exact formula in Eq. (5.6) and then weight each computed significance value by the probability of observing exactly N events given a Poisson distribution of expected total events  $N_s + N_b$  using Eq. (5.7).

$$P(N \ge N_{obs} \mid N_b = N_b, N_s = 0) = \left(\sum_{n=N_{obs}}^{\infty} \frac{(N_b)^n e^{-N_b}}{n!}\right)$$
(5.6)

$$=1 - \left(\sum_{n=0}^{N_{obs}-1} \frac{(N_b)^n e^{-N_b}}{n!}\right)$$

$$P(N \mid N_s + N_b) = \frac{(N_s + N_b)^N e^{-(N_s + N_b)}}{N!}$$
(5.7)

p-value = 
$$\int_{Z}^{\infty} \frac{1}{\sqrt{2\pi}} e^{-x^2/2} dx = 1 - \Phi(Z)$$
 (5.8)

where  $\Phi(Z)$  is the cumulative distribution function (CDF) of the standard normal distribution, and the sigma level is given by

$$Z = \Phi^{-1}(1 - p) \tag{5.9}$$

<sup>&</sup>lt;sup>4</sup>The value of N can be very large, but if N is a multiple large factor of the size of expected events  $N_S + N_b$ , the probability of observing more than in this case will be almost zero. Hence, for computation purposes, we use N up to a factor of three higher than the expected number of events from the source,  $N_S + N_b$ .

where p is the p-value obtained from Eq. (5.6).

## 5.3 Expected Performance

This section provides a detailed description of the expected performance for the NGC 1068 source discovered by IceCube [23], as well as the expected sensitivity to generic steady neutrino point sources at different declinations.

### 1582 5.3.1 Observing NGC 1068

To estimate the sensitivity of P-ONE for observing NGC 1068, we used a power-law flux 1583 model measured by IceCube from Ref. [23]. The best-fit flux normalization at neutrino 1584 energy of 1 TeV is  $5.0 \times 10^{-11} \text{ TeV}^{-1} \text{cm}^{-2} \text{s}^{-1}$ , and the spectral index is 3.2. To study 1585 how the angular resolution affects the sensitivity to the point source, we also compared the 1586 observation of NGC 1068 by P-ONE with the observation of a detector located at the P-1587 ONE location with different assumed median angular resolutions shown in Tables 5.1 and 1588 5.2. From the LeptonInjector simulation, we generated four different muon neutrino datasets 1589 based on the median track angular resolution. To obtain each data set, we used the same 1590 sampling procedure to assign reconstructed neutrino directions, using a von Mises-Fisher 159 distribution as described in Sec. 5.1. 1592

For each dataset, using the method described in Sec. 5.2.1, we compute the expected background events in the angular search bin, which depend on the assumed angular resolution under consideration. We also compute the number of signal events expected observing NGC 1068 using the same angular search bin using the method discussed in Sec. 5.2.2. Once the expected background events and signal events in each angular search bin have been

computed, the significance was calculated using the method described in Sec. 5.2.3.

Tables 5.1 and 5.2 show expected background and signal events and the corresponding 1590 significances for the NGC 1068 neutrino source, assuming a power-law flux, assuming dif-1600 ferent angular reconstruction resolutions for 1-year and 10 year livetimes. A good angular 1601 resolution allows the use of a smaller angular search bin. This implies that the number 1602 of expected background events is significantly reduced due to the small size of the spatial 1603 search bin, thereby increasing the expected significance level of the excess above background 1604 events. The likelihood track reconstruction of P-ONE predicts an angular resolution of 0.08 1605 degrees. From the Tables 5.1 and 5.2, with this resolution we expect less than one back-1606 ground neutrino event per year for P-ONE, and in fact less than one event even in 10 years 1607 of observation. This indicates that P-ONE can observe NGC 1068 in less than a year with 1608 more than  $5\sigma$  significance. 1600

We also calculated the significance of P-ONE for observing NGC 1068 for different detector livetimes as sshownin Fig. 5.6. This figure also indicates that P-ONE can observe NGC 1068 with five-sigma significance in less than 1 year.

Table 5.1: Expected bkg and NGC 1068 signal events / 1 year livetime

resolution in deg	Background $(N_b)$	Signal $(N_s)$	Significance
1.20	6.6	4.0	1.4
0.60	1.65	4.0	2.4
0.08	0.03	4.0	5.6
0.01	0.0005	4.0	8.0

Table 5.2: Expected bkg and NGC 1068 signal events / 10 years livetime

resolution in deg	Background $(N_b)$	Signal $(N_s)$	Significance
1.20	66.3	40	4.6
0.60	16.6	40	7.7
0.08	0.30	40	17.7
0.01	0.005	40	25.4

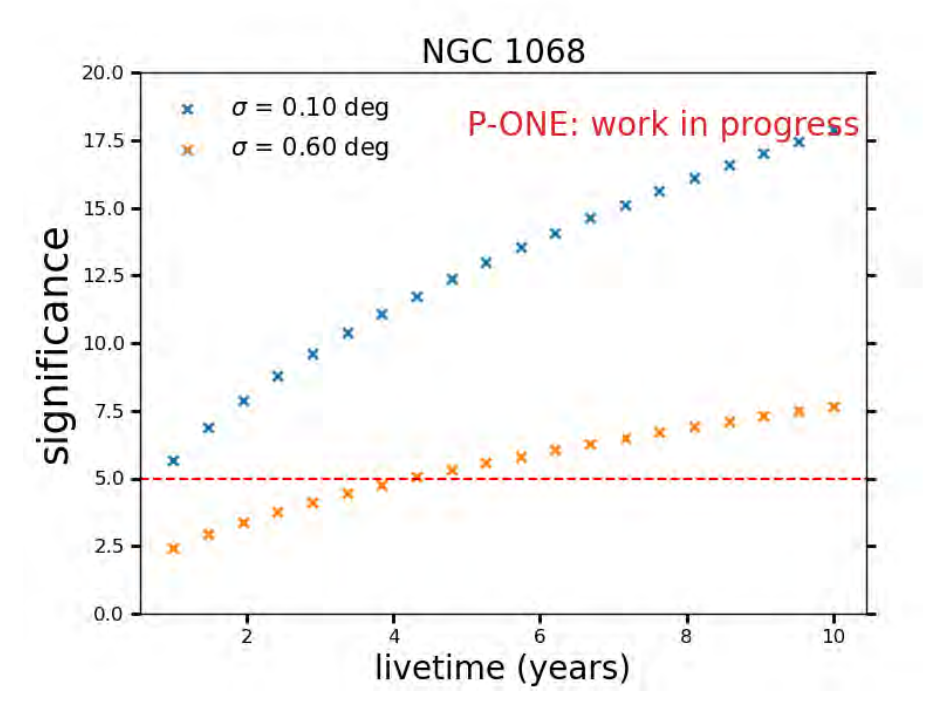


Figure 5.6: The significance of observing NGC 1068 [23] for different observation times. The blue line shows the performance expectation of the P-ONE based on our angular resolution assumption of 0.08 degrees. In contrast, the orange line shows the performance for a detector with an expected median angular resolution of 0.60 degrees.

## 5.3.2 Discovery Potential

1613

In this section, we evaluate the performance of the P-ONE in observing steady point sources located at different declinations in the sky. We are interested in computing the number of events needed to give a 5-sigma significance from observing a steady point source. We also calculate the corresponding flux and discovery potential. For a single source at a given declination, by scaling the source flux and using the method discussed in Sec. 5.2.3 to compute

the significance, we find a minimum flux (see Eq. (5.10)) that gives the number of events that produce an observation median significance level close to a 5-sigma.

Here, the significance of 5-sigma is calculated as the probability of the observation being

$$P(n_{5\sigma}^{obs} \mid N_s + N_b) \le 2.85 \times 10^{-7}$$
 (5.10)

less than  $2.85 \times 10^{-7}$ , from the one-sided tail of a normal distribution Eq. (5.8) and Eq. (5.9). 1622 This calculation assumes a lifetime of 10 years of detector operation, observing a source with 1623 a flux model given by a power-law flux with a spectral index of 2. The same procedure 1624 is repeated for steady point sources with different declinations to determine the discovery 1625 potential and the corresponding number of events that yield a 5-sigma significance. To inves-1626 tigate how the sensitivity scales with angular resolution, we also calculate the performance 1627 of a hypothetical detector with a median angular resolution of 0.60 degrees. 1628 The results in Fig. 5.7 indicate that P-ONE will be able to discover a steady point source 1629 with a spectral index flux of  $\gamma = 2$  by only observing about five events from that source, 1630 as shown by the orange line in the top plot of Fig. 5.7. The corresponding flux, discovery 1631 potential, that would produce 5-sigma in 10 years is  $0.5 \times 10^{-12} \, \text{TeV}^{-1} \, \text{cm}^{-2} \, \text{s}^{-1}$  at 1 TeV 1632

#### 5.3.3 Event Selection Method

reference energy, as shown in the bottom plot of Fig. 5.7.

1621

1633

1634

To purely use tracks from astrophysical origin and suppress background from atmospheric neutrinos and muons, point source analyses focus on tracks entering the detector from below.

Using these track events, IceCube has demonstrated improved point source sensitivity in the northern sky [23]. Because of the location of P-ONE, a neutrino point source in the sky will

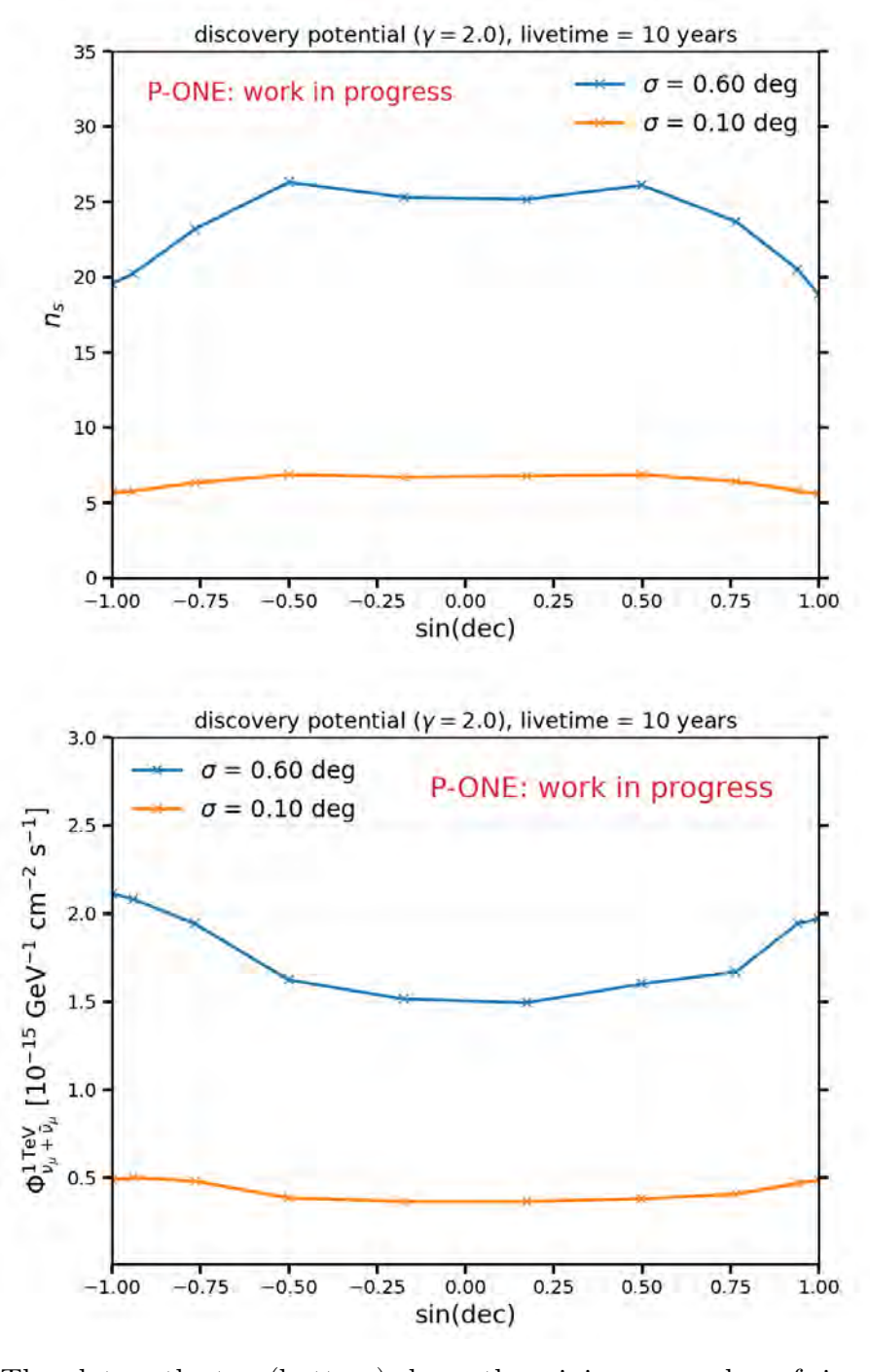


Figure 5.7: The plot on the top (bottom) shows the minimum number of signal events (flux) needed to reach a discovery potential with a significance of 5 sigma over 10 years exposure for a  $\gamma=2$  source at different declinations. The blue lines in both plots indicate predictions for a detector located at the P-ONE location for a median angular resolution of the track reconstruction of 0.6 degrees.

appear at different positions in local coordinates over the course of a day. And therefore for a single day of observation, events from the source can be observed at different altitude positions, depending on the source's location and the time of day. An example of the location of NGC 1068 for a single day is shown in Fig. 5.4.

At the time of writing, the Monte Carlo simulation available for this analysis does not in-1643 clude atmospheric muon background events. It only includes simulated astrophysical neutri-1644 nos and atmospheric neutrinos. Thus, the results shown in Fig. 5.7 are based on a calculation 1645 of the expected atmospheric neutrino background events in each bin, neglecting atmospheric 1646 muons. To account for the atmospheric muon background effect in the calculation, we only 1647 selected Monte Carlo simulation events that reached the detector from below. In reality, this 1648 selection would prevent including atmospheric muons and neutrinos that reach the detector 1649 from above in the analysis. 1650

The results of this selection, shown in Fig. 5.8, indicate that detecting the same number of signal events requires a higher source flux for a given live-time compared to the case without this selection (see Fig. 5.7). Moreover, a source located in the southern sky is approximately twice as detectable as one in the northern sky. Also P-ONE is unable to observe up-going events (tracks) originating from declinations beyond about 42°.

## 5.4 Outlook

The results presented in this chapter were obtained using a simple analysis. This analysis does not account for the dependence of the angular reconstruction resolution on event energy.

We used the same assumed angular error distribution for each event when sampling the directions of the reconstructed events. Future work, including an optimized reconstruction

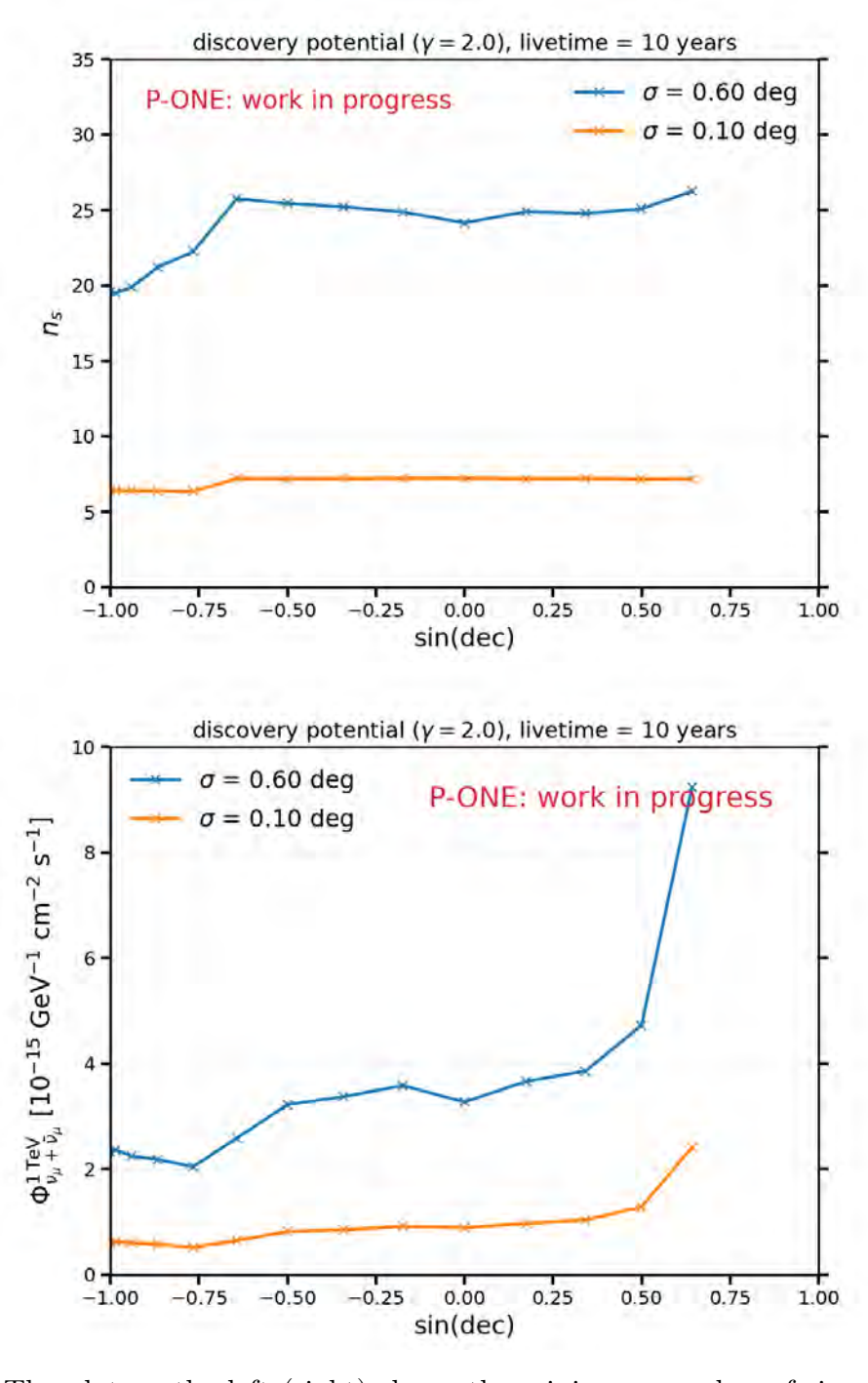


Figure 5.8: The plot on the left (right) shows the minimum number of signal events (flux) needed to reach a discovery potential with a significance of 5 sigma over 10 years exposure for a  $\gamma=2$  source at different declinations. The blue lines in both plots indicate predictions for a detector located at the P-ONE location for a median angular resolution of the track reconstruction of 0.6 degrees.

can further improve the analysis presented here by incorporating the energy dependence of the angular resolution of events. Moreover, adopting an unbinned analysis method will improve sensitivity in distinguishing the signal from the background within the search region. This method assigns a higher probability of being from the source to an event originating near the source than to one from the background.

# Chapter 6

# Conclusions

Pacific Ocean Neutrino Experiment is a km<sup>3</sup> scale neutrino telescope planned to be deployed 1668 in the northern hemisphere at the Cascadia Basin to advance the field of neutrino astronomy 1669 by complementing existing and under-construction neutrino telescopes. P-ONE collaboration 1670 deployed two Pathfinder missions, STRAW and STRAW-b, in 2018 and 2020, respectively, 1671 aimed at measuring the optical properties and assessing the feasibility of deployment at the 1672 Cascadia Basin. Following the successful deployment, operation, and decommissioning of the 1673 P-ONE pathfinder missions from 2018 to 2023, the P-ONE collaboration is now developing 1674 and working towards realizing P-ONE arrays of detector instruments. 1675

This thesis focuses on forecasting the sensitivity of the Pacific Ocean Neutrino Experiment to steady-point sources of astrophysical neutrinos. This involved producing a detailed
Event Monte Carlo simulation, developing a track directional reconstruction algorithm, and
conducting a statistical data analysis to estimate the discovery potential, flux needed to
discover a steady-point source.

In this thesis, we reported a detailed event Monte Carlo simulation pipeline in P-ONE using tools developed by the IceCube Neutrino Observatory collaboration. The current simulation utilizes a test geometry, and an ongoing effort is underway to develop an optimal geometry design. We have developed a basic model of detector response simulation for this first detailed Monte Carlo simulation. The detector response model simulation needs

improvement of the background noise simulation, in addition to the signal from the physics
event simulation. This involves incorporating a bioluminescence model and a background
model on a potassium-40 simulation conducted by a collaborator in the simulation pipeline.
Another aspect of the event simulation work that needs improvement is the detector response
model using lab data, which the collaboration is working on. Nevertheless, this initial version
of the Monte Carlo is sufficient for us to estimate the expected angular resolution of P-ONE
and its sensitivity to astrophysical neutrino sources.

The ability of a neutrino telescope to discover astrophysical sources of high-energy neutrinos depends significantly on its angular resolution. P-ONE is being developed for deployment in ocean water, where scattering is reduced compared to in-ice scattering, and will utilize the latest technology to achieve a good timing resolution. It is expected to have a good angular resolution. We reported a track event reconstruction algorithm we developed for the P-ONE using Monte Carlo simulation. The algorithm is based on a maximum-likelihood method and convolution techniques to deal with very narrow likelihood spaces near the solutions.

At the time of writing, we do not have a method that guarantees global convergence 1700 for all events at the trigger level. Hence, used truth-seeded fits as representative of the 170 performance that will be achievable in the future, once the global convergence has been 1702 further optimized. We found that for muon tracks with more than > 700 m in track length, 1703 P-ONE can potentially reach an angular resolution of  $\sim 0.1^{\circ}$  at 1 TeV, which improves to 1704  $\sim 0.05^{\circ}$  at 1 PeV. These values are a factor of  $\sim 4$  better than those currently achieved by 1705 IceCube. Maximum likelihood reconstruction performance is affected by the initial starting 1706 guess. If the starting points are very far away from the truth, the minimizer may not be able 1707 to converge. The current reconstruction discussed can be improved by using an initial guess 1708 that is better than LineFit, such as the development of improved seed algorithms based 1700

on machine learning. Additionally, the current reconstruction can be further enhanced by employing more advanced minimization techniques, such as gradient-based minimization.

We discuss the method used to study the sensitivity of P-ONE based on counting the 1712 number of events in an angular search bin that encompasses the possible neutrino source. 1713 We determine the flux of a steady-state point source required to observe excess events above 1714 background events. The results suggest that P-ONE can observe NGC 1068 in less than a 1715 year with more than  $5\sigma$  significance due to its expected angular resolution that reduces the 1716 angular search bin. P-ONE will be able to discover a steady point source, depending on 1717 the energy and flux, by observing as few as seven events from that source with a few years 1718 of operation. The results presented in this study were obtained using a simple analysis. 1710 This analysis does not account for the dependence of the angular reconstruction resolution 1720 on event energy. Once the reconstruction optimizations are solved, the analysis can be im-1721 proved by taking into account the angular resolution energy dependence. Future analysis 1722 of point source sensitivity can utilize robust methods, such as unbinned analysis methods, 1723 which are more sensitive to discriminate the signal event from the background event in the 1724 search bin. At the moment of writing this thesis, there is an ongoing work on adapting 1725 tools used in other neutrino telescopes at the P-ONE location that will be used for point 1726 source analysis. Nevertheless, the results from this thesis will serve as a baseline for future 1727 performance analysis, including geometry optimization for a detector that maximizes sci-1728 ence output while considering cost and physical infrastructure constraints, and fits within 1720 engineering constraints. 1730

REFERENCES

#### REFERENCES

- [1] P. D. Group, J. Collaboration, et al., "Beringer et al., "review of particle physics (rpp),"," Phys. Rev. D, vol. 86, p. 010001, 2012.
- [2] Wikipedia contributors, "Standard model." https://en.wikipedia.org/wiki/ Standard\_Modelhttps://en.wikipedia.org/wiki/Standard\_Model. Accessed: 2025-08-26.
- [3] C. Spiering, "Astroparticle physics in europe: Status and perspectives," Reviews in Modern Astronomy: Cosmic Matter, vol. 20, pp. 375–405, 2008.
- [4] D. R. Cantu, Search for extended galactic sources of astrophysical neutrinos with the icecube neutrino observatory. Michigan State University, 2021.
- [5] Wikipedia contributors, "Cherenkov radiation." https://en.wikipedia.org/wiki/ Cherenkov\_radiation. Accessed: 2025-08-26.
- [6] C. Kopper, R. the KM3NeT Consortium, et al., "Performance studies for the km3net neutrino telescope," Nuclear Instruments and Methods in Physics Research Section A:

  Accelerators, Spectrometers, Detectors and Associated Equipment, vol. 692, pp. 188–191, 2012.
- [7] V. Allakhverdyan, A. Avrorin, A. Avrorin, V. Aynutdinov, Z. Bardačová, I. Belolaptikov, E. Bondarev, I. Borina, N. Budnev, V. Chadymov, et al., "Overview of the baikal-gvd neutrino telescope: 2024 status," in *EPJ Web of Conferences*, vol. 319, p. 04002, EDP Sciences, 2025.
- [8] KM3NeT Collaboration, "KM3NeT: The next-generation neutrino telescope." https://www.km3net.org/, 2025. Accessed: August 27, 2025.
- [9] M. G. Aartsen, M. Ackermann, J. Adams, J. Aguilar, M. Ahlers, M. Ahrens, D. Altmann, K. Andeen, T. Anderson, I. Ansseau, et al., "The icecube neutrino observatory: instrumentation and online systems," Journal of Instrumentation, vol. 12, no. 03, p. P03012, 2017.
- [10] L. J. Schumacher, M. Huber, and M. Bustamante, "Plenum software tools." https://github.com/PLEnuM-group/Plenum, 2023. Accessed: 2024-03-04.
- 1759 [11] N. Bailly, J. Bedard, M. Böhmer, J. Bosma, D. Brussow, J. Cheng, K. Clark,
  1760 B. Croteau, M. Danninger, F. De Leo, et al., "Two-year optical site characterization
  1761 for the pacific ocean neutrino experiment (p-one) in the cascadia basin," The European
  1762 Physical Journal C, vol. 81, no. 12, p. 1071, 2021.

- [12] K. Holzapfel, Bioluminescence in the Pacific ocean neutrino experiment: shedding light on the deep sea. PhD thesis, Ph. D. thesis, Technical University of Munich, Munich, Germany, 2023.
- [13] C. Spannfellner, P.-O. Collaboration, et al., "Design of the pacific ocean neutrino experiments first detector line," in 38th International Cosmic Ray Conference, p. 1219, 2024.
- [14] F. Henningsen, "Pacific ocean neutrino experiment: Expected performance of the first cluster of strings," in 38th International Cosmic Ray Conference, p. 1053, 2024.
- 1771 [15] M. Agostini, S. Agreda, A. A. Wight, P. Barbeau, A. Baron, S. Bash, C. Bellenghi,
  1772 B. Biffard, M. Boehmer, M. Brandenburg, et al., "Prototype acoustic positioning sys1773 tem for the pacific ocean neutrino experiment," Journal of Instrumentation, vol. 20,
  1774 no. 07, p. P07003, 2025.
- 1775 [16] M. Agostini, M. Böhmer, J. Bosma, K. Clark, M. Danninger, C. Fruck, R. Gernhäuser,
  A. Gärtner, D. Grant, F. Henningsen, et al., "The pacific ocean neutrino experiment,"
  Nature Astronomy, vol. 4, no. 10, pp. 913–915, 2020.
- 1778 [17] J. P. Twagirayezu, H. Niederhausen, S. Sclafani, N. Whitehorn, M. Nisa, S. Yu, and R. Halliday, "Performance of the Pacific Ocean Neutrino Experiment (P-ONE)," *PoS*, vol. ICRC2023, p. 1175, 2023.
- [18] C. Haack, L. J. Schumacher, P.-O. Collaboration, et al., "Machine-learning aided detector optimization of the pacific ocean neutrino experiment," in 38th International Cosmic Ray Conference, p. 1059, 2024.
- [19] J. Ahrens *et al.*, "Muon track reconstruction and data selection techniques in AMANDA," *Nucl. Instrum. Meth. A*, vol. 524, pp. 169–194, 2004.
- [20] N. van Eijndhoven, O. Fadiran, and G. Japaridze, "Implementation of a gauss convoluted pandel pdf for track reconstruction in neutrino telescopes," *Astroparticle Physics*, vol. 28, no. 4-5, pp. 456–462, 2007.
- [21] I. collaboration, "Icetray documentation." Accessed: 2025-10-05.
- [22] Scipy, "von mises—fisher distribution." Accessed: 2024-10-05.
- [23] I. Collaboration\*†, R. Abbasi, M. Ackermann, J. Adams, J. Aguilar, M. Ahlers, M. Ahrens, J. Alameddine, C. Alispach, A. Alves Jr, et al., "Evidence for neutrino emission from the nearby active galaxy ngc 1068," Science, vol. 378, no. 6619, pp. 538–543, 2022.
- 1795 [24] A. Karle, "Icecube," arXiv:1003.5715, 2010.

- [25] M. Ackermann, M. Ajello, A. Allafort, L. Baldini, J. Ballet, G. Barbiellini, M. Baring,
   D. Bastieri, K. Bechtol, R. Bellazzini, et al., "Detection of the characteristic pion-decay
   signature in supernova remnants," Science, vol. 339, no. 6121, pp. 807–811, 2013.
- [26] M. Spurio et al., Particles and astrophysics. Springer, 2014.
- [27] P. D. Group, P. Zyla, R. Barnett, J. Beringer, O. Dahl, D. Dwyer, D. Groom, C.-J. Lin,
   K. Lugovsky, E. Pianori, et al., "Review of particle physics," Progress of Theoretical
   and Experimental Physics, vol. 2020, no. 8, p. 083C01, 2020.
- [28] W. Apel, J. Arteaga-Velázquez, K. Bekk, M. Bertaina, J. Blümer, H. Bozdog, I. Brancus, P. Buchholz, E. Cantoni, A. Chiavassa, et al., "Kneelike structure in the spectrum of the heavy component<? format?> of cosmic rays observed with kascade-grande,"

  Physical Review Letters, vol. 107, no. 17, p. 171104, 2011.
- [29] K. Kampert and P. Tinyakov, "Cosmic rays from the knee to the cutoff," *Comptes Rendus. Physique*, 2014.
- [30] I. Collaboration, M. Aartsen, M. Ackermann, J. Adams, J. A. Aguilar, M. Ahlers, M. Ahrens, I. Al Samarai, D. Altmann, K. Andeen, et al., "Neutrino emission from the direction of the blazar txs 0506+ 056 prior to the icecube-170922a alert," Science, vol. 361, no. 6398, pp. 147–151, 2018.
- [31] I. Collaboration, MAGIC, AGILE, ASAS-SN, HAWC, HESS, INTEGRAL, Kanata, Kiso, Kapteyn, et al., "Multimessenger observations of a flaring blazar coincident with high-energy neutrino icecube-170922a," Science, vol. 361, no. 6398, p. eaat1378, 2018.
- [32] J. M. Conrad, M. H. Shaevitz, and T. Bolton, "Precision measurements with highenergy neutrino beams," *Reviews of Modern Physics*, vol. 70, no. 4, p. 1341, 1998.
- [33] J. A. Formaggio and G. P. Zeller, "From ev to eev: Neutrino cross sections across energy scales," *Reviews of Modern Physics*, vol. 84, no. 3, pp. 1307–1341, 2012.
- [34] G. Binder, Measurements of the flavor composition and inelasticity distribution of highenergy neutrino interactions in IceCube. University of California, Berkeley, 2017.
- [35] K. Xie, J. Gao, T. Hobbs, D. R. Stump, C.-P. Yuan, and C.-T. Collaboration), "Highenergy neutrino deep inelastic scattering cross sections," *Physical Review D*, vol. 109, no. 11, p. 113001, 2024.
- [36] T. I. Collaboration, "Measurement of the multi-tev neutrino interaction cross-section with icecube using earth absorption," *Nature*, vol. 551, no. 7682, pp. 596–600, 2017.
- [37] F. Halzen and J. G. Learned, "High energy neutrino detection in deep polar ice," tech. rep., Wisconsin Univ. Dept. Phys., Madison, WI, 1988.

- [38] F. Halzen and J. Learned, "High energy neutrino astronomy: towards a  $1 \ km^3$  detector," tech. rep., P00014297, 1993.
- [39] P. A. Čerenkov, "Visible radiation produced by electrons moving in a medium with velocities exceeding that of light," *Physical Review*, vol. 52, no. 4, p. 378, 1937.
- [40] I. Frank and I. Tamm, "Coherent visible radiation of fast electrons passing through matter," in *Selected Papers*, pp. 29–35, Springer, 1991.
- 1835 [41] D. Chirkin and W. Rhode, "Propagating leptons through matter with muon monte carlo (mmc)," arXiv preprint hep-ph/0407075, 2004.
- [42] T. DeYoung, S. Razzaque, and D. Cowen, "Astrophysical tau neutrino detection in kilometer-scale cherenkov detectors via muonic tau decay," *Astroparticle Physics*, vol. 27, no. 4, pp. 238–243, 2007.
- <sup>1840</sup> [43] D. Cowen, for the IceCube Collaboration, et al., "Tau neutrinos in icecube," in *Journal* of *Physics: Conference Series*, vol. 60, p. 227, IOP Publishing, 2007.
- [44] A. Gaertner, The Pacific Ocean Neutrino Experiment: Site characterization, background studies and tau neutrino sensitivity. PhD thesis, University of Alberta, 2024.
- [45] C. Spiering, "Towards high-energy neutrino astronomy: a historical review," *The Eu-*1845 ropean Physical Journal H, vol. 37, no. 3, pp. 515–565, 2012.
- [46] H. Hanada, T. Hayashino, M. Ito, A. Iwasaki, K. Kawamorita, H. Kawamoto, T. Matsumoto, S. Narita, T. Takayama, S. Tanaka, et al., "A highly sensitive optical detector for use in deep underwater," Nuclear Instruments and Methods in Physics Research Section A: Accelerators, Spectrometers, Detectors and Associated Equipment, vol. 408, no. 2-3, pp. 425–437, 1998.
- [47] G. Safronov, "Baikal-gvd: status and first results," arXiv preprint arXiv:2012.03373, 2020.
- [48] E. Andres, P. Askebjer, S. Barwick, R. Bay, L. Bergström, A. Biron, J. Booth, A. Bouchta, S. Carius, M. Carlson, et al., "The amanda neutrino telescope: principle of operation and first results," Astroparticle Physics, vol. 13, no. 1, pp. 1–20, 2000.
- [49] M. Ageron, J. Aguilar, I. Al Samarai, A. Albert, F. Ameli, M. André, M. Anghinolfi,
   G. Anton, S. Anvar, M. Ardid, et al., "Antares: the first undersea neutrino telescope,"
   Nuclear Instruments and Methods in Physics Research Section A: Accelerators, Spectrometers, Detectors and Associated Equipment, vol. 656, no. 1, pp. 11–38, 2011.

- [50] S. Aiello, A. Albert, M. Alshamsi, S. A. Garre, Z. Aly, A. Ambrosone, F. Ameli, M. Andre, G. Androulakis, M. Anghinolfi, et al., "The km3net multi-pmt optical module,"
   Journal of Instrumentation, vol. 17, no. 07, p. P07038, 2022.
- [51] S. Adrian-Martinez, M. Ageron, F. Aharonian, S. Aiello, A. Albert, F. Ameli, E. Anassontzis, M. Andre, G. Androulakis, M. Anghinolfi, et al., "Letter of intent for km3net 2.0," Journal of Physics G: Nuclear and Particle Physics, vol. 43, no. 8, p. 084001, 2016.
- 1867 [52] R. Bruijn and D. van Eijk, "The km3net multi-pmt digital optical module," *PoS* (*ICRC2015*), vol. 1157, 2015.
- [53] J. G. Learned, "Future of high-energy neutrino astronomy," in *Proc. Venice Workshop on Neutrino telescopes*, 1990.
- [54] P. Askebjer, S. Barwick, L. Bergström, A. Bouchta, S. Carius, A. Coulthard, K. Engel,
   B. Erlandsson, A. Goobar, L. Gray, et al., "Optical properties of the south pole ice at depths between 0.8 and 1 kilometer," Science, vol. 267, no. 5201, pp. 1147–1150, 1995.
- [55] A. collaboration *et al.*, "Amanda: status, results and future," *Arxiv preprint astro-*ph/9906205, 1999.
- [56] A. Achterberg, M. Ackermann, J. Adams, J. Ahrens, K. Andeen, D. Atlee, J. Bahcall, X. Bai, B. Baret, M. Bartelt, et al., "Limits on the high-energy gamma and neutrino fluxes from the sgr 1806-20 giant flare<? format?> of 27 december 2004 with the amanda-ii detector," Physical review letters, vol. 97, no. 22, p. 221101, 2006.
- [57] A. Achterberg, M. Ackermann, J. Adams, J. Ahrens, K. Andeen, J. Auffenberg, X. Bai,
   B. Baret, S. Barwick, R. Bay, et al., "Multiyear search for a diffuse flux of muon
   neutrinos with amanda-ii," Physical Review D—Particles, Fields, Gravitation, and
   Cosmology, vol. 76, no. 4, p. 042008, 2007.
- [58] A. Achterberg, M. Ackermann, J. Adams, J. Ahrens, K. Andeen, J. Auffenberg, J. Bahcall, X. Bai, B. Baret, S. Barwick, *et al.*, "The search for muon neutrinos from northern hemisphere gamma-ray bursts with amanda," *The Astrophysical Journal*, vol. 674, no. 1, p. 357, 2008.
- [59] R. Abbasi, M. Ackermann, J. Adams, M. Ahlers, J. Ahrens, K. Andeen, J. Auffenberg,
   X. Bai, M. Baker, B. Baret, et al., "Search for point sources of high energy neutrinos
   with final data from amanda-ii," Physical Review D—Particles, Fields, Gravitation,
   and Cosmology, vol. 79, no. 6, p. 062001, 2009.
- [60] I. Collaboration\*, "Evidence for high-energy extraterrestrial neutrinos at the icecube detector," *Science*, vol. 342, no. 6161, p. 1242856, 2013.

- [61] I. Collaboration\*†, R. Abbasi, M. Ackermann, J. Adams, J. Aguilar, M. Ahlers, M. Ahrens, J. Alameddine, A. Alves Jr, N. Amin, et al., "Observation of high-energy neutrinos from the galactic plane," Science, vol. 380, no. 6652, pp. 1338–1343, 2023.
- [62] M. Bohmer, R. Gernhäuser, L. Ginzkey, R. Halliday, C. Spannfellner, N. Whitehorn,
   P.-O. Collaboration, et al., "Sub-ns timing for the pacific ocean neutrino experiment
   by optical fiber using gigabit ethernet," in 38th International Cosmic Ray Conference,
   p. 1216, 2024.
- [63] C. R. Barnes, M. M. Best, and A. Zielinski, "The neptune canada regional cabled ocean observatory," *Technology (Crayford, England)*, vol. 50, no. 3, 2008.
- [64] F. Henningsen, "Optical characterization of the deep pacific ocean: Development of an optical sensor array for a future neutrino telescope," Technical University of Munich, July 2018, Master Thesis, 2018.
- [65] A. Gärtner, "Development of an optical sensor system for the characterization of cascadia basin, canada," *Technical University of Munich, 2018, Master Thesis*, 2018.
- [66] M. Boehmer, J. Bosma, D. Brussow, L. Farmer, C. Fruck, R. Gernhäuser, A. Gärtner, D. Grant, F. Henningsen, S. Hiller, et al., "Straw (strings for absorption length in water): pathfinder for a neutrino telescope in the deep pacific ocean," Journal of Instrumentation, vol. 14, no. 02, p. P02013, 2019.
- 1912 [67] I. C. Rea, The Pacific ocean neutrino experiment: feasibility study for a new neutrino telescope at Cascadia basin, NE Pacific ocean. PhD thesis, Technische Universität München, 2021.
- [68] K. Holzapfel, C. Spannfellner, O. Aghaei, A. Baron, J. Bedard, M. Böhmer, J. Bosma,
   N. Deis, C. Fink, C. Fruck, et al., "Straw-b (strings for absorption length in water-b):
   the second pathfinder mission for the pacific ocean neutrino experiment," Journal of
   Instrumentation, vol. 19, no. 05, p. P05072, 2024.
- [69] A. Capone, T. Digaetano, A. Grimaldi, R. Habel, D. L. Presti, E. Migneco, R. Masullo, F. Moro, M. Petruccetti, C. Petta, et al., "Measurements of light transmission in deep sea with the ac9 trasmissometer," Nuclear Instruments and Methods in Physics Research Section A: Accelerators, Spectrometers, Detectors and Associated Equipment, vol. 487, no. 3, pp. 423–434, 2002.
- 1924 [70] V. Balkanov, I. Belolaptikov, L. Bezrukov, A. Chensky, N. Budnev, I. Danilchenko, Z.-A. Dzhilkibaev, G. Domogatsky, A. Doroshenko, S. Fialkovsky, et al., "In situ measurements of optical parameters in lake baikal with the help of a neutrino telescope,"

  1927 Applied Optics, vol. 38, no. 33, pp. 6818–6825, 1999.

- [71] G. Riccobene, A. Capone, S. Aiello, M. Ambriola, F. Ameli, I. Amore, M. Anghinolfi, A. Anzalone, C. Avanzini, G. Barbarino, et al., "Deep seawater inherent optical properties in the southern ionian sea," Astroparticle Physics, vol. 27, no. 1, pp. 1–9, 2007.
- [72] E. Anassontzis, A. Ball, A. Belias, A. Fotiou, G. Grammatikakis, H. Kontogiannis, P. Koske, S. Koutsoukos, V. Lykoussis, E. Markopoulos, et al., "Water transparency measurements in the deep ionian sea," Astroparticle Physics, vol. 34, no. 4, pp. 187–197, 2010.
- 1936 [73] I. C. Rea, K. Holzapfel, A. Baron, N. Bailly, J. Bedard, M. Bohmer, J. Bosma, D. Brussow, J. Cheng, K. Clark, et al., "P-one second pathfinder mission: Straw-b," in 37th International Cosmic Ray Conference, p. 1092, 2022.
- [74] P-ONE Collaboration, "Pathfinder-2." https://www.pacific-neutrino.org/pathfinder-2. Accessed: 2025-08-15.
- [75] J. Stacho, F. Henningsen, K. Nell, et al., "Development of calibration light sources for the pacific ocean neutrino experiment," in *Proceedings of 38th International Cosmic Ray Conference—PoS (ICRC2023)*, p. 49, 2023.
- [76] D. Ghuman, F. Henningsen, M. Danninger, P.-O. Collaboration, et al., "The acoustic calibration system for the pacific ocean neutrino experiment," in 38th International Cosmic Ray Conference, p. 1112, 2024.
- [77] M. Aartsen, K. Abraham, M. Ackermann, J. Adams, J. Aguilar, M. Ahlers, M. Ahrens,
   D. Altmann, T. Anderson, M. Archinger, et al., "Characterization of the atmospheric
   muon flux in icecube," Astroparticle physics, vol. 78, pp. 1–27, 2016.
- <sup>1950</sup> [78] D. Soldin, "Atmospheric muons measured with icecube," in *EPJ Web of Conferences*, vol. 208, p. 08007, EDP Sciences, 2019.
- [79] R. Abbasi, M. Ackermann, J. Adams, J. Aguilar, M. Ahlers, M. Ahrens, C. Alispach,
  A. Alves Jr, N. Amin, R. An, et al., "Leptoninjector and leptonweighter: A neutrino
  event generator and weighter for neutrino observatories," Computer physics communications, vol. 266, p. 108018, 2021.
- [80] A. Gazizov and M. Kowalski, "Anis: High energy neutrino generator for neutrino telescopes," *Computer Physics Communications*, vol. 172, no. 3, pp. 203–213, 2005.
- 1958 [81] IceCube Neutrino Observatory, "Icetray Documentation."
- [82] C. A. Argüelles, J. Salvado, and C. N. Weaver, "nusquids: A toolbox for neutrino propagation," *Computer Physics Communications*, vol. 277, p. 108346, 2022.

- 1961 [83] A. M. Dziewonski and D. L. Anderson, "Preliminary reference earth model," *Physics*1962 of the earth and planetary interiors, vol. 25, no. 4, pp. 297–356, 1981.
- 1963 [84] D. Heck, J. Knapp, J. Capdevielle, G. Schatz, T. Thouw, et al., "Corsika: A monte carlo code to simulate extensive air showers," Report fzka, vol. 6019, no. 11, 1998.
- 1965 [85] I. collaboration, "Muongun."
- 1966 [86] G. Carminati, M. Bazzotti, S. Biagi, S. Cecchini, T. Chiarusi, A. Margiotta, M. Sioli, and M. Spurio, "Mupage: a fast atmospheric muon generator for neutrino telescopes based on parametric formulas," arXiv preprint arXiv:0907.5563, 2009.
- [87] J.-H. Koehne, K. Frantzen, M. Schmitz, T. Fuchs, W. Rhode, D. Chirkin, and J. B.
   Tjus, "Proposal: A tool for propagation of charged leptons," Computer Physics Communications, vol. 184, no. 9, pp. 2070–2090, 2013.
- [88] M. Dunsch, J. Soedingrekso, A. Sandrock, M. Meier, T. Menne, and W. Rhode, "Recent improvements for the lepton propagator proposal," *Computer Physics Communications*, vol. 242, pp. 132–144, 2019.
- [89] J. Lundberg, P. Miočinović, K. Woschnagg, T. Burgess, J. Adams, S. Hundertmark,
   P. Desiati, and P. Niessen, "Light tracking through ice and water—scattering and
   absorption in heterogeneous media with photonics," Nuclear Instruments and Methods
   in Physics Research Section A: Accelerators, Spectrometers, Detectors and Associated
   Equipment, vol. 581, no. 3, pp. 619–631, 2007.
- [90] M. Ackermann, J. Ahrens, X. Bai, M. Bartelt, S. Barwick, R. Bay, T. Becka, J. Becker,
   K.-H. Becker, P. Berghaus, et al., "Optical properties of deep glacial ice at the south
   pole," Journal of Geophysical Research: Atmospheres, vol. 111, no. D13, 2006.
- [91] D. Chirkin, I. Collaboration, et al., "Photon tracking with gpus in icecube," Nuclear
   Instruments and Methods in Physics Research Section A: Accelerators, Spectrometers,
   Detectors and Associated Equipment, vol. 725, pp. 141–143, 2013.
- [92] D. Chirkin, J. C. Díaz-Vélez, C. Kopper, A. Olivas, B. Riedel, M. Rongen, D. Schultz,
   and J. van Santen, "Photon propagation using gpus by the icecube neutrino observatory," in 2019 15th International Conference on eScience (eScience), pp. 388–393,
   IEEE, 2019.
- [93] H. Schwanekamp, R. Hohl, D. Chirkin, T. Gibbs, A. Harnisch, C. Kopper, P. Messmer,
   V. Mehta, A. Olivas, B. Riedel, et al., "Accelerating icecube's photon propagation code
   with cuda," Computing and Software for Big Science, vol. 6, no. 1, p. 4, 2022.
- 1993 [94] R. Abbasi, Y. Abdou, T. Abu-Zayyad, J. Adams, J. Aguilar, M. Ahlers, K. Andeen, J. Auffenberg, X. Bai, M. Baker, et al., "Calibration and characterization of the icecube

- photomultiplier tube," Nuclear Instruments and Methods in Physics Research Section
  A: Accelerators, Spectrometers, Detectors and Associated Equipment, vol. 618, no. 1-3,
  pp. 139–152, 2010.
- [95] S. Adrián-Martínez, S. Aiello, F. Ameli, M. Anghinolfi, M. Ardid, G. Barbarino, E. Barbarito, F. C. T. Barbato, N. Beverini, S. Biagi, et al., "Long term monitoring of the optical background in the capo passero deep-sea site with the nemo tower prototype,"

  The European Physical Journal C, vol. 76, no. 2, p. 68, 2016.
- [96] R. Abbasi *et al.*, "A muon-track reconstruction exploiting stochastic losses for large-scale cherenkov detectors," *Journal of Instrumentation*, vol. 16, no. 08, p. P08034, 2021.
- <sup>2005</sup> [97] A. Wallace, "Direction reconstruction of icecube neutrino events with millipede," Master's thesis, The University of Adelaide, 2016.
- <sup>2007</sup> [98] T. De Young, "Icetray: A software framework for icecube," CERN, 2005.
- 2008 [99] D. Ghuman, "Muon track reconstruction for the pacific ocean neutrino explorer," Mas-2009 ter's thesis, Queen's University (Canada), 2021.
- [100] M. Hünnefeld, "Combining maximum-likelihood with deep learning for event reconstruction in icecube," arXiv preprint arXiv:2107.12110, 2021.
- [101] N. Whitehorn, J. van Santen, and S. Lafebre, "Penalized splines for smooth representation of high-dimensional monte carlo datasets," *Computer Physics Communications*, vol. 184, no. 9, pp. 2214–2220, 2013.
- [102] M. Aartsen, R. Abbasi, Y. Abdou, M. Ackermann, J. Adams, J. Aguilar, M. Ahlers,
   D. Altmann, J. Auffenberg, X. Bai, et al., "Improvement in fast particle track reconstruction with robust statistics," Nuclear Instruments and Methods in Physics Research
   Section A: Accelerators, Spectrometers, Detectors and Associated Equipment, vol. 736,
   pp. 143–149, 2014.
- 2020 [103] IceCube Neutrino Observatory, "Icetray Documentation."
- [104] G. B. Dantzig, Origins of the Simplex Method, p. 141–151. New York, NY, USA:
  Association for Computing Machinery, 1990.
- [105] D. Alexandreas, D. Berley, S. Biller, G. Dion, J. Goodman, T. Haines, C. Hoffman, E. Horch, X.-Q. Lu, C. Sinnis, et al., "Point source search techniques in ultra high energy gamma ray astronomy," Nuclear Instruments and Methods in Physics Research Section A: Accelerators, Spectrometers, Detectors and Associated Equipment, vol. 328, no. 3, pp. 570–577, 1993.

- [106] A. Abeysekara, R. Alfaro, C. Alvarez, J. Álvarez, R. Arceo, J. Arteaga-Velázquez, H. A. Solares, A. Barber, B. Baughman, N. Bautista-Elivar, et al., "Sensitivity of the high altitude water cherenkov detector to sources of multi-tev gamma rays," Astroparticle Physics, vol. 50, pp. 26–32, 2013.
- [107] J. Ahrens, J. N. Bahcall, X. Bai, R. Bay, T. Becka, K.-H. Becker, D. Berley, E. Bernardini, D. Bertrand, D. Besson, et al., "Sensitivity of the icecube detector to astrophysical sources of high energy muon neutrinos," Astroparticle physics, vol. 20, no. 5, pp. 507–532, 2004.
- <sup>2036</sup> [108] J. Stettner, "Measurement of the diffuse astrophysical muon-neutrino spectrum with ten years of icecube data," arXiv preprint arXiv:1908.09551, 2019.
- [109] IceCube Collaboration, "nuflux: a library for calculating atmospheric neutrino fluxes." IceCube/nuflux.
- <sup>2040</sup> [110] D. Caprioli, "Particle acceleration at shocks: An introduction," in Foundations of Cos-<sup>2041</sup> mic Ray Astrophysics, pp. 143–181, IOS Press, 2024.
- <sup>2042</sup> [111] M. G. Baring, "Diffusive shock acceleration: The fermi mechanism," arXiv preprint astro-ph/9711177, 1997.
- [112] G. Cowan, "Discovery sensitivity for a counting experiment with background uncertainty," en. In, vol. 8, 2012.
- <sup>2046</sup> [113] G. Cowan, K. Cranmer, E. Gross, and O. Vitells, "Asymptotic formulae for likelihood-based tests of new physics," *The European Physical Journal C*, vol. 71, pp. 1–19, 2011.
- <sup>2048</sup> [114] L. Lista, Statistical Methods for Data Analysis: With Applications in Particle Physics, vol. 1010. Springer Nature, 2023.
- <sup>2050</sup> [115] O. Behnke, K. Kröninger, G. Schott, and T. Schörner-Sadenius, *Data analysis in high* <sup>2051</sup> energy physics: a practical guide to statistical methods. John Wiley & Sons, 2013.